A MOTION OF FREELY OSCILLATING DROPLET OF A YIELD STRESS FLUID: ANALYSIS AND NUMERICAL STUDIES

A Dissertation Presented to

the Faculty of the Department of Mathematics

University of Houston

In Partial Fulfillment

of the Requirements for the Degree

Doctor of Philosophy

By

Wanli Cheng

September 2017

A MOTION OF FREELY OSCILLATING DROPLET OF A YIELD STRESS FLUID: ANALYSIS AND NUMERICAL STUDIES

Wanli Cheng

APPROVED:

Dr. Maxim Olshanskii, (Committee Chair)
Department of Mathematics, University of Houston

Dr. Tsorng-whay Pan,
Department of Mathematics, University of Houston

Dr. Annalisa Quaini,
Department of Mathematics, University of Houston

Dr. Jesse Chan,
Dept of Computational and Applied Mathematics,
Rice University

Dean, College of Natural Sciences and Mathematics

Acknowledgements

Firstly, I would like to express my deepest gratitude to my doctoral advisor Dr. Maxim Olshanskii. He is always nice and patient. He taught me how to solve problems: he always could break one hard topics into several easy ones which I could handle. He is also a patient and kindness person: he always reply me as fast as he could no matter how later it is. This four years, I really learnt a lot, not only the ability to complete doctoral program and the ability to solve problems but also how to be a good man– a man who is kind, patient and professional.

Dr Shanyu Ji is also an important professor in my life. He give me the second chance to study Mathematics again. He is such a good person that not only help me in my academic career but also give me a lot of care to my life.

Thank you for Dr Kirill Terekhov, he is very kind person who always be patient and give me a lot of solid suggestions about set up numerical experiments in my thesis.

The last but not the least I want to say thank you to my wife Kuikui Gao. We met each other at the beginning of our graduate student career, we share the same enthusiasm to maths, and we hold hand together to face everything before and now. She made my graduate student career colorful and full of happiness.

A MOTION OF FREELY OSCILLATING DROPLET OF A YIELD STRESS FLUID: ANALYSIS AND NUMERICAL STUDIES

An Abstract of a Dissertation

Presented to

the Faculty of the Department of Mathematics

University of Houston

In Partial Fulfillment

of the Requirements for the Degree

Doctor of Philosophy

By

Wanli Cheng

September 2017

Abstract

This dissertation studies the problem of free small-amplitude oscillations of a droplet of a yield stress fluid under the action of surface tension forces. The problem is treated both analytically and numerically. In particular, we address the question if there exists a finite stopping time for an unforced motion of a yield stress fluid with free surface.

In this thesis, a variational inequality formulation is deduced for the problem of yield stress fluid dynamics with a free surface. The free surface is assumed to evolve with a normal velocity of the flow. We also consider capillary forces acting along the free surface. Based on the variational inequality formulation an energy equality is obtained, where kinetic and free energy rate of change is in balance with the internal energy viscoplastic dissipation and the work of external forces. Further, we consider free small-amplitude oscillations of a droplet of Herschel-Bulkley fluid under the action of surface tension forces. Under certain assumptions it is shown that the finite stopping time T_f of oscillations exists once the yield stress parameter is positive and the flow index α satisfies $\alpha \geq 1$. Results of several numerical experiments illustrate the analysis, reveal the dependence of T_f on problem parameters and suggest an instantaneous transition of the whole drop from yielding state to the rigid one.

In charpter 1, we review the Navier-Stokes equations for motion of incompressible viscous fluid and consider different boundary conditions. We also discuss several approaches to recover the evolution of free interface.

In charpter 2, we derive a variational inequality formulation for the problem of yield stress fluid dynamics with a free surface. An energy balance follows from

the variational inequality. In this chapter, we also describe a numerical method to simulate a non-Newtonian fluid flow with free surface.

In charpter 3, we apply the method of viscous velocity potentials to study the problem of small-amplitude oscillations of a fluid droplet driven by surface tension forces. First the Newtonian fluid is treated and some well-known results are derived. Numerical experiments are provided to illustrate our results.

In charpter 4, we apply the method of visco-plastic velocity potentials to study the problem of small-amplitude oscillations of a non-Newtonian droplet driven by free surface tension forces. For a yield stress fluid we prove that oscillations have a finite stopping time. We describe the motion of a single harmonic ($2nd$ order harmonic) of oscillating droplet by an ODE. Numerical experiments illustrated our results.

In charper 5, we give the conclusion and outlook.

The main results of the thesis are published in Cheng W., Olshanskii M.A., Finite stopping times for freely oscillating drop of a yield stress fluid, Journal of Non-Newtonian Fluid Mechanics; 239 (2017) 7384.

Contents

CHAPTER 1

Introduction

1.1 Basic equations of fluid dynamics

1.1.1 Governing equations for one phase flow

We review the derivation of the Navier-Stokes equations for a laminar flow of incompressible fluid. We assume the fluid to be incompressible and pure (i.e., no mixture of different components). Moreover, we assume isothermal conditions and therefore neglect variations of density and viscosity of fluid due to temperature changes. Hence, the dynamic viscosity coefficient is constant and positive. Due to incompressibility

the density is also constant and positive.

One can distinct two general approaches to the description of fluid motion. In the Eulerian approach one measures a given property by either carrying out the measurement at a fixed point in space as particles of the fluid pass by, or by following a parcel of fluid along material lines. The derivative of a field with respect to a fixed position in space is called the Eulerian derivative, while the derivative following a moving parcel is called the advective or material ("Lagrangian" [40]) derivative. We always assume that the fluid occupies a bounded time dependent domain $\Omega(t) \in \mathbb{R}^3$ for $t \in [0, \infty)$. The Eulerian coordinates of a point in Ω are denoted by $\mathbf{x} = (x_1, x_2, x_3)$. We take a fixed $t_0 \in (0, T)$ and consider a time interval $(t_0 - \delta, t_0 + \delta)$, with $\delta > 0$ sufficiently small such that for $t \in (t_0 - \delta, t_0 + \delta)$. Let X denote a particle (also called material point) in Ω at $t = t_0$, with Eulerian coordinates $\xi \in \mathbb{R}^3$. Let$X_{\xi(t)}$ denote the Eulerian coordinates of the particle X at time t. The mapping

$$t \to X_\xi(t),\ t \in (t_0 - \delta, t_0 + \delta)$$

describes the trajectory of the particle X. The particles are transported by the fluid velocity field, which is denoted by $\mathbf{u} = \mathbf{u}(\mathbf{x}, t) = (u_1(\mathbf{x}, t), u_2(\mathbf{x}, t), u_3(\mathbf{x}, t)) \in \mathbb{R}^3$. Hence

$$\frac{d}{dt} X_\xi(t) = \mathbf{u}(X_\xi(t), t). \tag{1.1}$$

For the given X, the solution of the system of ordinary differential equations

$$\frac{d}{dt} X_\xi(t) = \mathbf{u}(X_\xi(t), t),\ t \in (t_0 - \delta, t_0 + \delta),\ X_\xi(t_0) = \xi$$

yields the trajectory of the particle ξ.

Physical processes can be modeled in different coordinate systems. For flow problems, the two most important ones are $(\mathbf{x}, t)$ (Eulerian) and (ξ, t) (Lagrangian):

- Euler coordinates $(\mathbf{x}, t)$: one takes an arbitrary fixed point $\mathbf{x}$ in space and considers the velocity $\mathbf{u}(\mathbf{x}, t)$ at $\mathbf{x}$. If time evolves different particles pass through $\mathbf{x}$.

- Lagrange (or material) coordinates (ξ, t): one takes an arbitrary fixed particle (material point) and considers its motion. If time evolves one thus follows the trajectory of a fixed particle

Related to the Lagrangian coordinates, we define the so-called material derivative of a (sufficiently smooth) function $f(\mathbf{x}, t)$ on the trajectory of X:

$$\dot{f}(X_\xi(t), t) := \frac{d}{dt} f(X_\xi(t), t)$$

The material derivative [24] describes the time rate of change of some physical quantity (like momentum) for a material element subjected to a space-and-time-dependent macroscopic velocity field. The material derivative can serve as a link between Eulerian and Lagrangian descriptions of continuum deformation

If f is defined in a neighborhood of the trajectory, we obtain from the chain rule and (1.1)

$$\dot{f} := \frac{\partial f}{\partial t} + \mathbf{u} \cdot \nabla f$$

We further need the **Reynolds' transport theorem:** for a scalar sufficiently smooth function $f = f(\mathbf{x}, t)$ it holds

$$\frac{d}{dt} \int_{\Omega(t)} f(\mathbf{x}, t) d\mathbf{x} = \int_{\Omega(t)} \left(\dot{f}(\mathbf{x}, t) + f \, \mathbf{div}\, \mathbf{u}(\mathbf{x}, t) \right) d\mathbf{x} = \int_{\Omega(t)} \left(\frac{\partial f}{\partial t}(\mathbf{x}, t) + \mathbf{div}(f\mathbf{u})(\mathbf{x}, t) \right) d\mathbf{x} \tag{1.2}$$

with $\dot{f} := \frac{\partial f}{\partial t} + \mathbf{u} \cdot \nabla f$ the material derivative.

First we consider the conservation of mass principle. Then the variation of mass is

$$\frac{d}{dt} \int_{\Omega(t)} \rho d\mathbf{x} = \int_{\Omega(t)} \left(\frac{\partial \rho}{\partial t} + \mathbf{div}(\rho \mathbf{u}) \right) d\mathbf{x} = 0 \quad for \quad t \in (0, T)$$

which holds in particular for $t = t_0$ and for an arbitrary material volume $\Omega(t_0) = \Omega_0$. Since also $t_0 \in (0, \infty)$ is arbitrary, we obtain the partial differential equation

$$\frac{\partial \rho}{\partial t} + \mathbf{div}(\rho \mathbf{u}) = 0 \quad in \quad \Omega \times (0, T)$$

Due to the assumption $\rho = const$ this simplifies to

$$\mathbf{div}\, \mathbf{u} = 0 \quad in \quad \Omega \times (0, T) \tag{1.3}$$

which is often called mass conservation equation or continuity equation.

We now consider conservation of momentum. The momentum of mass contained

in $\Omega(t)$ is given by

$$M(t) = \int_{\Omega(t)} \rho \mathbf{u} d\mathbf{x}.$$

Due to Newton's law the change of momentum $M(t)$ is equal to the force $F(t)$ acting on $\Omega(t)$. This force is decomposed in a volume force $F_1(t)$ and a boundary force $F_2(t)$,

$$F_1(t) = \int_{\Omega(t)} \mathbf{f} d\mathbf{x}.$$

The boundary force $F_2(t)$ is used to describe internal forces, i.e., forces that a fluid exerts on itself. These include pressure and the viscous drag that a fluid element $\Omega(t)$ gets from the adjacent fluid. These internal forces are contact forces: they act on the boundary $\partial\Omega(t)$ of the fluid element $\Omega(t)$. Let $\mathbf{t}$ denote this internal force vector, also called traction vector. Then we have

$$F_2(t) = \int_{\partial\Omega(t)} \mathbf{t} d\mathbf{x}.$$

Cauchy derived fundamental principles of continuum mechanics and in particular he derived the following law (often called Cauchys theorem): $\mathbf{t}$ is a linear function of $\mathbf{n}$, where $\mathbf{n} = \mathbf{n}(x,t) \in \mathbb{R}^3$ is the outer unit normal on $\partial\Omega(t)$.

Thus it follows that there is a matrix $\boldsymbol{\sigma} = \boldsymbol{\sigma}(\mathbf{x},t) \in \mathbb{R}^{3\times 3}$, called the stress tensor,

such that the boundary force can be represented as

$$F_2(t) = \int_{\partial\Omega(t)} \boldsymbol{\sigma}\mathbf{n}d\mathbf{x}.$$

Using these force representation in Newton's law and applying Stokes's theorem for $F_2(t)$ we get

$$\frac{d}{dt}M(t) = F_1(t) + F_2(t) = \int_{\Omega(t)} (\mathbf{f} + \mathbf{div}\,\boldsymbol{\sigma})\, d\mathbf{x}. \tag{1.4}$$

Using Reynold's transport theorem in the left-hand side of (1.4) with $f = \rho u_i$, $i = 1, 2, 3$, we obtain

$$\int_{\Omega(t)} \frac{\partial \rho u_i}{\partial t} + div(\rho u_i \mathbf{u})d\mathbf{x} = \int_{\Omega(t)} (f_i + \nabla \cdot \boldsymbol{\sigma}_i)\, d\mathbf{x}, \quad i = 1, 2, 3, \tag{1.5}$$

with $\boldsymbol{\sigma}_i$ the i-th row of tensor $\boldsymbol{\sigma}$ and f_i the i-th component of vector $\mathbf{f}$. Note that

$$div(u_i\mathbf{u}) = u_i div(\mathbf{u}) + \mathbf{u} \cdot \nabla u_i$$

and due to the continuity equation (1.3), since $t_0 \in (0, T)$ is arbitrary,

$$\frac{\partial \rho u_i}{\partial t} + \rho\mathbf{u} \cdot \nabla u_i = f_i + \nabla \cdot \boldsymbol{\sigma}_i, \tag{1.6}$$

In vector notation, we get the so-called Cauchy momentum equation,

$$\frac{\partial \rho\mathbf{u}}{\partial t} + \rho(\mathbf{u} \cdot \nabla)\mathbf{u} = \mathbf{f} + \mathbf{div}\,\boldsymbol{\sigma}, \tag{1.7}$$

Equation (1.3) and (1.7) are known as the Navier-Stokes equations for incompressible flow:

$$\begin{cases} \rho(\dfrac{\partial \mathbf{u}}{\partial t} + (\mathbf{u} \cdot \nabla \mathbf{u})) - \mathbf{div}\, \boldsymbol{\sigma} = \mathbf{f} \\ \nabla \cdot \mathbf{u} = 0 \end{cases} \quad \text{in } \ \Omega(t), \tag{1.8}$$

1.1.2 Constitutive law between stress tensor and the rate of deformation tensor

The Cauchy momentum equation (1.7) describes the non-relativistic momentum conservation of any continuum that conserves mass. $\boldsymbol{\sigma}$ is a symmetric tensor given by its covariant components. In orthogonal coordinates in three dimensions it is represented as a 3×3 matrix:

$$\left[\sigma_{ij}\right] = \begin{bmatrix} \sigma_{xx} & \tau_{xy} & \tau_{xy} \\ \tau_{yx} & \sigma_{yy} & \tau_{yz} \\ \tau_{zx} & \tau_{zy} & \sigma_{zz} \end{bmatrix}$$

where σ_{ij} are normal stresses and τ are shear stresses.

The constitutive law between stress tensor and the rate of deformation tensor defines the behavior of fluid flows, where $\mathbf{Du} := \frac{1}{2}(\nabla \mathbf{u} + \nabla \mathbf{u}^T)$ is the rate of deformation tensor.

For viscous Newtonian fluids one assumes that the stress tensor $\boldsymbol{\sigma}$ is of the form

$$\boldsymbol{\sigma} = -p\mathbf{I} + L(\mathbf{Du}),$$

where p is the pressure, $\nabla \mathbf{u} := (\nabla u_1, \quad \nabla u_2, \quad \nabla u_3)^T$ and L is assumed to be a linear mapping. Based on this structural model for the stress tensor and using the additional assumptions that the medium is isotropic (i.e. its properties are the same in all spatial directions) and the action of the stress tensor is independent of the specific frame of reference, it can be shown [26] that the stress tensor of the Newtonian fluid takes the form

$$\boldsymbol{\sigma} = -p\mathbf{I} + \lambda(\nabla \cdot \mathbf{u})\mathbf{I} + 2\mu\mathbf{D}(\mathbf{u})$$

Further physical considerations lead to relations for the parameters μ, λ, e.g., $\mu > 0$(for a viscous fluid), $\lambda \geq -\frac{2}{3}\mu$ or even $\lambda = -\frac{2}{3}\mu$. For the case of an incompressible fluid, i.e.,$\mathbf{div}\,\mathbf{u} = 0$, the relation for the stress tensor is simplified to

$$\boldsymbol{\sigma} = -p\mathbf{I} + 2\mu\mathbf{D}(\mathbf{u}) \tag{1.9}$$

with $\mu > 0$ the dynamic viscosity. Using the identity

$$2\,\mathbf{div}(\mathbf{Du}) = \Delta\mathbf{u}$$

we get the fundamental Navier-Stokes equations for the incompressible Newtonian fluid flow:

$$\begin{cases} \rho(\dfrac{\partial \mathbf{u}}{\partial t} + (\mathbf{u} \cdot \nabla \mathbf{u})) - \mu\Delta\mathbf{u} + \nabla p = \mathbf{f} \\ \nabla \cdot \mathbf{u} = 0 \end{cases} \quad \text{in } \ \Omega(t). \tag{1.10}$$

For visco-plastic fluids, one common choice for constitutive law for the stress

tensor is the Herschel-Bulkley constitutive law:

$$\begin{aligned} \boldsymbol{\tau} = (K|\mathbf{Du}|^{\alpha-1} + \tau_s|\mathbf{Du}|^{-1})\mathbf{Du} \quad &\Leftrightarrow \quad |\boldsymbol{\tau}| > \tau_s \\ \mathbf{Du} = 0 \quad &\Leftrightarrow \quad |\boldsymbol{\tau}| \leq \tau_s \end{aligned} \tag{1.11}$$

where $\boldsymbol{\tau}$ is the deviatoric part of the stress tensor, $\boldsymbol{\sigma}_{ij} = \boldsymbol{\tau}_{ij} + p\delta_{ij}$, with pressure p. Further notations introduced above are the following: For a tensor $\mathbf{A}$, $|\mathbf{A}|$ denotes its Frobenius norm

$$|\mathbf{A}| = (\mathbf{A} : \mathbf{A})^{\frac{1}{2}} = (\sum_{1\leq i,j\leq 3} |A_{ij}|^2)^{\frac{1}{2}},$$

Here τ_s is the yield stress parameter, K is the consistency parameter, $\alpha > 0$ is the flow index (for $\alpha < 1$ the fluid exhibits shear-thinning property whereas for $\alpha > 1$ it is shear-thickening; $\alpha = 1$ corresponds to the classic case of the Bingham plastic). The medium behaves like a fluid in the domain where $|\mathbf{Du}| \neq 0$, the so-called flow region, and exhibits the rigid body behavior in the region where the stresses do not exceed the threshold parameter τ_s, the so-called rigid (or plug) region.

1.1.3 Navier-Stokes equations for two phase flow

We now consider two-phase flows, i.e., Ω contains two different immiscible incompressible phases (liquid-liquid or liquid-gas) which may move in time and have different material properties ρ_i and $\mu_i, i = 1, 2$.

For each point in time, $t \in [0, T]$, Ω is partitioned into two open subdomains $\Omega_1(t)$ and $\Omega_2(t)$, $\overline{\Omega(t)} = \overline{\Omega_1(t)} \cup \overline{\Omega_2(t)}$, $\overline{\Omega_1(t)} \cap \overline{\Omega_2(t)} = \emptyset$, each of them containing one of the phases, respectively.

These phases are separated from each other by the interface $\Gamma(t) = \overline{\Omega(t)} \cap \overline{\Omega_2(t)}$. We do not consider reaction, mass transfer or phase transition.

In each of the phases, conservation of mass and momentum has to hold, yielding the Navier-Stokes equations in the two domains $\Omega_i,\ i = 1, 2$

$$\begin{cases} \rho_i(\dfrac{\partial \mathbf{u}}{\partial t} + (\mathbf{u} \cdot \nabla \mathbf{u})) - \mathbf{div}\, \boldsymbol{\sigma}_i = \mathbf{f} \\ \nabla \cdot \mathbf{u} = 0 \end{cases} \quad \text{in} \quad \Omega_i(t), \tag{1.12}$$

We now consider coupling conditions at the interface. As the phases are viscous and no phase transition takes place, the velocity can be assumed to be continuous at the interface:

$$[\mathbf{u}] = 0 \quad on \quad \Gamma \tag{1.13}$$

Here for $\mathbf{x} \in \Gamma$ and a function f defined in a neighborhood of Γ, we define the jump across Γ by

$$[f](x) = [f]_\Gamma(x) := \lim_{h \to 0}(f(x - h\mathbf{n}_\Gamma(x)) - f(x + h\mathbf{n}_\Gamma(x))) \tag{1.14}$$

where $\mathbf{n}_\Gamma$ denotes the unit normal on Γ at $\mathbf{x}$, pointing form Ω_1 to Ω_2.

At the interface there acts a surface tension force which is due to the fact that on both sides of Γ there are different molecules that have different attractive forces. The surface tension force acting on the interface segment γ can be modeled by

$$F_3(t) = -\tau \int_{\gamma(t)} \kappa \mathbf{n}_\Gamma ds$$

The parameter τ is the surface tension coefficient, which is a material property of the two-phase system. This additional force term $F_3(t)$ has to be taken into account. If we consider conservation of momentum, then the equation (1.15) should be

$$\frac{d}{dt}M(t) = F_1(t) + F_2(t) + F_3(t) = \int_{\Omega(t)} (\mathbf{f} + \mathbf{div}\,\boldsymbol{\sigma})\, d\mathbf{x} - \int_{\partial\Omega_N} \tau\kappa\mathbf{n}_\Gamma ds \qquad (1.15)$$

Since the stress tensor σ is not necessarily smooth across Γ, we split Ω into $\partial\Omega_1$ and $\partial\Omega_2$

$$\int_{\partial\Omega(t)} \sigma\mathbf{n} ds = \int_{\partial\Omega_1(t)} \sigma_1\mathbf{n}_1 ds + \int_{\partial\Omega_2(t)} \sigma_2\mathbf{n}_2 ds - \tau\int_{\Gamma(t)} [\sigma]\mathbf{n}_\Gamma ds,$$

and apply the Stokes' theorem on Ω_1 and Ω_2 separately. Note that $\mathbf{u}_i$ is the outward normal on $\partial\Omega_i$ and $\mathbf{n}_\Gamma$ the normal at Γ, pointing from Ω_1 to Ω_2. Thus we obtain

$$\begin{aligned}\int_{\Omega(t)} \rho_i(\frac{\partial\mathbf{u}}{\partial t} + (\mathbf{u}\cdot\nabla\mathbf{u}))dx \\ = \int_{\Omega_1(t)} \mathbf{div}\,\boldsymbol{\sigma}_i dx + \int_{\Omega_2(t)} \mathbf{div}\,\boldsymbol{\sigma}_2 dx + \int_{\Omega(t)} dx - \int_{\Gamma(t)} ([\boldsymbol{\sigma}]\mathbf{n}_\gamma - \tau\kappa\mathbf{n}_\gamma)\, ds \qquad (1.16)\end{aligned}$$

1.2 Boundary conditions

Modeling of fluid flows in the presence of solid bodies and free interfaces is a general problem in science and engineering, and requires some assumptions about the nature of the fluid motion (the boundary condition) at the solid surface and rheology of the interface [61]. For the boundary conditions we distinguish between essential and

natural boundary conditions. Let $\partial\Omega$ be subdivided into two parts $\partial\Omega = \Gamma_D \cup \Gamma_N$ with $\Gamma_D \cap \Gamma_N = \emptyset$. We use essential boundary conditions on Γ_D that are of Dirichlet type. In applications these describe inflow conditions or conditions at walls. Such Dirichlet conditions are of the form

$$\mathbf{u}(\mathbf{x}, t) = \mathbf{u}_D(\mathbf{x}, t) \quad on \quad \Gamma_D \tag{1.17}$$

with a given $\mathbf{u}_D(\mathbf{x}, t)$.

No-slip boundary condition is one of the simplest essential boundary conditions used to describe conditions at walls. No-slip boundary condition, which states that at a solid boundary the fluid will have zero velocity relative to the boundary, has remarkable success in reproducing the characteristic of many types of flow, however, there exist situations in which it leads to singular or unrealistic behavior–for example, the spreading of a liquid on a solid substrate [60], corner flow and the extrusion of polymer melts from a capillary tube [61].

Numerous boundary conditions that allow for finite slip at the solid interface have been used to rectify these difficulties. The Navier boundary condition is a slip boundary condition that assume that the tangential "slip" velocity, rather than zero, is proportional to the tangential stress. With a factor of proportionality a in $L^\infty(\Gamma)$, we can express the Navier boundary condition for a sufficiently regular vector field $\mathbf{u}$ as

$$\mathbf{u} \cdot \mathbf{n} = 0 \text{ and } 2\mu(\mathbf{n} \cdot \mathrm{D}(\mathbf{u})) \cdot \tau + \mathrm{a}\mathbf{u} \cdot \tau = 0 \text{ on } \Gamma$$

A boundary condition on a free surface results from balancing the strain (surface tension) and stress on the free surface

$$\boldsymbol{\sigma}\mathbf{n}_\Gamma = -\gamma\kappa\mathbf{n} - p_{ext}\mathbf{n} \quad \text{on} \quad \Gamma_N(t), \tag{1.18}$$

where γ is the surface tension coefficient which is a material property, κ is the mean curvature, for which

$$\kappa(\mathbf{x}) = \mathbf{div}\,\mathbf{n}_\Gamma(\mathbf{x}) \quad on \quad \Gamma_N(t),$$

holds.

On the free surface Γ, there is no flow through this boundary, so we impose the kinematic condition

$$u_\Gamma = \mathbf{u}_\Gamma \cdot \mathbf{n}_\Gamma \tag{1.19}$$

where u_Γ is the normal velocity of the free surface $\Gamma(t)$.

1.3 Free Surface Capturing Methods

An interface between a gas and a liquid is often referred to as a free surface. The reason for the free designation arises from the large difference in the densities of the gas and liquid (e.g., the ratio of density for water to air is 1000). A low gas density means that its inertia can generally be ignored compared to that of the liquid. In this sense the liquid moves independently, or freely, with respect to the gas. The only influence of the gas is the pressure it exerts on the liquid surface. In other

words, the gas-liquid surface is not constrained, but free. Free surfaces require the introduction of special methods to define their locations, their movements, and their influences on a flow. Numerical simulations for a moving free surface are complicated and difficult, the situation is further complicated if the boundaries are in motion or moving bodies are present in the fluid system. In this section, we review the most important approaches for describing the motion of the interface.

1.3.1 Free Surface Tracking

For a velocity field $\mathbf{u}$ and a smooth interface $\Gamma(t)$ the trace $\mathbf{u}|_{\Gamma(t)}$ and the immiscibility condition $\mathbf{u}_\Gamma = \mathbf{u}\cdot\mathbf{n}$ are well-defined. The evolution of the interface can be described by using the Lagrangian coordinates. Take a (virtual) particle X on the interface at $t = t_0$ with Eulerian coordinates $\xi \in \Gamma(t_0)$. For $t \geq t_0$, let $X_\xi(t)$ be the Eulerian coordinates of this particle.

The particles on the interface are transported by the flow field, hence for $X_\xi(t)$ we have the ODE system

$$\begin{cases} \dfrac{d}{d\tau}X_\xi(\tau) = \mathbf{u}(X_\xi(\tau),\tau), \quad \tau \geq 0, \\ X_\xi(0) = \xi \end{cases} \tag{1.20}$$

$X_\xi(\tau)$ can be interpreted as the path of an infinitely small particle with initial position ξ.

For $\mathbf{u}(\mathbf{x},t)$ sufficiently smooth (Lipschitz with respect to $\mathbf{x}$), this system of ODEs has a unique solution. This defines the coordinate transformation $(\mathbf{x},t) =$

$(X_\xi(t), t) \to (\xi, t)$ from Eulerian coordinates $(\mathbf{x}, t)$ to Lagrangian coordinates (ξ, t).

And the interface $\Gamma(t)$ can be characterized as follows,

$$\mathbf{x} = \xi + \int_0^t \mathbf{u}(X_\xi(\tau), \tau) d\tau \tag{1.21}$$

The interface representation in (1.21) also forms the basis for a class of numerical methods, known as interface tracking. In these methods a collection of markers is put on a given interface $\Gamma(t_0)$ and then transported (numerically) by the flow field $\mathbf{u}$ to obtain the markers on the interface $\Gamma(t_0 + \Delta t)$. The collection of markers on $\Gamma(t_0)$ could be the set of vertices of a triangulation of $\Gamma(t_0)$. In such methods one usually has to redistribute the markers after a certain number of time steps. In general it is rather difficult to treat topology changes (e.g. collision of droplets) in a systematic and accurate way.

1.3.2 Volume tracking based on the level set function

Volume Tracking is based on the concept of a flow map $\phi(t, \mathbf{x})$, which is a function that maps the location $\mathbf{x}$ of a particle at one time t_0 to its position at another time t_1, thereby answering the question: 'Where will this particle go?' or 'Where did this particle come from?'[62]. Using a proper map, the evolution of any volume in the flow can be defined: If the volume at the starting time t_0 is V_{t_0}, and the volume at another time t is $V(t)$, we define $V(t)$ as the image of V_0 under the flow map as

$$V(t) = \phi(V_{t_0}).$$

The map ϕ is solved by an advection equation

$$\frac{\partial \phi}{\partial t} + \mathbf{u} \cdot \nabla \phi = 0 \tag{1.22}$$

So we can locate the new interface $\Gamma(t)$ by

$$\Gamma(t) = \phi(\Gamma_{t_0})$$

In this thesis we employ the surface capturing algorithm based on the implicit definition of $\Gamma(t)$ as the zero level of a globally defined function $\phi(t; \mathbf{x})$. A smooth (at least Lipschitz continuous) function ϕ such that

$$\phi(t, \mathbf{x}) = \begin{cases} < 0 & \text{if } \mathbf{x} \in \Omega(\text{t}) \\ > 0 & \text{if } \mathbf{x} \in \mathbb{R}^3 / \overline{\Omega(\text{t})} \; for \; all \; t \in [0, T] \\ = 0 & \text{if } \mathbf{x} \in \Gamma(\text{t}) \end{cases} \tag{1.23}$$

is called the level set function. The kinematic boundary condition $\mathbf{u}_\Gamma = \mathbf{u} \cdot \mathbf{n}$ implies that for $t > 0$ the level set function can be found as the solution to the transport equation:

$$\frac{\partial \phi}{\partial t} + \widetilde{\mathbf{u}} \cdot \nabla \phi = 0 \; in \; \mathbb{R}^3 \times (0, T]$$

where $\widetilde{\mathbf{u}}$ is any (divergence-free) smooth velocity field such that $\widetilde{\mathbf{u}} = \mathbf{u}$ on $\Gamma(t)$.

CHAPTER 2

Mathematical Model and Numerical Method

2.1 Mathematical Model for Free Surface Flow

We consider a Newtonian fluid flow with a free-surface and surface tension forces in section 2.1.1 and a full 3D model of vicoplastic fluid flow with a free-surface and surface tension forces in section 2.1.2. In section 2.1.3 we deduce a suitable variational inequality formulation satisfied by any sufficiently regular solution to the fluid model. Then, the variational inequality provides us with an energy balance in section 2.1.4.

2.1.1 Newtonian Fluild Model

Consider a Newtonian incompressible fluid flow in a bounded time-dependent domain $\Omega(t) \in \mathbb{R}^3$ for $t \in (0, T]$. We apply constitutive law (1.9) in (1.8), and then get the governing equation for fluid dynamics

$$\begin{cases} \rho(\dfrac{\partial \mathbf{u}}{\partial t} + (\mathbf{u} \cdot \nabla \mathbf{u})) - \mu \Delta \mathbf{u} + \nabla p = \mathbf{f} \\ \nabla \cdot \mathbf{u} = 0 \end{cases} \quad \text{in } \ \Omega(t), \tag{2.1}$$

The initial condition is the initial velocity filed and initial domain:

$$\Omega(0) = \Omega_0, \quad \mathbf{u}|_{t=0} = \mathbf{u}_0, \quad \nabla \cdot \mathbf{u}_0 = 0. \tag{2.2}$$

We assume that the entire boundary of the whole domain is a free surface $\Gamma(t)$ which passively evolves with the normal velocity of fluid, i.e., the following kinematic condition is valid.

$$u_\Gamma = \mathbf{u} \cdot \mathbf{n} \quad \text{on } \ \Gamma(t), \tag{2.3}$$

where $\mathbf{n}$ is the unit external normal vector on $\Gamma(t)$ and u_Γ is the normal velocity of $\Gamma(t)$. Another boundary condition on $\Gamma(t)$ results from balancing the surface tension forces and the fluid stress forces:

$$\boldsymbol{\sigma}\mathbf{n}|_\Gamma = -\gamma\kappa\mathbf{n} - p_{ext}\mathbf{n} \quad \text{on } \ \Gamma(t), \tag{2.4}$$

where $\boldsymbol{\sigma} = \mu[\nabla \mathbf{u} + \nabla \mathbf{u}^T] + pI$ is the stress tensor of the fluid, κ is the sum of principal

curvatures, γ is the surface tension coefficient, p_{ext} is an exterior pressure which we set to be zero for the rest of the paper, $p_{ext} = 0$.

The system of equations (2.1), boundary condtions (2.3), (2.4) and intial condition (2.2) form a mathematical formulation of the problem of the Newtonian incompuressible fluid flow with free-surface.

2.1.2 Visco-plastic Fluid Model

A common choice to describle the dynamics of viscoplastic flow is to use Herschel-Bulkley constitutive law:

$$\begin{aligned} \boldsymbol{\tau} = (K|\mathbf{Du}|^{\alpha-1} + \tau_s|\mathbf{Du}|^{-1})\mathbf{Du} \quad &\Leftrightarrow \quad |\boldsymbol{\tau}| > \tau_s \\ \mathbf{Du} = 0 \quad &\Leftrightarrow \quad |\boldsymbol{\tau}| \leq \tau_s \end{aligned} \tag{2.5}$$

in the governing equations (1.8)

$$\begin{cases} \rho(\dfrac{\partial \mathbf{u}}{\partial t} + (\mathbf{u} \cdot \nabla \mathbf{u})) - \mathbf{div}\, \boldsymbol{\sigma} = \mathbf{f} \\ \nabla \cdot \mathbf{u} = 0 \end{cases} \quad \text{in } \ \Omega(t), \tag{2.6}$$

K is the consistency parameter, τ_s is yield stress and α is flow index. The most important feature of a viscoplastic fluid is its yield stress: Once the stresses exceed a positive threshold parameter, the material flows like a fluid. Otherwise, it behaves like a solid. To account for such a two-fold behaviour, one imposes conditioned constitutive relations between the strain-rate tensor $\mathbf{Du} = \frac{1}{2}[\nabla \mathbf{u} + (\nabla \mathbf{u})^T]$ and $\boldsymbol{\tau}$,

the deviatoric part of the stress tensor, $\boldsymbol{\sigma}_{ij} = \boldsymbol{\tau}_{ij} - p\delta_{ij}$, with pressure p.

The system of equation (2.6), boundary condtions (2.3), (2.4) and intial condition (2.2) form a mathematical formulation of the problem of the Herschel-Bulkley incompressible fluid flow with free-surface. The problem is challenging for analysis and only partial results are known regarding its well-posedness, see, e.g. [11, 18] and the reference therein for analysis of wall-bounded Herschel-Bulkley flows.

2.1.3 Variational Inequality

In this section, we show that any solution to (2.2)–(2.5) (if it possesses certain smoothness) and (2.6), satisfies a variational inequality.

For arbitrary smooth divergence-free vector field $\mathbf{v}$, we first take the scalar product of the first equation in (2.6) with $\mathbf{v} - \mathbf{u}$. This gives the relation

$$\rho(\frac{\partial \mathbf{u}}{\partial t} + (\mathbf{u} \cdot \nabla \mathbf{u})) \cdot (\mathbf{v} - \mathbf{u}) - \mathbf{div}\, \boldsymbol{\sigma} \cdot (\mathbf{v} - \mathbf{u}) = \mathbf{f} \cdot (\mathbf{v} - \mathbf{u}) \quad \text{on } \Omega(t), \tag{2.7}$$

for all $t > 0$. Further we integrate (2.7) over $\Omega(t)$ and obtain the identity

$$\int_{\Omega(t)} \left\{ \rho(\frac{\partial \mathbf{u}}{\partial t} + (\mathbf{u} \cdot \nabla \mathbf{u}))(\mathbf{v} - \mathbf{u}) + \mathbf{div}\, \boldsymbol{\sigma} \cdot (\mathbf{v} - \mathbf{u}) - \mathbf{f} \cdot (\mathbf{v} - \mathbf{u}) \right\} \mathrm{d}\mathbf{x} = 0$$

Then applying divergence theorem to the term $\mathbf{div}\, \boldsymbol{\sigma} \cdot (\mathbf{v} - \mathbf{u})$, we get

$$\int_{\Omega(t)} \left\{ \rho(\frac{\partial \mathbf{u}}{\partial t} + (\mathbf{u} \cdot \nabla \mathbf{u}))(\mathbf{v} - \mathbf{u}) + \boldsymbol{\sigma} : \nabla(\mathbf{v} - \mathbf{u}) - \mathbf{f} \cdot (\mathbf{v} - \mathbf{u}) \right\} \mathrm{d}\mathbf{x} = \int_{\Gamma(t)} \boldsymbol{\sigma}(\mathbf{v} - \mathbf{u}) \cdot \mathbf{n}\, \mathrm{d}\mathbf{s}$$

Now we employ dynamics condition (2.4) and note that the symmetry of the Cauchy tensor leads to the identity $\boldsymbol{\sigma} : \nabla(\mathbf{v} - \mathbf{u}) = \boldsymbol{\sigma} : (\mathbf{Dv} - \mathbf{Du})$.

This brings us to the equality

$$\int_{\Omega(t)} \left\{ \rho(\frac{\partial \mathbf{u}}{\partial t} + (\mathbf{u} \cdot \nabla \mathbf{u}))(\mathbf{v} - \mathbf{u}) + \boldsymbol{\sigma} : (\mathbf{Dv} - \mathbf{Du}) - \mathbf{f} \cdot (\mathbf{v} - \mathbf{u}) \right\} \mathrm{d}\mathbf{x} = - \int_{\Gamma(t)} \gamma \kappa \mathbf{n} \cdot (\mathbf{v} - \mathbf{u}) \, \mathrm{d}\mathbf{s}. \quad (2.8)$$

As the next step, we decompose the stress tensor into deviatoric and volumetric parts: $\boldsymbol{\sigma} = \boldsymbol{\tau} - p\mathbf{I}$ (the decomposition is formal in the plug region). We treat the stress term in (2.8) separately in the flow and plug regions of $\Omega(t)$. For the flow region $\Omega_f(t)$, we employ the first constitutive relation from (2.5) and further apply the Cauchy-Schwarz inequality $\mathbf{Du} : \mathbf{Dv} \leq |\mathbf{Du}||\mathbf{Dv}|$. We get

$$\begin{aligned} \int_{\Omega_f(t)} \boldsymbol{\sigma} : (\mathbf{Dv} - \mathbf{Du}) \, \mathrm{d}\mathbf{x} &= \int_{\Omega_f(t)} (K|\mathbf{Du}|^{\alpha-1} + \tau_s |\mathbf{Du}|^{-1}) \mathbf{Du} : (\mathbf{Dv} - \mathbf{Du}) \, \mathrm{d}\mathbf{x} \\ &= \int_{\Omega_f(t)} \left\{ K|\mathbf{Du}|^{\alpha-1} \mathbf{Du} : (\mathbf{Dv} - \mathbf{Du}) + \tau_s \left(|\mathbf{Du}|^{-1} (\mathbf{Du} : \mathbf{Dv}) - |\mathbf{Du}| \right) \right\} \mathrm{d}\mathbf{x} \\ &\leq \int_{\Omega_f(t)} \left\{ K|\mathbf{Du}|^{\alpha-1} \mathbf{Du} : (\mathbf{Dv} - \mathbf{Du}) + \tau_s (|\mathbf{Dv}| - |\mathbf{Du}|) \right\} \mathrm{d}\mathbf{x} \end{aligned} \quad (2.9)$$

The pressure term disappears above since both $\mathbf{v}$ and $\mathbf{u}$ are divergence free. The same arguments and the second constitutive relation from (2.5) give for the plug

region $\Omega_p(t) = \Omega(t) \setminus \overline{\Omega}_f(t)$:

$$\begin{aligned}\int_{\Omega_p(t)} \boldsymbol{\sigma} : (\mathbf{Dv} - \mathbf{Du})\,\mathrm{d}\mathbf{x} &= \int_{\Omega_p(t)} \boldsymbol{\tau} : \mathbf{Dv}\,\mathrm{d}\mathbf{x} \\ &\le \sup_{\Omega_p(t)} |\boldsymbol{\tau}| \int_{\Omega_p(t)} |\mathbf{Dv}|\,\mathrm{d}\mathbf{x} \le \tau_s \int_{\Omega_p(t)} |\mathbf{Dv}|\,\mathrm{d}\mathbf{x} \\ (\text{since } |\mathbf{Du}| = 0) &= \int_{\Omega_p(t)} \left\{ K|\mathbf{Du}|^{\alpha-1}\mathbf{Du} : (\mathbf{Dv} - \mathbf{Du}) + \tau_s(|\mathbf{Dv}| - |\mathbf{Du}|) \right\} \mathrm{d}\mathbf{x}\end{aligned} \tag{2.10}$$

Substituting (2.9) and (2.10) back into (2.8) gives the inequality

$$\begin{aligned}\int_{\Omega(t)} \left\{ \rho(\frac{\partial \mathbf{u}}{\partial t} + \mathbf{u}\cdot\nabla\mathbf{u})\cdot(\mathbf{v}-\mathbf{u}) + K|\mathbf{Du}|^{\alpha-1}\mathbf{Du} : (\mathbf{Dv}-\mathbf{Du}) + \tau_s(|\mathbf{Dv}| - |\mathbf{Du}|) \right\} \mathrm{d}\mathbf{x} \\ - \int_{\Omega(t)} \mathbf{f}\cdot(\mathbf{v}-\mathbf{u})\,\mathrm{d}\mathbf{x} + \int_{\Gamma(t)} \gamma\kappa\mathbf{n}\cdot(\mathbf{v}-\mathbf{u})\,\mathrm{d}\mathbf{s} \ge 0\end{aligned} \tag{2.11}$$

The arguments in this section are valid if a solution $\mathbf{u}$ is sufficiently smooth. The sufficient regularity assumptions would be $\mathbf{u} \in W^{1,\alpha+1}(\Omega(t))$, $\frac{\partial \mathbf{u}}{\partial t} \in L^2(\Omega(t))$, α is the same as in (2.5), and $\Omega(t)$ is bounded and has C^2 boundary for almost all $t > 0$. $W^{1,\alpha+1}(\Omega(t))$ is a Sobolev space defined as

$$W^{p,k} = \left\{ \mathbf{u} \in L^p(\Omega(t)) : D^i\mathbf{u} \in L^p(\Omega(t)) \ \ \forall |i| \le k \right\}$$

For the case of general boundary condition on the normal stress tensor, inequality (2.11) is found in [30].

We summarize the result of this section: *A sufficiently smooth solution* $\mathbf{u}$ *to* (2.6), (2.2)–(2.5) *satisfies the variational inequality* (2.11) *for almost all* $t > 0$ *and for any* $\mathbf{v} \in H^1(\Omega(t))$ *such that* $\mathbf{div}\,\mathbf{v} = 0$.

2.1.4 Energy balance

The energy balance for the solution to the free-surface flow problem (2.2)–(2.5) and (2.6) follows from the variational inequality (2.11). To show this, we first recall a few helpful identities. We shall assume that $\Gamma(t)$ is sufficiently smooth and closed for all $t \in [0,T]$. For a smooth function g defined on $\bigcup_{t\in[0,T]} \Omega(t) \times \{t\}$, the Reynolds transport theorem gives the relation

$$\frac{d}{dt}\int_{\Omega(t)} g \,\mathrm{d}\mathbf{x} = \int_{\Omega(t)} \frac{\partial g}{\partial t}\mathrm{d}\mathbf{x} + \int_{\Gamma(t)} v_\Gamma g \,\mathrm{d}\mathbf{s}. \tag{2.12}$$

Thanks to the kinematic condition (2.3) on the normal velocity of Γ and $\mathrm{div}\mathbf{u} = 0$, (2.12) yields the identity

$$\frac{d}{dt}\int_{\Omega(t)} g \,\mathrm{d}\mathbf{x} = \int_{\Omega(t)} \left(\frac{\partial g}{\partial t} + (\mathbf{u}\cdot\nabla)g\right) \mathrm{d}\mathbf{x}. \tag{2.13}$$

Recall the definition of the surface gradient and divergence operators:

$$\nabla_\Gamma q = \nabla q - (\mathbf{n}\cdot\nabla q)\mathbf{n}$$

and

$$\mathrm{div}_\Gamma \mathbf{g} = \mathrm{tr}(\nabla_\Gamma \mathbf{g})$$

which are the intrinsic surface quantities and do not depend on extensions of a scalar function q and a vector function $\mathbf{g}$ off the surface. The integration by parts formula

over a closed smooth surface Γ reads

$$\int_\Gamma \left(q(\mathrm{div}_\Gamma \mathbf{g}) + \mathbf{g} \cdot \nabla_\Gamma q \right) \mathrm{d}\mathbf{s} = \int_\Gamma \kappa(\mathbf{g} \cdot \mathbf{n}) q \, \mathrm{d}\mathbf{s}, \tag{2.14}$$

where κ denotes the (doubled) surface mean curvature as in (2.11). Finally, for $\Gamma(t)$ passively advected by a flow field $\mathbf{u}$, the Leibniz formula gives

$$\frac{d}{dt} \int_{\Gamma(t)} g \, \mathrm{d}\mathbf{s} = \int_{\Gamma(t)} \left(\frac{\partial g}{\partial t} + (\mathbf{u} \cdot \nabla) g + g \, \mathrm{div}_\Gamma \mathbf{u} \right) \mathrm{d}\mathbf{s}. \tag{2.15}$$

Now we are prepared to deduce the energy balance from (2.11). As the first step, we test (2.11) with $\mathbf{v} = 0$,

$$\int_{\Omega(t)} \left\{ \rho(\frac{\partial \mathbf{u}}{\partial t} + \mathbf{u} \cdot \nabla \mathbf{u}) \cdot (-\mathbf{u}) - K|\mathbf{D}\mathbf{u}|^{\alpha+1} + \tau_s(-|\mathbf{D}\mathbf{u}|) \right\} \mathrm{d}\mathbf{x} \\ - \int_{\Omega(t)} \mathbf{f} \cdot (-\mathbf{u}) \, \mathrm{d}\mathbf{x} + \int_{\Gamma(t)} \gamma\kappa\mathbf{n} \cdot (-\mathbf{u}) \, \mathrm{d}\mathbf{s} \geq 0 \tag{2.16}$$

and $\mathbf{v} = 2\mathbf{u}$,

$$\int_{\Omega(t)} \left\{ \rho(\frac{\partial \mathbf{u}}{\partial t} + \mathbf{u} \cdot \nabla \mathbf{u}) \cdot \mathbf{u} + K|\mathbf{D}\mathbf{u}|^{\alpha+1} + \tau_s|\mathbf{D}\mathbf{u}| \right\} \mathrm{d}\mathbf{x} \\ - \int_{\Omega(t)} \mathbf{f} \cdot \mathbf{u} \, \mathrm{d}\mathbf{x} + \int_{\Gamma(t)} \gamma\kappa\mathbf{n} \cdot \mathbf{u} \, \mathrm{d}\mathbf{s} \geq 0 \tag{2.17}$$

Comparing two resulting inequalities, we obtain the equality

$$\int_{\Omega(t)} \left\{ \rho(\frac{\partial \mathbf{u}}{\partial t} \cdot \mathbf{u} + (\mathbf{u} \cdot \nabla \mathbf{u}) \cdot \mathbf{u}) + K|\mathbf{D}\mathbf{u}|^{\alpha+1} + \tau_s|\mathbf{D}\mathbf{u}| \right\} \mathrm{d}\mathbf{x} + \int_{\Gamma(t)} \gamma\kappa\mathbf{n}\cdot\mathbf{u} \, \mathrm{d}\mathbf{s} = \int_{\Omega(t)} \mathbf{f}\cdot\mathbf{u} \, \mathrm{d}\mathbf{x}.$$

We rewrite the first two terms as $\frac{1}{2}\int_{\Omega(t)}\rho(\frac{\partial|\mathbf{u}|^2}{\partial t}+\mathbf{u}\cdot\nabla|\mathbf{u}|^2)\,\mathrm{d}\mathbf{x}$ and apply the Reynolds transport formula. This gives the identity

$$\frac{d}{dt}\int_{\Omega(t)}\frac{\rho|\mathbf{u}|^2}{2}\mathrm{d}\mathbf{x}+\int_{\Omega(t)}\left(K|\mathbf{D}\mathbf{u}|^{\alpha+1}+\tau_s|\mathbf{D}\mathbf{u}|\right)\mathrm{d}\mathbf{x}+\int_{\Gamma(t)}\gamma\kappa\mathbf{n}\cdot\mathbf{u}\,\mathrm{d}\mathbf{s}=\int_{\Omega(t)}\mathbf{f}\cdot\mathbf{u}\,\mathrm{d}\mathbf{x}. \tag{2.18}$$

With the help of integration by parts (2.14) over $\Gamma=\Gamma(t)$ and the Leibniz formula we calculate:

$$\int_{\Gamma(t)}\kappa(\mathbf{n}\cdot\mathbf{u})\mathrm{d}\mathbf{s}=\int_{\Gamma(t)}\mathrm{div}_\Gamma\mathbf{u}\mathrm{d}\mathbf{s}=\frac{d}{dt}\int_{\Gamma(t)}1\mathrm{d}\mathbf{s}=\frac{d}{dt}|\Gamma(t)|$$

where $|\Gamma(t)|$ denotes the area of the free surface. Employing these relations in (2.18) leads to the following *energy balance for the solution of* (2.2)–(2.5), (2.6):

$$\frac{d}{dt}\left(\int_{\Omega(t)}\frac{\rho|\mathbf{u}|^2}{2}\mathrm{d}\mathbf{x}+\gamma|\Gamma(t)|\right)+\int_{\Omega(t)}\left(K|\mathbf{D}\mathbf{u}|^{\alpha+1}+\tau_s|\mathbf{D}\mathbf{u}|\right)\mathrm{d}\mathbf{x}=\int_{\Omega(t)}\mathbf{f}\cdot\mathbf{u}\,\mathrm{d}\mathbf{x}. \tag{2.19}$$

The energy balance (2.19) has the form

$$\frac{d}{dt}E_{\mathrm{total}}(t)=-D(t)+W_{\mathrm{ext}}(t),$$

where the total energy $E_{\mathrm{total}}(t)$ is the sum of kinetic energy $E_{\mathrm{kin}}(t)=\int_{\Omega(t)}\frac{\rho|\mathbf{u}|^2}{2}\mathrm{d}\mathbf{x}$ and potential energy $E_{\mathrm{free}}(t)=\gamma|\Gamma(t)|+\mathrm{const}$. The rate of change of E_{total} is balanced by the internal energy dissipation

$$D(t)=\int_{\Omega(t)}\left(K|\mathbf{D}\mathbf{u}|^{\alpha+1}+\tau_s|\mathbf{D}\mathbf{u}|\right)\mathrm{d}\mathbf{x} \tag{2.20}$$

and the work of external forces

$$W_{\text{ext}}(t) = \int_{\Omega(t)} \mathbf{f} \cdot \mathbf{u} \, \mathrm{d}\mathbf{x}.$$

2.2 Numerical Method

One of the difficult features of the problem for simulating viscoplastic flows is that two regions are unknown a priori. To avoid this difficulty, we regularize the problem by enforcing the fluidic medium behavior in the entire computational domain (see, e.g., [8, 20]). We use $|\mathbf{Du}|_\varepsilon = \sqrt{|\mathbf{Du}|^2 + \varepsilon^2}$ to replace $|\mathbf{Du}|$, where $\varepsilon > 0$ is a very small constant (we set $\varepsilon = 10^{-6}$ in our numerical method). Now the governing equation for the whole domain is:

$$\begin{cases} \rho(\dfrac{\partial \mathbf{u}}{\partial t} + (\mathbf{u} \cdot \nabla \mathbf{u})) - \mathbf{div}\, \boldsymbol{\mu_\varepsilon} \boldsymbol{Du} + \nabla p = \mathbf{f} \\ \nabla \cdot \mathbf{u} = 0 \end{cases} \quad \text{in} \;\; \Omega(t), \tag{2.21}$$

with the shear-dependent effective viscosity

$$\mu_\varepsilon = K|\mathbf{Du}|_\varepsilon^{\alpha-1} + \tau_s|\mathbf{Du}|_\varepsilon^{-1}$$

The initial condition and kinetic boundary condition are the same as in section 2.1.1:

$$\Omega(0) = \Omega_0, \quad \mathbf{u}|_{t=0} = \mathbf{u}_0, \quad \nabla \cdot \mathbf{u}_0 = 0. \tag{2.22}$$

$$u_\Gamma = \mathbf{u} \cdot \mathbf{n} \quad \text{on} \;\; \Gamma(t), \tag{2.23}$$

The dynamics boundary condition is different:

$$\boldsymbol{\sigma}_\varepsilon \mathbf{n}|_\Gamma = -\gamma\kappa\mathbf{n} - p_{ext}\mathbf{n} \quad \text{on} \quad \Gamma(t), \tag{2.24}$$

where $\boldsymbol{\sigma}_\varepsilon = \mu_\varepsilon \mathbf{D}\mathbf{u} + pI$ is the regularized stress tensor of the fluid.

We employ the surface capturing algorithm based on the implicit definition of $\Gamma(t)$ as the zero level of a globally defined function $\phi(t;x)$. A smooth (at least Lipschitz continuous) function ϕ such that (1.23) holds.

The initial condition (2.22) allows us to define $\phi(0;x)$. For $t > 0$ the level set function satisfies the following transport equation [46]:

$$\frac{\partial \phi}{\partial t} + \tilde{\mathbf{u}} \cdot \nabla\phi = 0 \quad in \quad \mathbb{R}^3 \times (0,T], \tag{2.25}$$

where $\tilde{\mathbf{u}}$ is any smooth velocity field such that $\tilde{\mathbf{u}} = \mathbf{u}$ on $\Gamma(t)$. The employed mathematical model consists of Eqs. (2.21), (2.22), (2.23), (2.24) and (2.25). We note that the implicit definition of $\Gamma(t)$ as zero level of a globally defined function ϕ leads to numerical algorithms which can easily handle complex topological changes of the free surface such as merging or pinching of two fronts and formation of singularities.

The level set function provides an easy access to useful geometric characteristics of $\Gamma(t)$. For instance, the unit outward normal to $\Gamma(t)$ is $n_\Gamma = \nabla\phi/|\nabla\phi|$, and the surface curvature is $\kappa = \nabla \cdot \mathbf{n}_\Gamma$. From the numerical point of view, it is often beneficial if the level set function possesses the signed distance property, i.e. it satisfies the

Eikonal equation

$$|\nabla\phi| = 1$$

The Numerical method applied in all our numerical experiments is based on the level set method for capturing the free surface evolution and on locally refined and dynamically adapted octree cartesian staggered grids for the discretization of fluid and level set equations. The numerical approach we use has been developed in [43, 44, 45]. To approximate complex geometries emerging in the process of the free surface evolutions we use adaptive cartesian grids dynamically refined near the free surfaces and coarsened in the fluid interior. For the application of such grids in image processing, the visualization of amorphous medium, free surface Newtonian ow computations and other applications where non-trivial geometries occur see, [36], [39],[42],[49],[57]. We combine the mesh adaptation with a splitting algorithm for time integration.

2.2.1 Numerical time integration

For the spatial discretization we use octree cubic meshes, which allow fast dynamic mesh adaptation based on geometric or error indicators, the detail can be found in [43] and the next section. In this section we ignore the spatial discretization for the purpose of presentation. The time integration algorithm that we applied is a projection method due to Chorin, Yanenko, Pironneau and others, see, for example, [14],[48]. In our notation $\mathbf{u}^n$, p^n, ϕ^n are the velocity field, the pressure, and the level set function at $t = t_n$, respectively. Function ϕ^n implicitly defines an approximation

to fluid domain at time $t = t_n$ through $\Omega_n := \{\mathbf{x} \in \mathbb{R}^3 \,:\, \phi^n(\mathbf{x}) < 0\}$.

We assume that $\mathbf{u}^0 = \mathbf{u}(t_0)$ and $\phi^0 = \phi(t_0)$ since initial velocity field and domain is known. Given $\mathbf{u}^n$, ϕ^n such that $\mathbf{div}\,\mathbf{u}^n = 0$, we find $\mathbf{u}^{n+1}$, p^{n+1}, ϕ^{n+1} in several steps:

The semi-Lagrangian step for solving level set function $\Omega_n \to \Omega_{n+1}$. Extend divergence free velocity field to the exterior domain: $\mathbf{u}^n|_{\Omega_n} \to \widetilde{\mathbf{u}}^n|_{\mathbb{R}^3}$, where the extension domain is a bulk computational domain in our algorithm.

Find ϕ^{n+1} from (2.25) by a numerical intergration with the semi-Lagrangian method [59]. For every $\mathbf{y} \in \mathbb{R}^3$, solve the characteristic equation backward in time

$$\frac{\partial \mathbf{x}(\tau)}{\partial \tau} = \widetilde{\mathbf{u}}^n(\mathbf{x}(\tau)), \quad \mathbf{x}(t_{n+1}) = \mathbf{y}, \quad \text{for } \tau \in [t_{n+1}, t_n]. \tag{2.26}$$

The mapping $\mathbf{X} : \mathbf{y} \to \mathbf{x}(t_n)$ defines an isomorphism on $\mathbb{R}^3$:

$$\phi^{n+1}(\mathbf{y}) = \phi^n(\mathbf{X}(\mathbf{y})). \tag{2.27}$$

This mapping help us to determine new boundary $\Gamma_{n+1} = \{\mathbf{y} : |\phi^{n+1}(\mathbf{y}) = 0\}$ by updating the information from $\phi^n(\mathbf{y})$.

Remeshing. Given the new fluid domain we update and adapt the grid to account for the new position of the free surface. The adaptation is based on the information about the distance to the free surface provided by ϕ^{n+1}.

Re-interpolation. After remeshing we re-interpolate all discrete variables to the new

grid. The re-interpolated velocity field is defined on the bulk computational domain (due to the extension procedure at the beginning of the level-set part).

Next we handle viscoplastic terms and project the velocity into (discretely) divergence-free functions subspace and recover the new pressure.

The convection-diffusion step: Solve for $\widetilde{\mathbf{u}^{n+1}}$ in Ω_{n+1}:

$$\begin{cases} \dfrac{\widetilde{\mathbf{u}^{n+1}} - \mathbf{u}^n}{\triangle t_n} + G \circ (\mathbf{u}^{n+\frac{1}{2}}) \cdot \dfrac{\nabla\widetilde{\mathbf{u}^{n+1}} + \nabla\mathbf{u}^n}{2}) - \dfrac{1}{2}\,\mathbf{div}(\mu_\varepsilon^n(\mathbf{u}^{n+\frac{1}{2}})(D\mathbf{u}^n + D\widetilde{\mathbf{u}^{n+1}})) = -\nabla p^n, \\ (\nabla\widetilde{\mathbf{u}^{n+1}} + \nabla\widetilde{\mathbf{u}^{n+1}}^T)\mathbf{n}\Big|_\Gamma = 0. \end{cases} \tag{2.28}$$

Where the operator G is a filter, which is needed to stabilize staggered grid discretizations on the octree meshes, $\mathbf{u}^{n+\frac{1}{2}} = \mathbf{u}^n + \xi(\mathbf{u}^n + \mathbf{u}^{n-1})$ with $\xi = \Delta t_n/\Delta t_{n-1}$.

The projection step: Project $\widetilde{\mathbf{u}^{n+1}}$ on the divergence-free space to recover $\mathbf{u}^{n+1}$:

$$\begin{cases} \alpha(\mathbf{u}^{n+1} - \widetilde{\mathbf{u}^{n+1}})/\triangle t_n - \nabla q = 0, \\ \mathbf{div}\,\mathbf{u}^{n+1} = 0, \\ q|_\Gamma = 0. \end{cases} \tag{2.29}$$

The problem (2.29) is reduced to the Poisson problem for q:

$$\begin{cases} -\Delta q = \alpha/\triangle t_n \,\mathrm{div}\,\widetilde{\mathbf{u}^{n+1}}, \\ q|_\Gamma = \tau\kappa^{n+1}. \end{cases} \tag{2.30}$$

Finally, update the pressure:

$$p^{n+1} = p^n - q + \mu_\varepsilon \, \mathbf{div} \, \widetilde{\mathbf{u}^{n+1}}. \tag{2.31}$$

The 'extra' divergence term in the pressure correction step (2.31) is used to reduce numerical boundary layers in the pressure, see, e.g., [25], [50].

2.2.2 Spartial discretization

For the spatial discretization we apply dynamic octree cubic meshes instead of the uniform mesh, since adapative meshes are cost-efficient comparing to the uniform mesh. Octree meshes allow fast reconstruction.

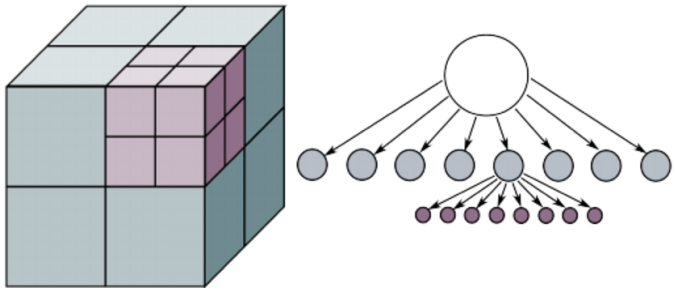

Figure 2.1: An octree mesh (left) and its representation as a tree (right).

The adaptation method is based on the graded refinement with cubic cells, see Fig. 2.1. An octree mesh is *graded* if the size of cells sharing (a part of) an edge or a face can differ in size only by the factor of two. This restriction simplifies support of mesh connectivity and the construction of discrete differential operators. We use the staggered location of velocity and pressure unknowns. The pressure degrees of

freedom are assigned to cells centers and velocity variables are located at cells faces in such a way that every face stores normal velocity flux. If a face is shared by cells from different grid levels, then velocity degrees of freedom are assigned to the faces centers of fine grid cells (in the case of graded octree mesh, the corresponding face of the coarse grid cell holds 4 unknowns).

At time t_n, the free surface $\Gamma(t_{n+1})$ is recovered by solving the characteristic equation (2.26) with the predicted location at time t_n and current velocity $\mathbf{u}^n$. The grid refinement towards the predicted interface location is done in order to reduce the loss of the local surface geometric information which occurs if Γ_{n+1} is approximated by a trilinear function on a coarser grid; such possible loss is illustrated in Fig 2.2. Note, that the predicted location may slightly differ from the actually computed $\Gamma(t_{n+1})$ in the level set part of the algorithm, since the mesh adaptation step is performed before the velocity is updated in the fluid part of the algorithm. However, this allows us to preserve most of the local surface geometry and avoids double remeshing. Details on how quadtree/octree structures can be efficiently handled computationally are found in [54].

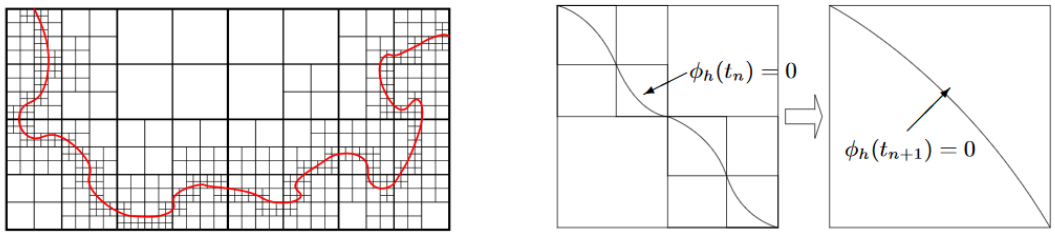

Figure 2.2: Left:2D quadtree grid adapted to free boundary. Right:The loss of discrete free surface geometric information when ϕ_h is transported from a region with finer mesh to the one with a coarser mesh

The constructed spacial discretization is hybrid: a finite volume method was used to handle incompressibility constrain and inertia terms, while a finite difference method was applied to diffusion terms and pressure gradient. Here we will discuss the discretization of gradient ∇_h, the advective term $\mathbf{u}\nabla\mathbf{u}$, the diffusion term $\mathbf{div}\,\mu_\varepsilon D\mathbf{u}$ and the divergence $\mathbf{div}$.

First we introduce the discrete gradient. We can define it as the adjoint of the discrete divergence. However, an approximation of ∇_h based on the formal Taylor expansions gives more accurate results. Pressure gradient has to be assigned to every internal face of the grid.

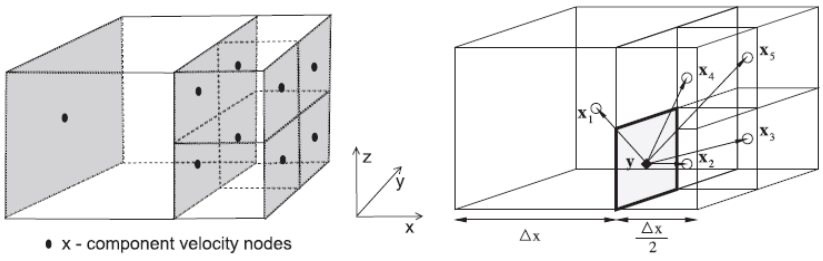

Figure 2.3: Left:Each shared face holds a node for velocity x-component.The nodes are located at faces barycenters. Right: Discretization stencil for $\frac{\partial p}{\partial x}$

For every internal face we assign the corresponding component of $\nabla_h p$ as follows. Since the octree mesh is graded, there can be only two geometric cases. If a face is shared by two equal-size cells, then the central difference approximation is used. Otherwise consider Fig. 2.3, for the approximation of p_x at the face center node $\mathbf{y}$ one considers the centers of five surrounding cells $\mathbf{x}_1, \ldots, \mathbf{x}_5$ and expand the pressure

value $p(\mathbf{x}_i)$ with respect to $p(\mathbf{y})$:

$$p(\mathbf{x}_i) = p(\mathbf{y}) + \nabla p(\mathbf{y}) \cdot (\mathbf{x}_i - \mathbf{y}) + O(|\mathbf{x}_i - \mathbf{y}|^2).$$

Neglecting the second-order terms, we obtain the following over-determined system:

$$\begin{pmatrix} 1 & -\Delta/2 & \Delta/4 & \Delta/4 \\ 1 & \Delta/4 & 0 & 0 \\ 1 & \Delta/4 & \Delta/2 & 0 \\ 1 & \Delta/4 & 0 & \Delta/2 \\ 1 & \Delta/4 & \Delta/2 & \Delta/2 \end{pmatrix} \begin{pmatrix} p(\mathbf{y}) \\ p_x(\mathbf{y}) \\ p_y(\mathbf{y}) \\ p_z(\mathbf{y}) \end{pmatrix} = \begin{pmatrix} p(\mathbf{x}_1) \\ p(\mathbf{x}_2) \\ p(\mathbf{x}_3) \\ p(\mathbf{x}_4) \\ p(\mathbf{x}_5) \end{pmatrix}, \tag{2.32}$$

where $\Delta \equiv \Delta x$. The least squares solution of (2.32) gives the stencil for the x-component of the gradient:

$$p_x(\mathbf{y}) \approx \frac{1}{3\Delta}(p_2 + p_3 + p_4 + p_5 - 4p_1). \tag{2.33}$$

The superposition of the discrete gradient and divergence operators generally leads to the non-symmetric matrix for the pressure problem. However, the corresponding linear algebraic systems are solved efficiently by a Krylov subspace method with an appropriate preconditioner.

It was noted in [45] for octree staggered grids, the discrete Helmholtz decomposition, which essentially constitutes the projection step of the splitting scheme, is unstable due to oscillatory spurious *velocity* modes tailored to course-to-fine grid

interfaces. If the viscosity is sufficiently large, then such modes are suppressed, otherwise they propagate and destroy the accuracy of numerical solution. Following that paper we apply a linear low-pass filter, which eliminates the spurious modes and improves the accuracy of numerical solution significantly. The low-pass filter G acts on the coarse-to-fine grid interface Γ_{cf}:

$$G \circ u(\mathbf{x}) = \begin{cases} \dfrac{1}{4}\displaystyle\sum_{i=1}^{4} u(\mathbf{x}_i) & \text{if } \mathbf{x} \in \Gamma_{cf}, \\ u(\mathbf{x}) & \text{otherwise,} \end{cases} \qquad \text{for every internal velocity component node } \mathbf{x}.$$

Here Γ_{cf} denotes the union of all octree cells faces, which are shared by cells of different sizes; $\mathbf{x}_i$ are four velocity nodes lying on the same large cells face as $\mathbf{x}$ (obviously $\mathbf{x} \in \{\mathbf{x}_1, \mathbf{x}_2, \mathbf{x}_3, \mathbf{x}_4\}$).

Next, we describe how the advection $\mathbf{u} \cdot \nabla \mathbf{u}$ and diffusion terms $\mathbf{div}\, \mu_\varepsilon D\mathbf{u}$ are treated in the interior of the computational domain. We consider a higher order upwind finite volume scheme on the graded octree meshes, which is both stable and accurate. In several places further in the text we need an approximation of the grid velocity function $\mathbf{a}$ in an arbitrary point of the computational domain.

In several places of this section we need an approximation of the grid velocity function $\mathbf{a}$ in an arbitrary point of the computational domain We interpolate the grid velocity function $\mathbf{a}(\mathbf{y})$, where $\mathbf{y} \in \Omega(t)$. Assume $\mathbf{y}$ belongs to a cell V and we start to interpolate the x-component of velocity to $\mathbf{y}$, i.e. $a_x(\mathbf{y})$. Consider a plane $\mathcal{P}$ such that $\mathbf{y} \in \mathcal{P}$ and $\mathcal{P}$ is orthogonal to the Ox axis. Let $\mathbf{x}_V \in \mathcal{P}$ be the orthogonal projection of the center of V on $\mathcal{P}$ and $\mathbf{x}_k$, $k = 1, \ldots, m$, $m \leq 12$, are the projections

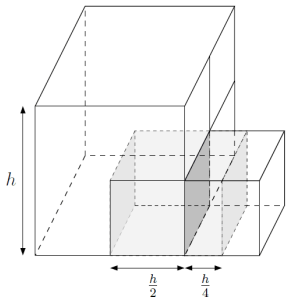

Figure 2.4: Reference points for the diffusion flux approximation

of centers of all cells sharing a face with V. The values $a_x(\mathbf{x}_V)$ and $a_x(\mathbf{x}_k)$ can be defined by a linear interpolation of the velocity values at nodes where a_x is collocated. Once $a_x(\mathbf{x}_V)$ and $a_x(\mathbf{x}_k)$, $k = 1, \ldots, m$, are computed, we consider the triangle fan based on $\mathbf{x}_V$ and $\mathbf{x}_k$, $k = 1, \ldots, m$, as shown in Figure 2.5. Now $a_x(\mathbf{y})$ is defined by a linear interpolation between the values of a_x in the vertices of the triangle, which contains $\mathbf{y}$. $\mathbf{a}_y(\mathbf{y})$ and $\mathbf{a}_z(\mathbf{y})$ are treated similarly.

For the incompressible fluid we treat the advection form $\mathbf{u} \cdot \nabla \mathbf{u} = \mathbf{div}\,(\mathbf{u} \otimes \mathbf{u})$, where the vector **div** operator applies row-wise. Equation (2.28) of the splitting method linearizes the nonlinear terms by using last time step's velocity information, so that we need to approximate $\mathbf{div}\,(\mathbf{u} \otimes \mathbf{a})$ for a known nodal velocity $\mathbf{a} = (a_x, a_y, a_z)^T$ and unknown nodal velocity $\mathbf{u} = (u, v, w)^T$. Below we discuss the FV discretization of $\mathbf{div}(u\mathbf{a})$. Other two components of $\mathbf{div}\,(\mathbf{u} \otimes \mathbf{a})$ are treated similarly.

Consider the velocity component u at the x-node $\mathbf{x}_F$, which is the barycenter of the face F. If F is shared by the cells of different sizes, we define the control volume V' as shown in Figure 2.4. If F is shared by the cells of the same size, then V' is defined in the obvious way by merging two half-cells. Let $\mathcal{F}(V')$ denote the set of all

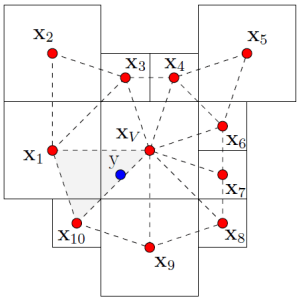

Figure 2.5: Reference points for the upwind approximation of advection. This illustration is for the derivative tangential to a face F, where the velocity degree of freedom is located.

faces for V'. We have

$$\mathbf{div}(u\mathbf{a})(\mathbf{x}_F) \approx |V'|^{-1} \sum_{F' \in \mathcal{F}(V')} |F'|(\mathbf{a}\cdot\mathbf{n})(\mathbf{x}_{F'})u(\mathbf{x}_{F'}), \tag{2.34}$$

where the term $\mathbf{a}(\mathbf{x}_{F'})\cdot\mathbf{n}u$ at the barycenters $\mathbf{x}_{F'}$ of faces $F' \in \mathcal{F}(V')$ is still need to be interpolated. Consider F' orthogonal to Oy so that $\mathbf{a}\cdot\mathbf{n} = a_y$. If two cells sharing F have the same size, then $(\mathbf{a}\cdot\mathbf{n})(\mathbf{x}_{F'})$ is the simple averaging of a_y values from the two neighboring face center nodes. Otherwise $a_y(\mathbf{x}_{F'})$ is computed by the interpolation procedure described above as in Fig 2.5. Now, consider the approximation of the advective flux at $F' \in \mathcal{F}(V')$ parallel to F, hence $\mathbf{a}\cdot\mathbf{n} = a_x$. After prescribing $a_x(\mathbf{x}_{F'})$ value with the help of the linear interpolation at the corresponding faces of the control volume, we define $u(\mathbf{x}_{F'})$ using (2.35). The only differences with the treatment of the face F' orthogonal to Oy are the following: a_x is defined in $\mathbf{x}$ (no interpolation required), and the reference points $\mathbf{x}_{-1}$, $\mathbf{x}_1$, $\mathbf{x}_2$ are always lying on cells x-faces (although not necessarily in the centers and one has to do the interpolation).

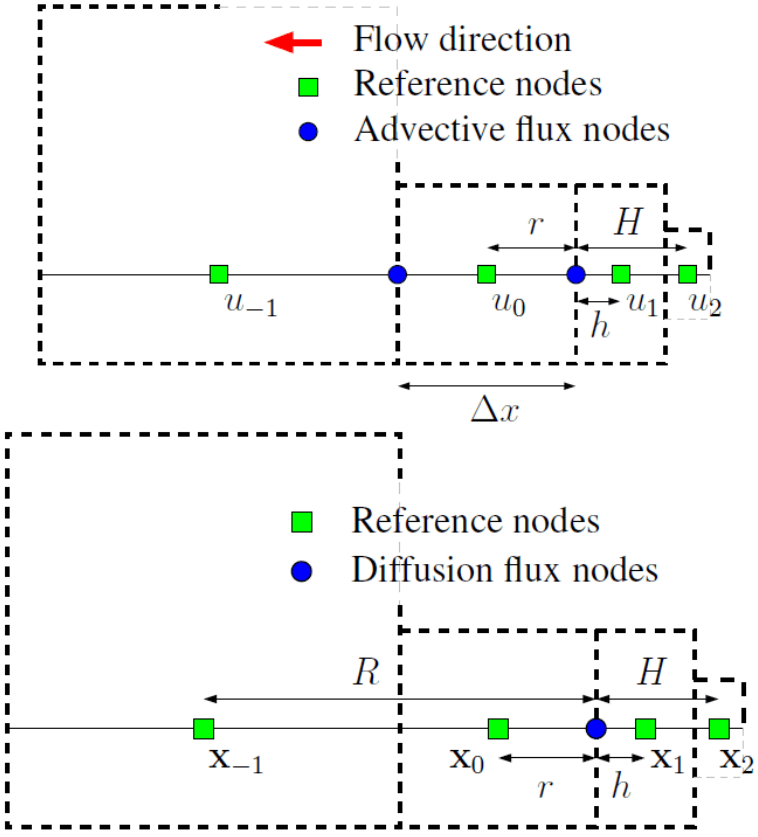

Figure 2.6: Reference points for the diffusion flux approximation

To define $u(\mathbf{x}_{F'})$, we take four 'reference' points ($\mathbf{x}_{-1}$, $\mathbf{x}_1$, $\mathbf{x}_2$, $\mathbf{x}_0 := \mathbf{x}_F$) as shown in Figure 2.6. Note that $\mathbf{x}_{-1}$, $\mathbf{x}_1$, and $\mathbf{x}_2$ are not necessarily grid nodes. Values u_{-1}, u_1, and u_2 in these nodes are then defined based on the following interpolation procedure. If the reference point belongs to a cell *smaller* than the cell of $\mathbf{x}_0$ (points $\mathbf{x}_1$ and $\mathbf{x}_2$ in the figure), then the linear interpolation between the *two* barycenters of adjunct faces is used. If the node belongs to a cell *larger* than the cell of $\mathbf{x}_0$ (point $\mathbf{x}_{-1}$ in the figure), then one apply the same interpolation procedure as we used above to define the values of $\mathbf{a}$. The only difference is that instead of the linear interpolation using the fan triangulation for $\mathbf{x}_V$ we use the weighted least-square method to fit the velocity values $u(\mathbf{x}_V)$ and $u(\mathbf{x}_k)$ by the second order polynomial Q_2, and further set $u(\mathbf{x}_{-1}) := Q_2(\mathbf{x}_{-1})$.

If $a_y(\mathbf{x}_F) > 0$, the u-values in reference points $\mathbf{x}_{-1}$, $\mathbf{x}_0$, $\mathbf{x}_1$ are used to approximate the flux. Otherwise, the u-values in the reference points $\mathbf{x}_0$, $\mathbf{x}_1$, $\mathbf{x}_2$ are needed. Assume $a_y(\mathbf{x}_F) < 0$, we set

$$u(\mathbf{x}_{F'}) = D^{-1}\left[u_0(hH^2 - h^2H) + u_1(rH^2 + r^2H) - u_2(hr^2 + h^2r) \right.$$
$$\left. +\lambda\Delta x^2(u_0(H-h) - u_1(H+r) + u_2(r+h))\right], \quad (2.35)$$

where $D = (r+h)(H-r)(H+r)$. A family of second order upwind discretization is parameterized by $\lambda \in \mathbb{R}$. $\lambda = 0$ produces the most accurate results on octree meshes and we use this value for numerical experiments.

Next, we explain how the discretization of diffusion terms $\mathbf{div}\,\mu_\varepsilon D\mathbf{u}$ is computed.

We use the following identity, which is valid for a smooth $\mathbf{u}$ such that $\mathbf{div}\,\mathbf{u} = 0$:

$$\mathbf{div}\,\mu_\varepsilon D\mathbf{u} = \frac{1}{2}(\mathbf{div}\,\mu_\varepsilon \nabla\mathbf{u} + (\nabla\mathbf{u})^T\nabla\mu_\varepsilon)$$

We can approximate $(\nabla\mathbf{u})^T\nabla\mu_\varepsilon$ according to (2.33), while the term $\mathbf{div}\,\mu_\varepsilon\nabla\mathbf{u}$ still need to be further discreted.

Consider a node $\mathbf{x}$ holding the velocity component u and lying on a face F and define a cubic control volume V' such that $\mathbf{x}$ is the center of V' and F is a middle cross section of V'. Note that the control volumes for x-nodes do not overlap, but for locally refined mesh they do not necessarily cover the whole bulk domain. Hence the dicretization of the diffusiion terms is a finite difference method, rather than a finite volume method. We have

$$(\mathbf{div}\,\mu_\varepsilon\nabla\mathbf{u})(\mathbf{x}) \approx |V'|^{-1} \sum_{F'\in\mathcal{F}(V')} |F'|(\mu_\varepsilon\nabla_h\mathbf{u}\cdot\mathbf{n})(\mathbf{y}_{F'}). \tag{2.36}$$

To approximate the diffusion flux at the center $\mathbf{y}_{F'}$ of $F' \in \mathcal{F}(V')$, we take four reference points ($\mathbf{x}_{-1}$, $\mathbf{x}_0$, $\mathbf{x}_1$, $\mathbf{x}_2$) as shown in Figure 2.6 (top). Velocity values u_{-1}, u_0, u_1, and u_2 are assigned to reference points same way as for the advective terms described above. Using the notation from Figure 2.6, the formal third order

approximation of the diffusion flux density $(\nabla u \cdot \mathbf{n})$ can be written out as

$$\begin{aligned}(\nabla u \cdot \mathbf{n}) \approx D^{-1}\big[&(h^2H^3 + h^3R^2 - H^3R^2 + h^2R^3 - H^2R^3 - h^3H^2)u_0 \\ &+ (H^3R^2 + r^3R^2 + H^2R^3 - r^2R^3 - H^3r^2 - H^2r^3)u_1 \\ &+ (h^3r^2 + h^2r^3 - h^3R^2 - r^3R^2 - h^2R^3 + r^2R^3)u_{-1} \\ &+ (h^3H^2 - h^2H^3 - h^3r^2 + H^3r^2 - h^2r^3 + H^2r^3)u_2\big],\end{aligned} \tag{2.37}$$

with $D = (H-h)(h+r)(H+r)(h+R)(H+R)(R-r)$. If the reference point in $\mathbf{x}_2$ is not available, we use the point $\mathbf{x}_{-2}$.

To enforce incompressibility condition, we approximate $\mathbf{div}\,\mathbf{u}$ in the center $\mathbf{x}_V$ of a grid cell V. We define the grid divergence operator by

$$(\mathbf{div}_h\,\mathbf{u}_h)(\mathbf{x}_V) = |V|^{-1} \sum_{F \in \mathcal{F}(V)} |F|(\mathbf{u}_h \cdot \mathbf{n})(\mathbf{x}_F). \tag{2.38}$$

Thanks to the staggered location of velocity nodes, the fluxes $(\mathbf{u}_h \cdot \mathbf{n})(\mathbf{x}_F)$ are well-defined.

CHAPTER 3

Small-amplitude Oscillations of Newtonian Droplet

3.1 Introduction

The small-amplitude oscillatory motion of drops and bubbles about the spherical shape is a classical problem in fluid mechanics considered in one form or another already by Kelvin (l890), Lamb (1932) and Rayleigh (1894). A number of other studies have also been devoted to this problem in recent times for its importance in chemical engineering, spray cooling, multi-phase flow and meteorology, as well as for its intrinsic scientific interest [51].

In this charpter, we first discuss the irrotational assumption for the small-amplitude oscillation of a Newtonian droplet. The analysis of periodicity and damping factor of the osclllating droplet are reviewed, and numerical experiments illustrated our analysis.

3.2 Irrotational Assumption

Lamb assumed an irrotational velocity field and used the dissipation method to evaluate the effect of the viscosity on the decay of the oscillations. An exact solution of this problem for the Newtonian case is found in the analysis by Miller and Scriven [38] of the oscillations of a fluid droplet immersed in another fluid. The viscous effects on the perturbed spherical flows were further studied in [51]. Those studies indicated that the no-slip condition on the interface between two fluids is a major source of vorticity production in the problem, while the irrotational velocity field is an adequate approximation in the *viscous* case, if the interface is free and one of two fluids is a gas of negligible density and viscosity. In the present study, the exterior is vacuum and we enforce no condition on tangential velocities. Hence for the analysis we accept the irrotational velocity field assumption. For the extended discussion of the plausibility of the vorticity-free approximation for the oscillating viscous droplet problem we refer to [33, 47].

Since the velocity field is assumed irrotational, we conclude it has a potential, a single-valued function ϕ. The components of velocity field, u, v, w, can be expressed

as follows:

$$(u, v, w) = (-\frac{\partial \phi}{\partial x}, -\frac{\partial \phi}{\partial y} - \frac{\partial \phi}{\partial z}), \tag{3.1}$$

where ϕ is called a 'velocity-potential'.

If a velocity potential exists, at any one instant, for any finite portion of an ideal fluid in motion under the action of potential forces, then, provided the density of the fluid be either constant or a function of the pressure only, a velocity-potential exists for the same portion of the fluid at all instants before or after.

3.3 Free Oscillations of a Droplet

3.3.1 Classic Case of Newtonian Droplet

The oscillating droplet problem often serves as a benchmark test for free surface and two-phase flow solvers for the Newtonian fluids.

Here we assume the motion of oscillating droplet is irrotational, i.e. $\nabla \times \mathbf{u} = 0$ Then the velocity field $\mathbf{u}$ has a potential ϕ s.t. $\mathbf{u} = -\nabla\phi$

Assuming the rotational symmetry [1], the initial shape of the droplet is given by a perturbation of the sphere

$$r = r_0(1 + \tilde{\varepsilon} \sum_{n \geq 1} c_n \mathcal{H}_n(\theta, \varphi)), \tag{3.2}$$

[1]The rotational symmetry is assumed for the presentation convenience. The arguments can be extended to more general perturbations.

where (r, θ, φ) are spherical coordinates, $\mathcal{H}_n$, $n = 1, 2, \ldots$, is the nth spherical harmonic and $\tilde{\varepsilon} > 0$ is small comparable to r_0. We denote by S_0 the unperturbed sphere of radius r_0 and without loss of generality assume that $\mathcal{H}_n$ are normalized, i.e. $\|\mathcal{H}_n\|_{L^2(S_0)} = 1$, and $\sum_{n\geq 1} c_n^2 = 1$. The fluid is assumed to be in rest at time $t = 0$ and $\mathbf{f} = \mathbf{0}$ for all $t \geq 0$. At $t = 0$ the mean curvature of the surface is not constant, and an unbalanced surface tension force causes droplet oscillation. Consider the evolution of the droplet surface given by

$$r = r_0 + \sum_{n\geq 1} A_n(t)\mathcal{H}_n(\theta, \varphi) =: r_0 + \sum_{n\geq 1} \xi_n. \tag{3.3}$$

In the absence of dissipation, Lamb showed that $A_n = r_0 c_n \tilde{\varepsilon} \sin(\sigma_n t + \alpha_n)$, where the period of oscillations depends on surface tension, fluid density, the harmonic's index n, and r_0.

3.3.2 Period and Damping Factor

For the Newtonian droplets, one may consider the evolution for the initial perturbation given by the *single* n-th harmonic:

$$r = r_0(1 + \tilde{\varepsilon}\mathcal{H}_n(\theta, \varphi)) \tag{3.4}$$

Figure 3.1 illustrates the motion of a Newtonian droplet over one period for the initial perturbation given by (3.4) with $n = 2$, $\tilde{\varepsilon} = 0.3$, $r_0 = 1$. For $t = 0.0046s$, the droplet is a purtubation sphere and the north tip of the dorplet has maxium

displacement; with time increasing, the displacement of north tip gradually decrease at $t = 0.3845s$; the droplet recovers to a sphere at $t = 0.7644s$; the displacement keeps decreasing till $t = 1.1443s$; then the droplet recovers to a sphere again at $t = 1.5242s$; with the displacement increase, finally, the droplet recover to the intial state at $t = 2.2840s$. Two statistics of the motion of droplet are of common interest: The droplet oscillation period T and the damping factor d. In this case and for $\tilde{\varepsilon} \ll 1$, a linear stability analysis from [35] predicts the period and the damping factor according to

$$T_{ref} = 2\pi\sqrt{\frac{\rho r_0^3}{n(n-1)(n+2)\gamma}}, \quad d_{ref} = \frac{2r_0^2}{(n-1)(2n+1)K}$$

Further in the text, we apply the method of viscous potentials and we recover the same period and damping factor as above, when the fluid is assumed Newtonian. Before we start our analysis, we illustrate numerically the irrotational velocity field assumption. We set surface tension coefficient $\gamma = 1$, density $\rho = 1$, harmonic order $n = 2$, the original ridus of droplet $r_0 = 1$ and $\tilde{\varepsilon} = 0.3$. Then we compare the skew-symmetric part of the velocity gradient tensor against its symmetric part for several computed solutions. For the skew-symmetric part we have

$$\int_{\Omega(t)} |\nabla_{scew}\mathbf{u}|^2 \mathrm{d}\mathbf{x} = \frac{1}{2}\int_{\Omega(t)} |\nabla \times \mathbf{u}|^2 \mathrm{d}\mathbf{x}.$$

Thus, Figure 3.2 shows the evolution of $\int_{\Omega(t)} |\mathbf{Du}|^2 \mathrm{d}\mathbf{x}$ and of the enstrophy for the Newtonian droplet and for two values of parameter $K = 10^{-2}$ and $K = 10^{-3}$. For

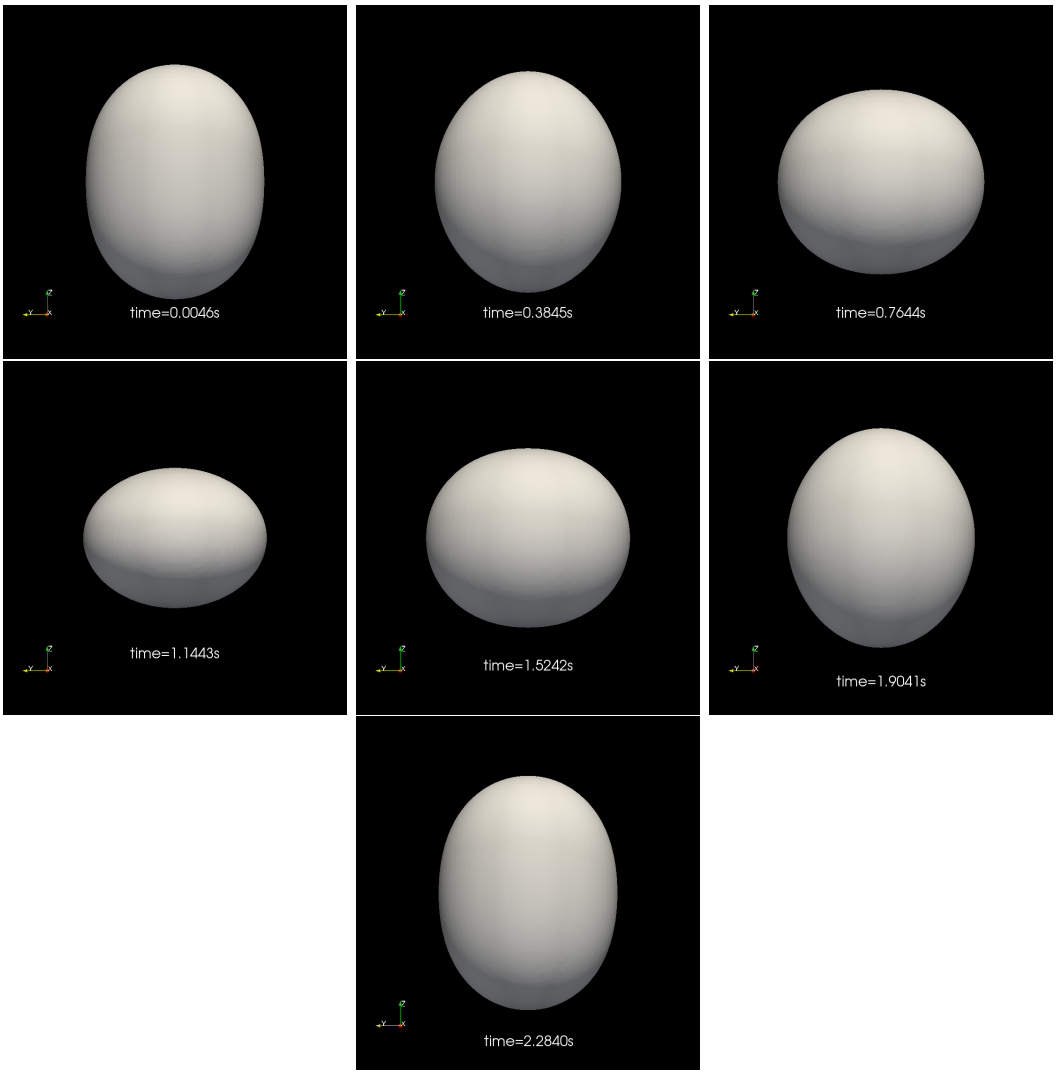

Figure 3.1: Oscillating droplet

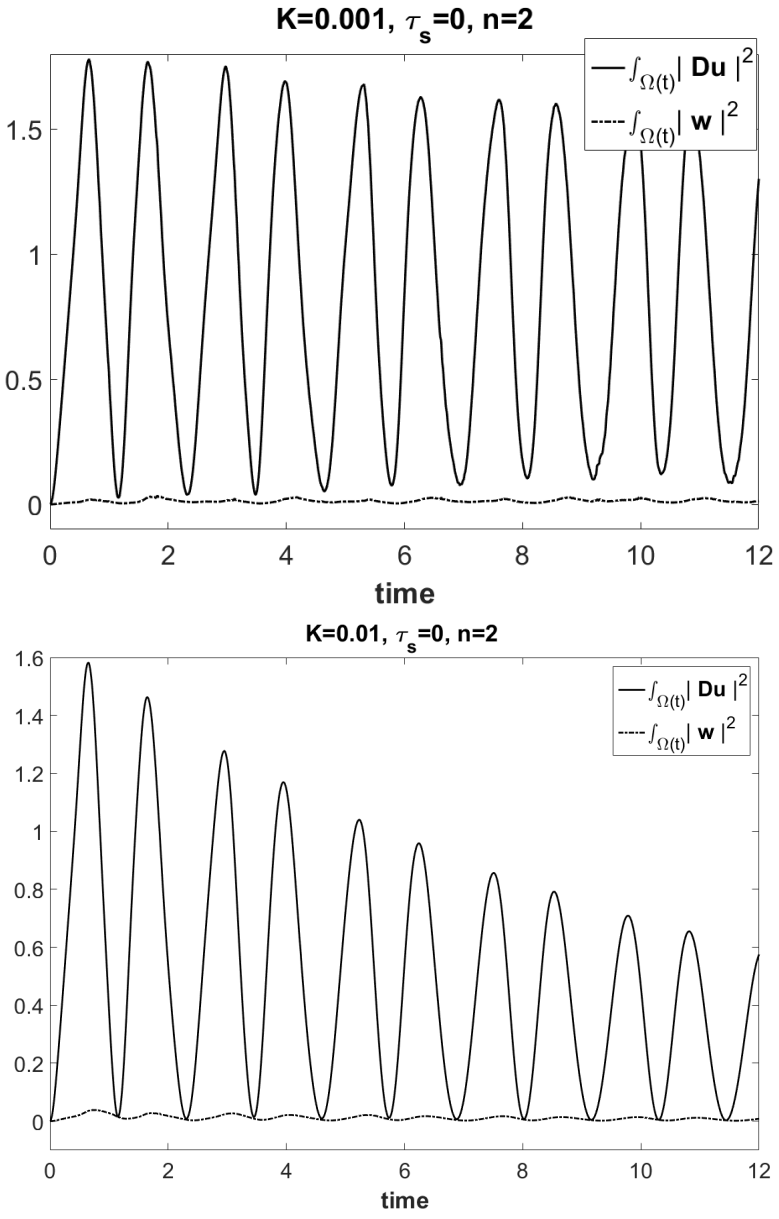

Figure 3.2: The evolution of $\int_{\Omega(t)} |\mathbf{Du}|^2 \mathrm{d}\mathbf{x}$ and of the enstrophy, $\int_{\Omega(t)} |\mathbf{w}|^2 \mathrm{d}\mathbf{x}$, with $\mathbf{w} = \frac{1}{\sqrt{2}} \nabla \times \mathbf{u}$. All results are computed for $n = 2$.

Newtonian droplet, the produced vorticity appears to be minor compared to symmetric rate of strain tensor.

We conclude that it is reasonable to assume the velocity field $\mathbf{u}$ has a potential ϕ, where $\nabla\phi = -\mathbf{u}$. Since the fluid is incompressible($\mathbf{div}\,\mathbf{u} = 0$), it holds $\mathbf{div}(\nabla\phi) = \Delta\phi = 0$. So ϕ is a harmonic function for all $t > 0$. We seek ϕ in the form of volume spherical harmonics series

$$\phi = \sum_{n\geq 1} B_n(t)\frac{r^n}{r_0^n}\mathcal{H}_n, \tag{3.5}$$

where $B_n(t)$ is a function that only depends on time t. Let $\xi := \sum_{n\geq 1}\xi_n$ in (3.3). The kinematic boundary condition (2.3) can be written as

$$\frac{\partial\phi}{\partial r} = \frac{\partial\xi}{\partial t} \quad \text{on} \quad S_0. \tag{3.6}$$

This gives

$$\frac{n}{r_0}B_n = \frac{dA_n}{dt}. \tag{3.7}$$

With the help of $\Delta\phi = 0$ and divergence theorem, the kinetic energy

$$E_{\text{kin}}(t) = \frac{\rho}{2}\int_{\Omega(t)} |\nabla\phi|^2 \mathrm{d}\mathbf{x} = \frac{\rho}{2}\int_{\Omega(t)} \mathbf{div}(\phi\nabla\phi) - \phi\Delta\phi \;\mathrm{d}\mathbf{x} = \frac{\rho}{2}\int_{\Gamma(t)} \phi\frac{\partial\phi}{\partial\mathbf{n}}\mathrm{d}\mathbf{s}. \tag{3.8}$$

By the definition of ϕ and dropping higher order terms one computes the kinetic energy:

$$E_{\text{kin}}(t) = \frac{\rho}{2}\int_{\Gamma(t)} \phi\frac{\partial\phi}{\partial\mathbf{n}}\mathrm{d}\mathbf{s} \simeq \frac{\rho}{2}\int_{S_0} \phi\frac{\partial\phi}{\partial r}\mathrm{d}\mathbf{s} = \frac{\rho}{2r_0}\sum_{n\geq 1} nB_n^2\int_{S_0}\mathcal{H}_n^2\mathrm{d}\mathbf{s}. \tag{3.9}$$

Recall that $\int_{S_0} \mathcal{H}_n \mathcal{H}_m \mathrm{d}\mathbf{s} = \delta_m^n$. Employing (3.7), we find the rate of change of E_{kin}:

$$\frac{d}{dt} E_{\text{kin}}(t) = \frac{\rho}{r_0} \sum_{n\geq 1} n \frac{dB_n}{dt} B_n = \rho \sum_{n\geq 1} \frac{r_0}{n} \frac{d^2 A_n}{dt^2} \frac{dA_n}{dt}. \tag{3.10}$$

For the potential energy, the rate of change of the potential energy is

$$\frac{d}{dt} E_{\text{free}}(t) = \gamma \int_{\Gamma(t)} \kappa(\mathbf{n}\cdot\mathbf{u}) \mathrm{d}\mathbf{s} \simeq \gamma \int_{S_0} \kappa \frac{\partial \phi}{\partial r} \mathrm{d}\mathbf{s}.$$

First we calculate

$$\begin{aligned}
\kappa = \frac{1}{R_1} + \frac{1}{R_2} &= \frac{2}{r_0} - \frac{2\xi}{r_0^2} - \frac{1}{r_0^2} \left\{ \frac{1}{\sin^2\theta} \frac{\partial^2 \xi}{\partial \phi^2} + \frac{1}{\sin\theta} \frac{\partial}{\partial \theta} \left(\sin\theta \frac{\partial \xi}{\partial \theta} \right) \right\} \\
&= \frac{2}{r_0} - \sum_{n\geq 1} \left\{ \frac{2A_n \mathcal{H}_n}{r_0^2} - \frac{n(n+1)}{r_0^2} A_n \mathcal{H}_n \right\} \\
&= \frac{2}{r_0} + \sum_{n\geq 1} \frac{A_n}{r_0^2} (n(n+1) - 2) \mathcal{H}_n.
\end{aligned}$$

where R_1, R_2 are the radii of principal curvatures of the surface.

Noting $\int_{S_0} \mathcal{H}_n = 0$ and $\int_{S_0} \mathcal{H}_n \mathcal{H}_m \mathrm{d}\mathbf{s} = \delta_m^n$, $n \geq 1$, thanks to (3.5), we have

$$\begin{aligned}
\gamma \int_{S_0} \kappa \frac{\partial \phi}{\partial r} \mathrm{d}\mathbf{s} &= \sum_{n\geq 1} \frac{2n}{r_0^2} B_n \int_{S_0} \mathcal{H}_n \mathrm{d}\mathbf{s} + \sum_{m,n\geq 1} \frac{\gamma(n-1)(n+2)n}{r_0^3} A_n B_m \int_{S_0} \mathcal{H}_n \mathcal{H}_m \mathrm{d}\mathbf{s} \\
&= \sum_{n\geq 1} \frac{\gamma(n-1)(n+2)n}{r_0^3} B_n A_n \int_{S_0} \mathcal{H}_n^2 \mathrm{d}\mathbf{s} \\
&= \sum_{n\geq 1} \frac{\gamma\,(n-1)(n+2)}{r_0^2} \frac{dA_n}{dt} A_n.
\end{aligned}$$

We have the variation of free surface potential energy

$$\frac{d}{dt}E_{\text{free}}(t) = \sum_{n\geq 1} \frac{\gamma\,(n-1)(n+2)}{r_0^2}\frac{dA_n}{dt}A_n.$$

This and (3.9) give the variation of the total energy

$$\frac{d}{dt}E_{\text{total}}(t) = \sum_{n\geq 1}\left\{\frac{r_0\rho}{n}\frac{d^2A_n}{dt^2}\frac{dA_n}{dt} + \frac{\gamma\,(n-1)(n+2)}{r_0^2}\frac{dA_n}{dt}A_n\right\}. \tag{3.11}$$

For the *ideal* fluid setting $\frac{d}{dt}E_{\text{total}}(t) = 0$, one finds $A_n = \widehat{A}_0\sin(\sigma_n t + \alpha_n)$ with the frequency

$$\sigma_n = \frac{\sqrt{\gamma\, n(n-1)(n+2)}}{r_0^{\frac{3}{2}}\rho^{\frac{1}{2}}} \tag{3.12}$$

as in [35].

Thanks to irrotational condition $\nabla\times\mathbf{u} = 0$, $\nabla\mathbf{u} = \mathbf{Du}$ is symmetric, we have

$$\int_{\Omega(t)}|\mathbf{Du}|^2\mathrm{d}\mathbf{x} = \int_{\Omega(t)}|\nabla\mathbf{u}|^2\mathrm{d}\mathbf{x} = \int_{\Gamma(t)}\mathbf{u}\cdot\frac{\partial\mathbf{u}}{\partial\mathbf{n}}\mathrm{d}\mathbf{s} = \frac{1}{2}\int_{\Gamma(t)}\frac{\partial|\mathbf{u}|^2}{\partial\mathbf{n}}\mathrm{d}\mathbf{s} \simeq \frac{1}{2}\int_{S_0}\frac{\partial|\nabla\phi|^2}{\partial r}\mathrm{d}\mathbf{s}.$$

Note that $\frac{\partial\phi_n}{\partial r} = \frac{n}{r}\phi_n$, with $\phi_n = B_n\frac{r^n}{r_0^n}\mathcal{H}_n$, since $\mathcal{H}_n$ is a spherical harmonic which does not depend on r.

With the help of these identities and the surface integration by parts formula

(2.14), we handle the integral on the righthand side as follows:

$$\begin{aligned}\int_{S_0} \frac{\partial|\nabla\phi|^2}{\partial r}\mathrm{d}\mathbf{s} &= \int_{S_0} \frac{\partial}{\partial r}\left(|\nabla_\Gamma\phi|^2 + \left|\frac{\partial\phi}{\partial r}\right|^2\right)\mathrm{d}\mathbf{s} \\ &= \int_{S_0} \frac{\partial}{\partial r}\left(-\phi\Delta_\Gamma\phi + \left|\frac{\partial\phi}{\partial r}\right|^2\right)\mathrm{d}\mathbf{s} \\ &= \sum_{n\geq 1}\int_{S_0} \frac{\partial}{\partial r}\left(n(n+1)r^{-2}\phi_n^2 + n^2 r^{-2}\phi_n^2\right)\mathrm{d}\mathbf{s}\end{aligned}$$

where Δ_Γ is Laplace-Beltrami operator s.t. $\Delta_\Gamma = \Delta - \frac{1}{r^2}\frac{\partial}{\partial r}(r^2\frac{\partial}{\partial r})$.

Substituting $\phi_n = B_n(r/r_0)^n\mathcal{H}_n$, we find

$$\begin{aligned}\int_{\Omega(t)} |\mathbf{Du}|^2\mathrm{d}\mathbf{x} &= \sum_{n\geq 1} n(n-1)(2n+1)r_0^{-3}[B_n]^2\int_{S_0}\mathcal{H}_n^2\mathrm{d}\mathbf{s} \\ &= \sum_{n\geq 1}\frac{(n-1)(2n+1)}{nr_0}\left|\frac{dA_n}{dt}\right|^2.\end{aligned} \tag{3.13}$$

Thus, for the *Newtonian* fluid, we get from (2.19), (4.4) and (4.25) that A_n satisfy the ODE:

$$\frac{d^2A_n}{dt^2} + \frac{K\,(n-1)(2n+1)}{r_0^2\rho}\frac{dA_n}{dt} + \frac{\gamma\, n(n-1)(n+2)}{r_0^3\rho}A_n = 0, \quad \text{for } \; n = 2,3,\ldots. \tag{3.14}$$

When the determinant of the characteristic equation for some $n > 1$ is non-negative (viscosity dominates over surface tension), then the corresponding harmonic does not contribute to oscillations and, using the initial condition $\frac{dA_n}{dt} = 0$ (since the

fluid is assumed at rest at initial time, i.e. $\phi = 0$), one finds

$$A_n(t) = A_n(0)\frac{\lambda_n^1 \exp(\lambda_n^2 t) - \lambda_n^2 \exp(\lambda_n^1 t)}{\lambda_n^1 - \lambda_n^2}, \tag{3.15}$$

where $\lambda_n^{1,2} < 0$ are corresponding real eigenvalues.

$$\lambda_n^{1,2} = -\frac{K\,(n-1)(2n+1)}{2r_0^2\rho} \pm \frac{1}{2}\sqrt{\left(\frac{K\,(n-1)(2n+1)}{r_0^2\rho}\right)^2 - \frac{4\gamma\, n(n-1)(n+2)}{r_0^3\rho}}$$

For complex eigenvalues, we observe oscillatory behavior. The amplitude of the oscillations for nth harmonic decays exponentially:

$$A_n(t) = \widehat{A}_n(0)\exp(-d_n\, t)\sin(\sigma_n t + \alpha_n), \quad \text{with} \;\; d_n = -Re(\lambda_n^1) = \frac{K\,(n-1)(2n+1)}{2r_0^2\rho}$$

and σ_n from (3.12), $\widehat{A}_n(0) = A_n(0)/\sin\alpha_n$. We note that for any fixed positive problem parameters r_0, ρ, γ, K, it holds

$$|A_n| \le A(0)\exp(-c_d n^2\, t), \tag{3.16}$$

with a constant c_d depending only on the parameters of the problem.

Table 3.1: Approximate number of total active degrees of freedom and the error in viscosity (numerical dissipation) introduced by the method for the ideal fluid.

h_{min}	$\frac{\ell}{16}$	$\frac{\ell}{32}$	$\frac{\ell}{64}$	$\frac{\ell}{128}$
$\approx$ # d.o.f.	111333	142405	452681	1772340
$\text{Error}_{\text{visc}}$	0.0032	9.5750e-04	7.2761e-04	4.8750e-04

To illustrate our analysis, we perform a series of experiments for the *Newtonian*

oscillating droplet[2]. The computational domain in this and all further experiments is the cube $(0, \ell)^3$, $\ell = \frac{10}{3}$; an initially perturbed sphere of radius $r_0 = 1$ is placed in the center of Ω. Everywhere in computations we set harmonic order $n = 2$, constant density parameter $\rho = 1$ and surface tension coffecient $\gamma = 1$.

This series of experiments assessed the accuracy of the numerical method and studied the convergence of flow statistics in this case to those given by the analysis in [35, 38] and recovered in (3.12) and (3.15). Thus, a droplet of the ideal fluid ($\nu = 0$, $\tau_s = 0$) oscillates infinitely with constant amplitude. We ran a series of experiments with $\nu = 0$ and different mesh size h. The results are shown in Figure 3.3. The deviation of the numerical solution from predicted behaviour allows us to estimate (by fitting an exponential function to maximum values of the kinetic energy over periods) the numerical dissipation of the method, which is reported in Table 3.1. We see that the numerical dissipation is low and decreases when the mesh is refined.

All following experiments in this charpter are done with $h_{\min} = \frac{\ell}{64}$. Tabel 3.2 shows the numerical viscosity and period for different viscosity parameters. In our numerical experiments, we recover the volume *vol* by summing the volume of each fluid cell in the computational domain, and compute the average raduis r_0 with $r_0 = \sqrt[3]{\frac{3}{4\pi} vol}$. The oscillation period is found by applying Fourier transform of the computed displacement of droplet's north tip.

Figure 3.4 shows the evolution of the kinetic energy and the kinetic energy peaks for several values of the viscosity parameter. For reference, we plot the exponent functions from (3.15) (there graphs are straight lines in the log scale). The slopes

[2]Numerical method was described in section 2.2

show the theoretically predicted *asymptotic* energy decay rates. Note that in the viscous case the rate (3.15) is valid for large enough time or sufficiently small perturbation $\tilde{\varepsilon}$, see [51], and so a deviation at the initial stage of oscillations may be expected.

K	r_0	T	δ	υ_{num}
0	1.0068	2.3023	278.6191	7.3e-04
500^{-1}	1.0068	2.2999	173.5589	0.0002
250^{-1}	1.0068	2.2932	108.7023	-0.0001
100^{-1}	1.0068	2.2847	47.3069	-0.0007
50^{-1}	1.0068	2.2773	23.8173	-0.0015
20^{-1}	1.0068	2.2658	9.3208	-0.0032
10^{-1}	1.0068	2.2581	4.5837	-0.0058

Table 3.2: The damping factor d was computed by the least square fitting of the function $c\ exp(-\frac{t}{d})$, the effective numerical viscosity of the scheme υ_{num} was assumed to hold $\upsilon_{num} = K - \frac{r_0^2}{5d}$, r_0 is the the radius of a spherical droplet with the same volume as the initial droplet. T is the period for oscillation.

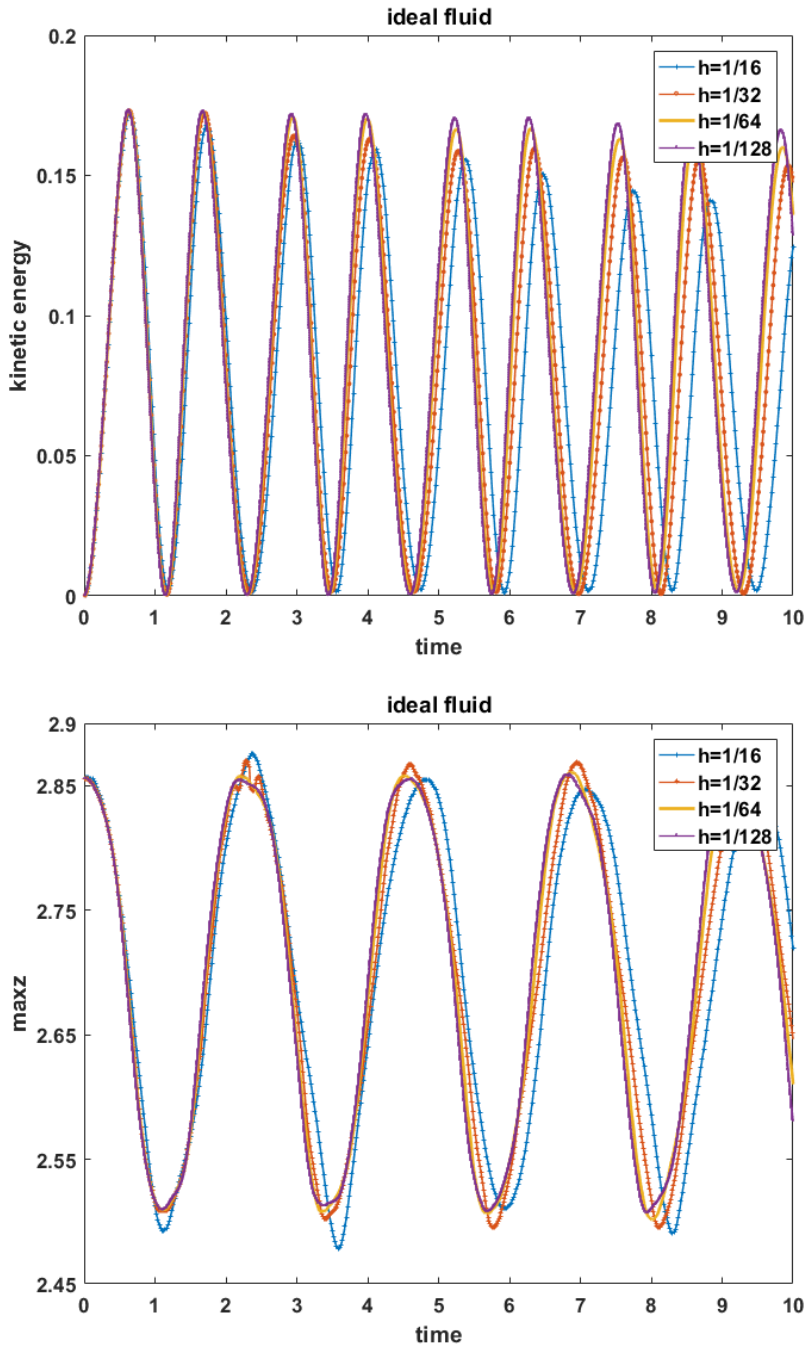

Figure 3.3: The evolution of the kinetic energy (upper plots) and the trajectory of the north tip (bottom plots) computed for different mesh size with $K = 0$.

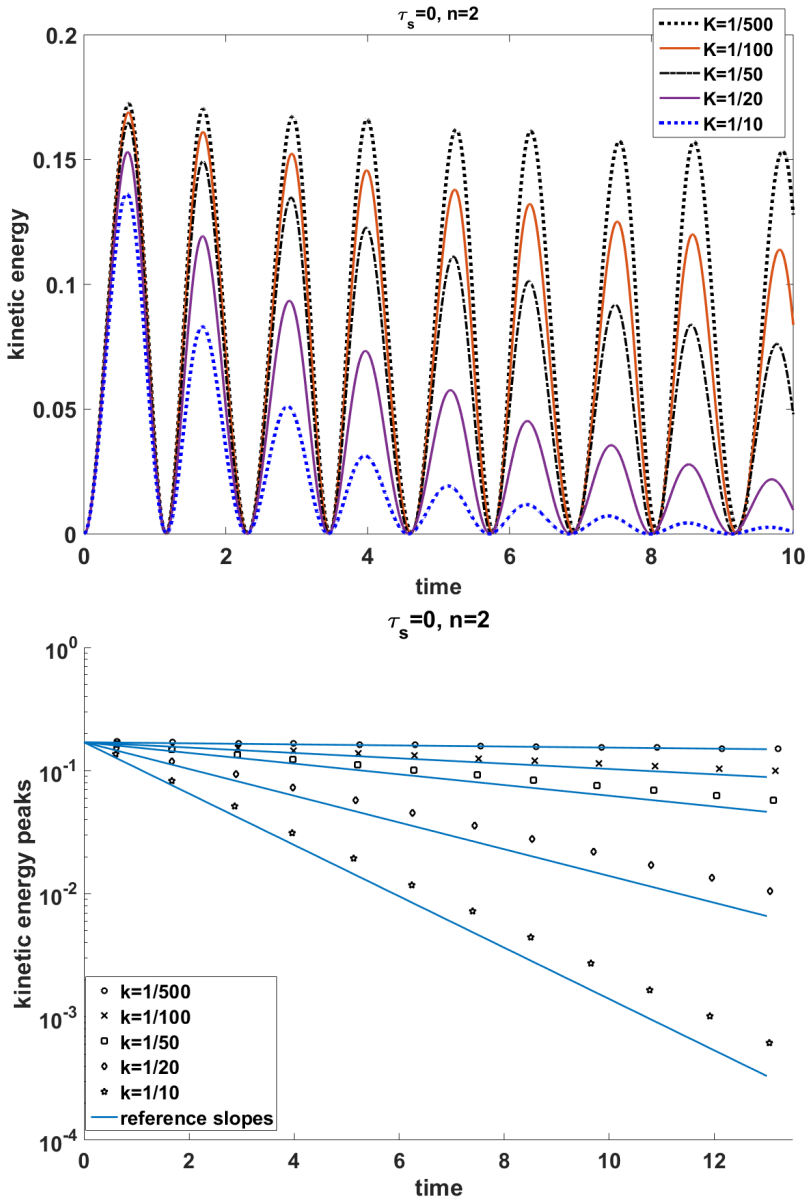

Figure 3.4: Evolution of $E_{\text{kin}}(t)$ and decay of the maximum (over a period) kinetic energy for the simulation of a Newtonian ($\tau_s = 0$, $\alpha = 1$) fluid droplet for several values of the viscosity parameter.

CHAPTER 4

Finite Stopping Time of Yield Stress Oscillating Droplet

4.1 Introduction

There are many materials in nature and industry exhibiting the viscoplastic behaviour. For example, these are fresh concrete, geomaterials, colloid solutions, powder mixtures, lubricants, metals under pressure treatment, blood in a capillary, foodstuffs, toothpaste. Such a medium below a certain stress value behaves as a rigid body and above this level behaves as an incompressible fluid. In many applications such as geophysical hazards (e.g., [3, 23]) or the damping of water waves by a muddy bottom [63], the complex dynamics of viscoplastic fluids is coupled to the evolution

a free surface. Recently there has been a significant increase of interest in developing and analyzing mathematical models and numerical methods for flows of yield stress fluids, flows with free surfaces and a combination thereof. However, 'yield stress fluids slowly yield to analysis' [10]. This section contributes to finding an answer to the following question: If there exists a finite stopping time T_f for a free-surface flow of an isolated volume of a yield stress fluid with surface tension forces? If the answer is positive, one is also interested in knowing an estimate of T_f.

The property of an unforced yield stress fluid flow to come to a complete rest in a finite time is an intrinsic one and often considered of keen importance[7]. For the yield-stress fluid flows in pipes of a constant cross-section this property of a weak solution to the variational formulation of the problem has been proved in [22, 30]. Theoretical upper bounds for the finite stopping times of several simple one-dimensional flows can be found in [31, 29, 41]. In the presence of a free surface, one may distinguish between the existence of a finite cessation time and the existence of a final arrested state (the latter can be attained in a finite or infinite time). Although, there is a common belief that the yield stress should bring an unforced free-surface flow to rest in a finite time, we are not aware of a mathematical analysis of this phenomenon except a few special flows. The question is intriguing since the theory for viscoplastic *films* with a free surface suggests infinite stopping times [37]. This may be an artifact of the thin-film approximation. The computational results in [43] suggest that the finite stopping times exist for isolated volumes with momentum and angular momentum free initial conditions.

The problem of yield stress fluid dynamics with free surface has been addressed

also numerically. Since the full problem poses a serious challenge for numerical simulations, it is common in the literature to consider simplified models of free-surface yield stress fluids. The shallow approximation is one of the most common reduced model for viscoplastic fluids flows over inclined planes and more complex 2D topographies, see [4, 6, 28] for recent reviews on this subject and [1, 9, 19, 32] for more recent advances. The previous studies of free surface viscoplastic fluid flows also include axisymmetric squeezing flows, bubble Bingham type flows [34, 2, 63], the free interface lattice Boltzmann model [21], and the dam-break problem [43].

However, contrary to the wall-bounded flows, the free energy (due to surface tension) enters the energy balance and makes the analysis harder. This and the lack of the embedding of $W^{1,1}(\Omega)$ in $L^2(\Omega)$ for $\Omega \in \mathbb{R}^3$ do not permit us to give the affirmative answer to the question raised above for a general free-surface viscoplastic fluid flow (see the next section). To gain more insight into the phenomenon, we consider the problem of motion for a viscoplastic drop for which the evolution is driven only by surface tension forces. Droplet flows of yield stress fluids, such as molten metals or polymers, arise in many engineering applications, including spray coating, 3D printing and arc welding [5, 27, 16]. In these and some other applications, surface tension forces play essential role in the formation and evolution of fluid droplets, see, e.g., [16, 53]. Thus, the oscillating viscoplastic droplet problem is also of its own interest as a model problem for such industrial flows.

Following the analysis of the Newtonian case [35, 52, 38, 51] in section 3.3, we assume that the initial shape of the drop is a *perturbation* of a sphere. For the *Newtonian* fluid, a linear stability analysis predicts that the drop oscillates, while

an amplitude of the oscillations decays exponentially to zero with a damping factor depending on the viscosity. To the best of our knowledge, this problem has never been analysed for a viscoplastic fluid. Under certain assumptions the analysis in this paper shows that in the presence of the yield stress the oscillations cease in a finite time T_f. In a series of numerical experiments we study the dependence of T_f on problem parameters: yield stress, flow index, and viscosity coefficient.

4.2 Finite Stopping Time for Yield Stress Droplet

4.2.1 Energy Inequality for Bingham Droplet

Since there is no explicit dissipation mechanism for the free surface energy $E_{\text{free}}(t)$ in (2.19), it is not easy to obtain directly from (2.19) a priori estimates for the solution which would be sufficient for showing the (local) well-posedness of the problem. Solonnikov in [56] was the first to study the solvability of the Newtonian fluid free-surface flow problem subject to surface tension forces. His proof does not directly rely on energy estimates, but rather on Fourier-Laplace transform techniques, which required the use of exponentially weighted anisotropic Sobolev–Slobodeskii spaces with fractional-order spatial derivatives. Further, energy methods to establish new space-time estimates for the Newtonian flows were developed in [17] and semigroup approach to establish the existence was used in [55]. None of these analyses are known to be extended to viscoplastic fluid flow problems with free surfaces and surface tension forces. If one is interested in the existence of the arrested state or

the finite stopping time, then the available analysis requires a lower bound for the plastic dissipation term

$$c_0\sqrt{\int_{\Omega(t)}\tau_s|\mathbf{u}|^2\mathrm{d}\mathbf{x}} \leq \int_{\Omega(t)}\tau_s|\mathbf{D}\mathbf{u}|\mathrm{d}\mathbf{x} \quad for \quad c_0>0.$$

The bound is feasible for certain one-dimensional flows and for the flow in a long pipe of a constant cross-section [22, 30]. However, in a more general case of $\Omega \in \mathbb{R}^d$, the estimate implies the embedding $W^{1,1}(\Omega) \hookrightarrow L^2(\Omega)$, which is known to be valid only for $d \leq 2$. We note that this fundamental difficulty arises within the existing framework regardless of the form of exterior forces and also for the fixed (time-independent) domain.

Following the assumption of Newtonian droplet in section 3.3.1, we assume that the velocity field is irrotational. We shall illustrate this assumption numerically. The velocity potential ϕ of irrotational flow of incompressible fluid is a harmonic function for all $t > 0$. We seek ϕ in the form of volume spherical harmonics series

$$\phi = \sum_{n\geq 1} B_n(t)\frac{r^n}{r_0^n}\mathcal{H}_n$$

Let $\xi := \sum_{n\geq 1}\xi_n$. The kinematic boundary condition (2.3) can be written as

$$\frac{\partial\phi}{\partial r} = \frac{\partial\xi}{\partial t} \quad \text{on} \quad S_0. \tag{4.1}$$

This gives

$$\frac{n}{r_0}B_n(t) = \frac{dA_n(t)}{dt}. \tag{4.2}$$

To illustrate $\nabla \times \mathbf{u} = 0$ assumption, we set surface tension coefficient $\gamma = 1$, density $\rho = 1$, harmonic order $n = 2$, the original ridus of droplet $r_0 = 1$ and $\tilde{\varepsilon} = 0.3$. We compare the skew-symmetric part of the velocity gradient tensor against its symmetric part for several computed solutions. For the skew-symmetric part we have $\int_{\Omega(t)} |\nabla_{scew}\mathbf{u}|^2 \mathrm{d}\mathbf{x} = \frac{1}{2}\int_{\Omega(t)} |\nabla \times \mathbf{u}|^2 \mathrm{d}\mathbf{x}$. Thus, Figure 4.1 shows the evolution of $\int_{\Omega(t)} |\mathbf{Du}|^2 \mathrm{d}\mathbf{x}$ and of the enstrophy for the Newtonian droplet and for the yield stress case with two values of parameter τ_s. For the yield stress fluid, we also plot $\int_{\Omega(t)} |\mathbf{Du}| \mathrm{d}\mathbf{x}$, since this statistic enters the energy balance. In all cases, the produced vorticity appears to be minor compared to symmetric rate of strain tensor.

By using the same analysis method as in section 3.3.2, with the help of $\Delta\phi = 0$ and dropping higher order with respect to $\tilde{\varepsilon}$ terms, we find the rate of change of E_{kin}:

$$\frac{d}{dt}E_{\text{kin}}(t) = \rho \sum_{n\geq 1} \frac{r_0}{n} \frac{d^2 A_n}{dt^2} \frac{dA_n}{dt}, \tag{4.3}$$

and the rate of change of the potential energy

$$\frac{d}{dt}E_{\text{free}}(t) = \sum_{n\geq 1} \frac{\gamma\,(n-1)(n+2)}{r_0^2} \frac{dA_n}{dt} A_n.$$

This and (4.3) gives the rate of change of the total energy

$$\frac{d}{dt}E_{\text{total}}(t) = \sum_{n\geq 1} \left\{ \frac{r_0\rho}{n} \frac{d^2 A_n}{dt^2} \frac{dA_n}{dt} + \frac{\gamma\,(n-1)(n+2)}{r_0^2} \frac{dA_n}{dt} A_n \right\}. \tag{4.4}$$

For the Bingham fluid, one should account for plastic dissipation besides viscous dissipation term. Thanks to $\nabla \times \mathbf{u} = 0$, the tensor $\nabla\mathbf{u}$ is symmetric. The viscous

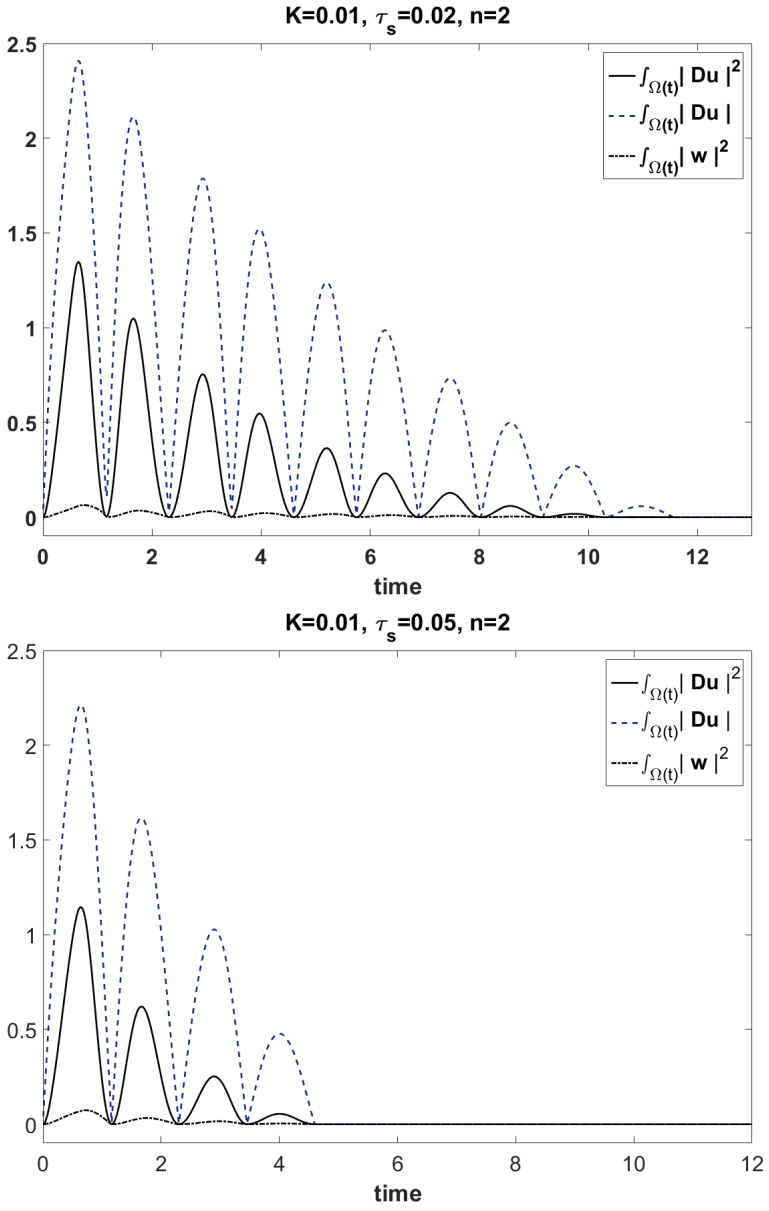

Figure 4.1: The evolution of $\int_{\Omega(t)} |\mathbf{Du}|^2 \mathrm{d}\mathbf{x}$ and of the enstrophy, $\int_{\Omega(t)} |\mathbf{w}|^2 \mathrm{d}\mathbf{x}$, with $\mathbf{w} = \frac{1}{\sqrt{2}} \nabla \times \mathbf{u}$. All results are computed for $n = 2$ and different values of τ_s. For $\tau_s > 0$ the figure also shows $\int_{\Omega(t)} |\mathbf{Du}| \mathrm{d}\mathbf{x}$.

dissipation term is exactly same as Newonian case:

$$\int_{\Omega(t)} |\mathbf{Du}|^2 \mathrm{d}\mathbf{x} = \sum_{n\geq 1} \frac{(n-1)(2n+1)}{nr_0} \left|\frac{dA_n}{dt}\right|^2. \tag{4.5}$$

Further we consider the effect of the plastic dissipation. To this end, we need the following trace inequality for functions of bounded variation in an N-dimensional ball [15]:

$$\begin{aligned} \|u - |\partial B|^{-1} \int_{\partial B} u \mathrm{d}\mathbf{s}\|_{L^1(\partial B)} \leq & \frac{N\sqrt{\pi}\,\Gamma(\frac{1}{2}(N+1))}{2\Gamma(\frac{1}{2}(N+2))} \|\nabla u\|_{L^1(B)} \\ \overset{N=3}{=} & \frac{N\sqrt{\pi}\,\Gamma(2))}{2\Gamma(\frac{5}{2})} \|\nabla u\|_{L^1(B)} = 2\|\nabla u\|_{L^1(B)}, \end{aligned} \tag{4.6}$$

where $\Gamma(\cdot)$ is Gamma function s.t. $\Gamma(\frac{1}{2}+n) = \frac{(2n-1)!!}{2^n}\sqrt{\pi}$, $\Gamma(n) = (n-1)!$.

Noting that for irrotational flow $\mathbf{Du} = \nabla\mathbf{u}$ and due to axial symmetries $\int_{S_0} u_i = 0$, $i = 1, 2, 3$, we apply the above inequality componentwise and we estimate the plastic dissipation to be *at least*

$$\begin{aligned} \tau_s \int_{\Omega(t)} |\mathbf{Du}| \mathrm{d}\mathbf{x} = \tau_s \int_{\Omega(t)} |\nabla\mathbf{u}| \mathrm{d}\mathbf{x} \simeq \tau_s \int_{\Omega_0} |\nabla\mathbf{u}| \mathrm{d}\mathbf{x} \geq \frac{\tau_s}{3} \int_{\Omega_0} |\nabla\mathbf{u}|_{\ell^1} \mathrm{d}\mathbf{x} \\ \geq \frac{\tau_s}{6} \int_{S_0} |\mathbf{u}|_{\ell^1} \mathrm{d}\mathbf{s} = \frac{\tau_s}{6} \int_{S_0} |\nabla\phi|_{\ell^1} \mathrm{d}\mathbf{s}, \end{aligned} \tag{4.7}$$

where $|\nabla\mathbf{u}|$ is the Frobenius norm of $\nabla\mathbf{u}$ s.t. $|\nabla\mathbf{u}| = \sqrt{\sum_{1\leq i,j\leq 3} (\frac{\partial u_i}{\partial x_j})^2}$ and

$$|\nabla\mathbf{u}|_{l_1} = \sum_{1\leq i,j\leq 3} |\frac{\partial u_i}{\partial x_j}|.$$

We note $3|\nabla \mathbf{u}| \geq |\nabla \mathbf{u}|_{l_1}$, since

$$\begin{aligned} |\nabla \mathbf{u}|_{l_1}^2 &= \sum_{1\leq i,j,m,n\leq 3} |\frac{\partial u_i}{\partial x_j}\frac{\partial u_m}{\partial x_n}| \\ &\leq \sum_{1\leq i,j,m,n\leq 3} \frac{1}{2}(|\frac{\partial u_i}{\partial x_j}|^2 + |\frac{\partial u_m}{\partial x_n}|^2) \\ &= 9\sum_{1\leq i,j\leq 3} (\frac{\partial u_i}{\partial x_j})^2 = 9|\nabla \mathbf{u}|^2 \end{aligned} \tag{4.8}$$

In vector calculus, $\nabla\phi$ can be decomposed into two parts: surface gradient $\nabla_\Gamma \phi$ and a component normal to the surface $\mathbf{n}\cdot(\nabla\phi\cdot\mathbf{n})$. Then we have from (4.7):

$$\begin{aligned} \tau_s \int_{\Omega(t)} |\mathbf{Du}| \mathrm{d}\mathbf{x} \geq \frac{\tau_s}{6}\int_{S_0} |\mathbf{u}|_{\ell^1} \mathrm{d}\mathbf{s} = \frac{\tau_s}{6}\int_{S_0} |\nabla\phi|_{\ell^1} \mathrm{d}\mathbf{s} \geq \frac{\tau_s}{6}\int_{S_0} |\nabla\phi|_{\ell^2} \mathrm{d}\mathbf{s} \\ = \frac{\tau_s}{6}\int_{S_0} \left(|\nabla_\Gamma \phi|^2 + \left|\frac{\partial\phi}{\partial r}\right|^2\right)^{\frac{1}{2}} \mathrm{d}\mathbf{s}. \end{aligned} \tag{4.9}$$

Let C_{emb} be optimal constant from the following Sobolev embedding inequality for the two-dimensional sphere S_0:

$$\|\phi\|_{L^2(S_0)} \leq C_{\mathrm{emb}} \|\phi\|_{W^{1,1}(S_0)} \quad \text{for } u \in W^{1,1}(S_0), \quad \text{s.t.} \int_{S_0} \phi \, ds = 0.$$

Applying this result, we proceed with the estimate on plastic dissipation from below

as follows,

$$\begin{aligned}\tau_s \int_{\Omega(t)} |\mathbf{Du}| \mathrm{d}\mathbf{x} &\geq \frac{\tau_s}{6} \int_{S_0} |\nabla_\Gamma \phi| \mathrm{d}\mathbf{s} \geq \frac{\tau_s}{6C_{\mathrm{emb}}} \left(\int_{S_0} |\phi|^2 \mathrm{d}\mathbf{s} \right)^{\frac{1}{2}} \\ &= \frac{\tau_s}{6C_{\mathrm{emb}}} \left(\int_{S_0} |\sum_{n\geq 1} B_n \mathcal{H}_n|^2 \mathrm{d}\mathbf{s} \right)^{\frac{1}{2}} = \frac{\tau_s}{6C_{\mathrm{emb}}} \left(\sum_{n\geq 1} B_n^2 \right)^{\frac{1}{2}} \\ &= \frac{\tau_s r_0}{6C_{\mathrm{emb}}} \left(\sum_{n\geq 1} n^{-2} \left| \frac{dA_n}{dt} \right|^2 \right)^{\frac{1}{2}}. \end{aligned} \tag{4.10}$$

Now we obtained lower bound for yield stress dissipation term.

4.2.2 Finite stopping time for Bingham drop

We first treat the case of the flow index $\alpha = 1$ (Bingham fluid). From (4.5) and (4.10) one gets the lower bound for the total internal energy dissipation (2.20) of the viscoplastic droplet

$$\begin{aligned} D(t) &= \int_{\Omega(t)} \left(K|\mathbf{Du}|^2 + \tau_s |\mathbf{Du}| \right) \mathrm{d}\mathbf{x} \\ &\geq \sum_{n\geq 1} \frac{K(n-1)(2n+1)}{nr_0} \left| \frac{dA_n}{dt} \right|^2 + \frac{\tau_s r_0}{6C_{\mathrm{emb}}} \left(\sum_{n\geq 1} n^{-2} \left| \frac{dA_n}{dt} \right|^2 \right)^{\frac{1}{2}}. \end{aligned} \tag{4.11}$$

Substituting this estimate to the total energy balance relation one obtains the following differential inequalities for A_n:

$$\sum_{n\geq 1}\left\{\frac{\rho}{2n}\frac{d}{dt}\left|\frac{dA_n}{dt}\right|^2+\frac{K\,(n-1)(2n+1)}{n\,r_0^2}\left|\frac{dA_n}{dt}\right|^2+\frac{\gamma\,(n-1)(n+2)}{2r_0^3}\frac{d|A_n|^2}{dt}\right\}$$
$$+\frac{\tau_s}{6\pi C_{\rm emb}}\left|\sum_{n\geq 1}n^{-2}\left|\frac{dA_n}{dt}\right|^2\right|^{\frac{1}{2}}\leq 0. \quad (4.12)$$

Based on (4.12) and the previous analysis, we show that there exists such finite T_f that $\frac{dA_n}{dt}=0$ for all $n\geq 1$ and $t>T_f$. However, we are not able to show the existence of the finite stopping time direclty from (4.12) due to its complexity. We need further estimate. To this end, we first estimates the third (surface tension) term with the help of the Cauchy inequality:

$$\sum_{n\geq 1}\frac{\gamma\,(n-1)(n+2)}{2r_0^3}\frac{d|A_n|^2}{dt}=\sum_{n\geq 1}\frac{\gamma\,(n-1)(n+2)}{r_0^3}\frac{dA_n}{dt}A_n$$
$$\leq\frac{\gamma}{r_0^3}\left(\sum_{n\geq 1}(n-1)^2(n+2)^2n^2A_n^2\right)^{\frac{1}{2}}\left(\sum_{n\geq 1}n^{-2}\left|\frac{dA_n}{dt}\right|^2\right)^{\frac{1}{2}}. \quad (4.13)$$

From the study of purely viscous case, when there is no additional plastic dissipation, we know that A_n decay at least exponentially with the decay factors not less than $-c_dn^2$, see (3.16). If we *assume* that adding the plastic dissipation can only contribute to the energy decay in a given harmonic, we conclude that there exists such finite time T_1 that

$$\frac{\gamma}{r_0^3}\left(\sum_{n\geq 1}(n-1)^2(n+2)^2n^2A_n^2\right)^{\frac{1}{2}}\leq\frac{\tau_s}{12C_{\rm emb}}\quad\text{for } t\geq T_1. \quad (4.14)$$

Using this and (4.13) in (4.12), we get

$$\sum_{n\geq 1}\left\{\frac{\rho n}{2}\frac{d}{dt}B_n^2+\frac{K\,(n-1)(2n+1)n}{r_0^2}B_n^2\right\}+\frac{\tau_s r_0}{12C_{\rm emb}}\left|\sum_{n\geq 1}B_n^2\right|^{\frac{1}{2}}\leq 0\quad\text{for } t\geq T_1. \tag{4.15}$$

For the sake of convenient notation we also make the substitution $\frac{dA_n}{dt}=\frac{n}{r_0}B_n$. Further we use the Hölder inequality

$$\sum_{k\geq 1}|x_k y_k|\leq(\sum_{k\geq 1}|x_k|^p)^{\frac{1}{p}}(\sum_{k\geq 1}|x_k|^q)^{\frac{1}{q}}$$

where p and q are in an open interval $(1,\infty)$ with $\frac{1}{p}+\frac{1}{q}=1$, to estimate the plastic dissipation term from below:

$$\sum_{n\geq 1}nB_n^2\leq\left(\sum_{n\geq 1}n^pB_n^{(2-\alpha)p}\right)^{\frac{1}{p}}\left(\sum_{n\geq 1}B_n^{\alpha q}\right)^{\frac{1}{q}}\overset{p=\frac{3}{2},\,q=3,\,\alpha=\frac{2}{3}}{=}\left(\sum_{n\geq 1}n^{\frac{3}{2}}B_n^2\right)^{\frac{2}{3}}\left(\sum_{n\geq 1}B_n^2\right)^{\frac{1}{3}}.$$

Thanks to the Young inequality $ab\leq\frac{\delta}{2}a^2+\frac{1}{2\delta}b^2,\ \forall\delta>0$, we have

$$\left(\sum_{n\geq 1}nB_n^2\right)^{\frac{3}{4}}\leq\left(\sum_{n\geq 1}n^{\frac{3}{2}}B_n^2\right)^{\frac{1}{2}}\left(\sum_{n\geq 1}B_n^2\right)^{\frac{1}{4}}\leq\frac{\delta}{2}\sum_{n\geq 1}n^{\frac{3}{2}}B_n^2+\frac{1}{2\delta}\left(\sum_{n\geq 1}B_n^2\right)^{\frac{1}{2}}\quad\forall\,\delta>0,$$

and after obvious rearrangement of terms, we get

$$2\delta\left(\sum_{n\geq 1}nB_n^2\right)^{\frac{3}{4}}-\delta^2\sum_{n\geq 1}n^{\frac{3}{2}}B_n^2\leq\left(\sum_{n\geq 1}B_n^2\right)^{\frac{1}{2}}\quad\forall\,\delta>0. \tag{4.16}$$

Thanks to the kinetic energy decay, we may always assume that T_1 is such that $E_{\rm kin}(t)\leq\frac{\rho}{2}$ for $t\geq T_1$ and $E_{kin}(t)=\frac{1}{2}\rho\sum_{n\geq 1}nB_n^2$. So $B_1^2\leq\frac{2}{\rho}E_{\rm kin}\leq 1$ for $t\geq T_1$.

Hence for $\delta \in (0,1]$ it holds $\delta^2 B_1^2 \leq \delta \left(\sum_{n\geq 1} n B_n^2\right)^{\frac{3}{4}}$. Now (4.16) yields

$$\delta \left(\sum_{n\geq 1} n B_n^2\right)^{\frac{3}{4}} - \delta^2 \sum_{n\geq 2} n^{\frac{3}{2}} B_n^2 \leq \left(\sum_{n\geq 1} B_n^2\right)^{\frac{1}{2}} \quad \forall\ \delta > 0. \tag{4.17}$$

If we substitute (4.17) in (4.15) with $\delta > 0$ satisfying

$$\frac{\tau_s r_0}{12 C_{\text{emb}}} \delta^2 \leq \frac{5K}{r_0^2 \sqrt{2}}, \tag{4.18}$$

we have

$$\begin{aligned} &\sum_{n\geq 1} \left\{ \frac{\rho n}{2} \frac{d}{dt} B_n^2 + \frac{K\,(n-1)(2n+1)n}{r_0^2} B_n^2 \right\} \\ &+ \frac{\tau_s r_0}{12 C_{\text{emb}}} [\delta \left(\sum_{n\geq 1} n B_n^2\right)^{\frac{3}{4}} - \delta^2 \sum_{n\geq 2} n^{\frac{3}{2}} B_n^2] \leq 0 \quad \text{for } t \geq T_1. \end{aligned} \tag{4.19}$$

Now $\frac{1}{2}$ of the viscous term $\frac{K\,(n-1)(2n+1)n}{2r_0^2} B_n^2$ kills the negative term $\frac{\tau_s r_0}{12 C_{\text{emb}}} \delta^2 \sum_{n\geq 2} n^{\frac{3}{2}} B_n^2$ on the left hand side of (4.19) due to equation (4.18). Further, for the viscous term in (4.15), the following holds trivially

$$\sum_{n\geq 1} \frac{K\,(n-1)(2n+1)n}{2r_0^2} B_n^2 \geq \frac{5K}{2r_0^2} \sum_{n\geq 2} n B_n^2. \tag{4.20}$$

Finally, we must get control of $\frac{5K}{2r_0^2} B_1^2$ with the help of the viscoplastic term. Again, thanks to the kinetic energy decay, we may assume that T_1 is sufficiently large such that for $t \geq T_1$ the coefficient B_1 is small to satisfy the inequality

$$\frac{5K}{2r_0^2} B_1^2 \leq \frac{\tau_s r_0 \delta}{24 C_{\text{emb}}} \left(\sum_{n\geq 1} n B_n^2\right)^{\frac{3}{4}}.$$

Thus, using (4.17), (4.20) in (4.15) and choosing δ satisfying (4.18), we arrive at the following differential inequality for the quantity $\widehat{B} := \sum_{n\geq 1} nB_n^2$:

$$\frac{\rho}{2}\frac{d\widehat{B}}{dt} + \frac{5K}{2r_0^2}\widehat{B} + \frac{\tau_s r_0 \delta}{24 C_{\text{emb}}}\widehat{B}^{\frac{3}{4}} \leq 0 \quad \text{for} \;\; t \geq T_1.$$

We can rearrange $y' + c_1 y + c_2 y^s = 0$ as

$$(y^{1-s} + \frac{c_2}{c_1})' + c_1(1-s)(y^{1-s} + \frac{c_2}{c_1}) = 0$$

The ODE is solved by $y^{1-s} = (y^{1-s}(0) + c_2 c_1^{-1})e^{-(1-s)c_1 t} - c_2 c_1^{-1}$ for $t \geq 0$, $s \neq 1$.

We need the Gronwall inequality : If u is differentiable in the interior $[a, \infty]$ and satisfies the differential inequality

$$u^{'} \leq \beta(t)u(t), \quad t \in (a, \infty),$$

then u is bouned by the solution of the corresponding differential equation $y'(t) = \beta(t)y(t)$:

$$u(t) \leq u(a) exp(\int_a^t \beta(s)ds), \quad \forall t \in (a, \infty)$$

Thanks to the Gronwall inequality we can find the bound

$$\widehat{B}^{\frac{1}{4}} \leq (\widehat{B}^{\frac{1}{4}}(T_1) + c_2 c_1^{-1})e^{-\frac{c_1(t-T_1)}{4}} - c_2 c_1^{-1}, \quad \text{for all } t \geq T_1,$$

with $c_1 = \frac{5K}{r_0^2 \rho}$, $c_2 = \frac{\tau_s r_0 \delta}{12 \rho C_{\text{emb}}}$, $s = \frac{1}{4}$ and $y = \widehat{B}$. From above inequality, we conclude that $\widehat{B} = 0$ for $t \geq T_f$, with a finite stopping time T_f.

Remark 4.1. The analysis above can be simplified for $d = 2$, i.e. for the problem of 2D oscillating drop. Indeed, in this case one can use the continuous embedding $W^{1,1}(\Omega) \hookrightarrow L^2(\Omega)$, $\Omega \subset \mathbb{R}^2$, and estimate the plastic dissipation terms from below as follows (compare to (4.9)-(4.10) and arguments below (4.15)):

$$\tau_s \int_{\Omega(t)} |\mathbf{Du}| \mathrm{d}\mathbf{x} = \tau_s \int_{\Omega(t)} |\nabla \mathbf{u}| \mathrm{d}\mathbf{x} \simeq \tau_s \int_{\Omega_0} |\nabla \mathbf{u}| \mathrm{d}\mathbf{x} \geq \widehat{C}_{\mathrm{emb}} \left(\int_{\Omega_0} |\mathbf{u}|^2 \mathrm{d}\mathbf{x} \right)^{\frac{1}{2}}$$
$$= \sqrt{2} \widehat{C}_{\mathrm{emb}} E_{\mathrm{kin}}^{\frac{1}{2}}(t) = \widehat{C}_{\mathrm{emb}} \left(\frac{\rho}{r_0} \sum_{n \geq 1} n B_n^2 \right)^{\frac{1}{2}}.$$

4.2.3 Shear Thickening Case

The fluid with the index $\alpha \geq 1$ fits the framework of the Bingham fluid if one notes the inequality

$$K|\mathbf{Du}|^{1+\alpha} + \tau_s |\mathbf{Du}| \geq \min\{K, \frac{\tau_s}{2}\} |\mathbf{Du}|^2 + \frac{\tau_s}{2} |\mathbf{Du}| \quad \text{for } \alpha \geq 1.$$

Therefore, the above analysis applies with the viscosity coefficient $\min\{K, \frac{\tau_s}{2}\}$ and yield stress $\frac{\tau_s}{2}$. However, the similar argument do not work for the shear thinning case $\alpha < 1$. Since our analysis relies on the viscosity term $K|\mathbf{Du}|^{1+\alpha}$, we cannot find a lower bound that is proportional to $|\mathbf{Du}|^2$.

4.3 Numerical Experiments

In this section we present the results of several numerical experiments, which illustrate the analysis of section 4.2. These experiments also study the dependence of the finite stopping time for the 3D droplet problem on various parameters. For the computer simulations we use the numerical approach developed in [43, 45, 44] for free-surface incompressible viscous flows and reviewed in section 2.2. The plasticity term is regularized by the Bercovier-Engelman method [8] ($|\mathbf{Du}|^{-1} \to (|\mathbf{Du}|^2 + \varepsilon^2)^{-\frac{1}{2}}$ in (2.5)) with the regularization parameter $\varepsilon = 10^{-6}$. We note that regularized problem may not inherit to existence of arrested state from the original problem. However, numerical experiments in Fig 4.2 demonstrate the convergent results of flow statistics for this level of values of ε. This indicates that the modelling error due to the regularization for $\varepsilon = 10^{-6}$ is minor compared to discretization errors. The regularization allows us to overcome computational difficulties associated with the non-differentiability of the constitutive relations and hence to perform 3D computations using dynamically refined grids towards the free surface, i.e. the refinement follows the evolution of the free surface. Such a refinement is of crucial importance for the sufficiently accurate computations of the surface tension forces. Only those cells of the background octree mesh are active in computations, which are intersected by the surface or belong to the interior of the droplet, so no auxiliary conditions are needed on the boundary of the bulk domain.

First we experiment with the Bingham fluid (fluid index $\alpha = 1$). As in the experiments with the Newtonian fluid, the initial perturbation is defined by (3.2)

with $A_2(0) = 1$ and $A_n(0) = 0$ for $n \neq 2$, $\tilde{\varepsilon} = 0.3$. Now Figures 4.3–4.6 show the evolution of the total kinetic energy and the trajectory of the north tip computed for viscosity coefficients $K = 0.01$ and $K = 0.025$ and different yield stress parameters τ_s, with $\tau_s = 0$ obviously showing the Newtonian case. Both from the kinetic energy evolution and the trajectory of the drop tip we clearly see the complete cessation of the motion in a finite time for all $\tau_s > 0$. It is interesting to note from the north tip trajectories that the final arrested state is not necessarily the original unperturbed sphere. The quasi-period of the oscillations looks independent of the K and τ_s values. The decay rate and the final stopping time, otherwise, depend on K and τ_s. The final stopping times presented in Table 4.2 were estimated from the computed kinetic energy applying the following formula:

$$T_f = \arg\min_{t>0} \max_{s\geq 0} \{E_{\text{kin}}(t+s) \leq 10^{-7}\}. \tag{4.21}$$

As can be expected T_f, in general, decreases for larger values of K and τ_s. It is interesting to note that for the range of modest, i.e., not too large, yield stress parameter values, the final stopping time demonstrates the dependence on τ_s close to $T_f = O(\tau_s^{-1})$. The viscosity coefficient for this problem appears to have less influence on the variation of the finite cessation time.

We next experiment with different initial perturbations of the drop. In this experiment, we set $A_4(0) = 1$ and $A_n(0) = 0$ for $n \neq 4$, $\tilde{\varepsilon} = 0.3$ in (3.2). For this setup, Figure 4.10 shows the evolution of the total kinetic energy and the trajectory of the north tip computed for viscosity coefficient $K = 0.01$ and different yield stress parameters τ_s. Again we observe the complete cessation of the motion in a finite time

for all $\tau_s > 0$. As expected from the analysis, the decay of the oscillations for the spherical harmonic with larger number happens faster and the computed stopping time T_f is smaller.

Further, we simulate the droplet oscillations for different values of the fluid index α. The computed evolution of the total kinetic energy and the trajectory of the north tip for $K = 0.01$ and $\tau_s = 0.02$ are shown in Figure 4.7. The estimated final stopping times are shown in Table 4.1. The results indicate that shear-thinning/thickening variation has some affect on the stopping times of the oscillations in general leading to faster decay as $\alpha \to 0$. At the same time, the results for $n = 4$ are inconclusive.

Table 4.1: Estimated final stopping times for various values of α and $n \in \{2, 4\}$ (for initial perturbation), with $K = 0.01$, $\tau_s = 0.02$.

α	n=2	n=4
0	7.96	5.55
0.5	9.09	5.53
1	10.27	5.46
2	11.40	4.92

We are also interested in the evolution of unyielded zones prior to the final cessation of the drop motion. Note that numerical studies of the pipe and enclosed flows typically demonstrate an earlier formation and further growth of the unyielded zones until they occupy the whole domain and halt the motion, see, e.g., [12, 13, 58]. However, for the oscillating drop problem, if we accept the approach of Lamb and seek the solution in the form of the series (3.3), then we conclude that the whole droplet comes to the full stop at T_f without *prior* formation of rigid zones. The solution in (3.3) is an approximation, and it is interesting to see which scenario the fluid motion follows in practice. Results of the numerical experiments suggest that

Lamb's approach is remarkably predictive. Figure 4.8 and 4.9 shows the unyielded regions computed with the help of von Mises criterion around the final stopping time for the Bingham fluid and with other parameters $K = 0.01$, $\tau \in \{0.04, 0.05\}$. The von Mises criterion defines the rigid zone as $\{\mathbf{x} : (K + \tau_s |D\mathbf{u}|_\varepsilon^{-1})|D\mathbf{u}| \leq \tau_s\}$.

The regions are visualized by three consecutive time steps. We see the (almost) immediate transition from fluidic to rigid phases in the entire droplet. Small unyielded regions near the droplet tips right before the complete stop can be a numerical phenomenon. We recall that the numerical method makes *no* use of the expansion in (3.3) or any other assumptions, including rotational symmetry, made in the framework of section 3.3; rather, it obtains the 3D solution of (2.2)–(2.5), (2.6) directly. Postprocessing of the numerical results for other values of τ_s showed very similar behavior of the rigid zones to those shown in Figure 4.8, so we skip including these plots. It also occurs that the von Mises criterion yields the final stopping times very close to those computed from (4.21).

4.4 Single Harmonic Bingham Droplet Analysis

It follows from the analysis in section 3.3, and was noticed already in [35], that for the Newtonian case the drop oscillations are the linear superposition of individual oscillations of each spherical harmonics, satisfying equations (3.14). For the non-Newtonian case, we do not see why a similar superposition principle should be valid in general. However, if for a prediction purpose one could *assume* that there is no transfer of energy between different scales, then one can write an ODE for the time

evolution of each harmonic separately. In addition to the terms in (3.14) one computes for the plastic dissipation: $\tau_s \int_{\Omega(t)} |\mathbf{Du}| \mathrm{d}\mathbf{x} \simeq \tau_s n^{-1} r_0^{1-n} \left|\frac{dA_n}{dt}\right| \int_{\Omega_0} |D^2(r^n \mathcal{H}_n)| \mathrm{d}\mathbf{x}$, where $D^2(f)$ is the Hessian matrix for f.

For example, if we consider $2nd$ harmonics, the initial shape is given by

$$r = r_0 + \widetilde{\varepsilon}\mathcal{H}_2(\theta, \phi),\ t = 0. \tag{4.22}$$

We set $\mathcal{H}_2 = \frac{1}{4}\sqrt{\frac{5}{\pi}}(3cos^2\theta - 1)$ and $\widetilde{\varepsilon} = 0.3$ in our case.

Since we assume no energy transfer between individual harmonics, the oscillations take the form:

$$r = r_0 + A_2(t)\mathcal{S}_2(\theta), \tag{4.23}$$

where $A_2(t)$ is the displacement of the north pole of sphere,

$$S_2 = \frac{1}{2}(3cos^2\theta - 1) = \frac{2z^2 - x^2 - y^2}{2r^2}.$$

Now we consider the velocity potential $\phi = B(t)\frac{r^2}{r_0^2}S_2$. The kinematic boudary condition gives

$$\frac{2}{r_0}B_2 = \frac{dA_2}{dt}. \tag{4.24}$$

The change rate of the total energy is

$$\frac{d}{dt}E_{\text{total}}(t) = \left\{\frac{r_0\rho}{2}\frac{d^2A_2}{dt^2}\frac{dA_2}{dt} + \frac{4\tau}{r_0^2}\frac{dA_2}{dt}A_2\right\} \iint S_2^2 ds,$$

The dissipation of viscosity term is

$$K\int_{\Omega(t)}|\mathbf{Du}|^2\mathrm{d}\mathbf{x}=K\frac{5}{2r_0}\left|\frac{dA_2}{dt}\right|^2\iint S_2^2ds. \tag{4.25}$$

where $\iint S_2^2ds=\int_0^{2\pi}\int_0^{\pi}\frac{1}{4}(3cos^2\theta-1)^2sin\theta d\theta d\phi=\frac{4\pi}{5}r_0^2$

Since we can complete $\nabla\mathbf{u}$ explicitly

$$\nabla\mathbf{u}=\nabla(\nabla\phi)=B_2(t)\frac{1}{r_0^2}\nabla(\nabla r^2S_2)=\frac{B_2(t)}{r_0^2}\begin{pmatrix}-1&0&0\\0&-1&0\\0&0&2\end{pmatrix},$$

we get

$$|\nabla\mathbf{u}|=|\sqrt{6}\frac{B_2(t)}{r_0^2}|.$$

The disspation of yield stress term for $2nd$ harmonic droplet should be

$$\tau_s\int_{S(0)}|\nabla\mathbf{u}|\mathrm{d}\mathbf{x}=\tau_sr_0\frac{4}{3}\pi\sqrt{6}B_2(t)=\tau_s\frac{2}{3}\pi\sqrt{6}|\frac{dA_2(t)}{dt}|$$

According to energy balance (2.20), we have the ODE,

$$\frac{d^2A_2}{dt^2}+\frac{5K}{r_0^2\rho}\frac{dA_2}{dt}+\frac{8\tau}{r_0^3\rho}A_2+\frac{\tau_s}{r_0\rho}\frac{10}{\sqrt{6}}sign\{\frac{dA_2}{dt}\}=0 \tag{4.26}$$

This ODE can be numerically solved with a high accuracy. The first time T_{pred} such that $A_n(t)=0$ for all $t>T_{\text{pred}}$ may serve as a prediction to the actual stopping time if the initial perturbation is defined only by the second harmonic (similar with

other harmonics). We solve (4.26) by the 4th order Runge-Kutta method. Then we compare the results with the one generated by the octree-CFD code in Figure 4.11 and 4.12 and report the computed T_{pred} in Table 4.2. The results obtained from computing equation (4.26) are rather close to the numerical results obtaining from system equations in section 2.1.2. The computed T_{pred} are close to T_f recovered by the full 3D simulations. This suggests that the transfer of energy between the scales (from lower to higher) does not play an essential role in this problem and gives an additional support to the assumption leading to (4.14). The "—" sign in Table 4.2 indicates that for $\tau_s = 0.4$, the droplet motion is halted at $t = 0$.

Table 4.2: Computed and 'predicted' final stopping times for various values of K and τ_s, with $\alpha = 1$, $n = 2$ (for initial perturbation).

τ_s	K=0.005		K=0.01		K=0.025	
	T_f	T_{pred}	T_f	T_{pred}	T_f	T_{pred}
0.02	10.29	9.940	10.27	8.873	9.182	7.760
0.03	8.274	6.647	6.847	6.629	7.125	5.543
0.04	5.712	4.439	5.722	4.434	4.568	4.434
0.05	4.573	4.416	4.577	4.361	4.688	3.326
0.1	2.279	2.213	2.279	2.213	2.289	2.213
0.2	1.135	1.099	1.130	1.099	1.130	1.099
0.4	1.260	–	1.265	–	1.237	–

We demonstrate below that for an isolated motion in the second harmonic there exists the halting yield stress coefficient τ_s.

Without lost generaility, we assume $A_2(0) > 0$. The energy balance equation (2.19) also has the form

$$\frac{dE_{\text{free}}(t)}{dt} + \frac{dE_{\text{kin}}(t)}{dt} + D(t) = 0$$

If the droplet starts to oscillate, then the kinetic energy of droplet should increase and $\frac{dA_2(t)}{dt} < 0$, when t is close enough to 0, since $A_2(t) > 0$.

The onset of droplet oscillations also means that the variation of kinetic energy is positive, i.e. $\frac{dE_{kin}(t)}{dt} > 0$, since $E_{kin}(0) = 0$. Since the variation of kinetic energy is positive, from the energy balance, for small enough $t > 0$, we have

$$\frac{dE_{\text{free}}(t)}{dt} + D(t) < 0 \tag{4.27}$$

By plugging the $2nd$ harmonic into equation (3.3.2), the variation of free surface energy is

$$\frac{d}{dt}E_{\text{free}}(t) = \left\{\frac{4\tau}{r_0^2}\frac{dA_2}{dt}A_2\right\}\iint S_2^2 ds. \tag{4.28}$$

and the plastic dissipation term

$$D(t) \geq \tau_s \int_{S(0)} |\nabla \mathbf{u}| \mathrm{d}\mathbf{x} = \tau_s r_0 \frac{4}{3}\pi\sqrt{6}|B_2(t)| = \tau_s \frac{2}{3}\pi\sqrt{6}|\frac{dA_2(t)}{dt}| \tag{4.29}$$

Subsituting the variation of free surface (4.28) and dissipation (4.29) into (4.27), we get

$$\frac{16}{5}\pi\frac{dA_2(t)}{dt}A_2 + \tau_s\frac{2\sqrt{6}\pi}{3}|\frac{dA_2(t)}{dt}| < 0$$

Since $\frac{dA_2(t)}{dt} < 0$, we have $\frac{4\sqrt{6}}{5}A_2(t) \geq \tau_s$, for t enough close to 0. In other words, $\frac{4\sqrt{6}}{5}A_2(0) \geq \tau_s$ is a necessary condition for the droplet start to oscillate.

Note for $A_2(0) = 0.1892$ (the initial displacement of the north pole of sphere), $\tau_s = 0.3708$ is the threshold yield stress parameter of droplet to begin oscillate.

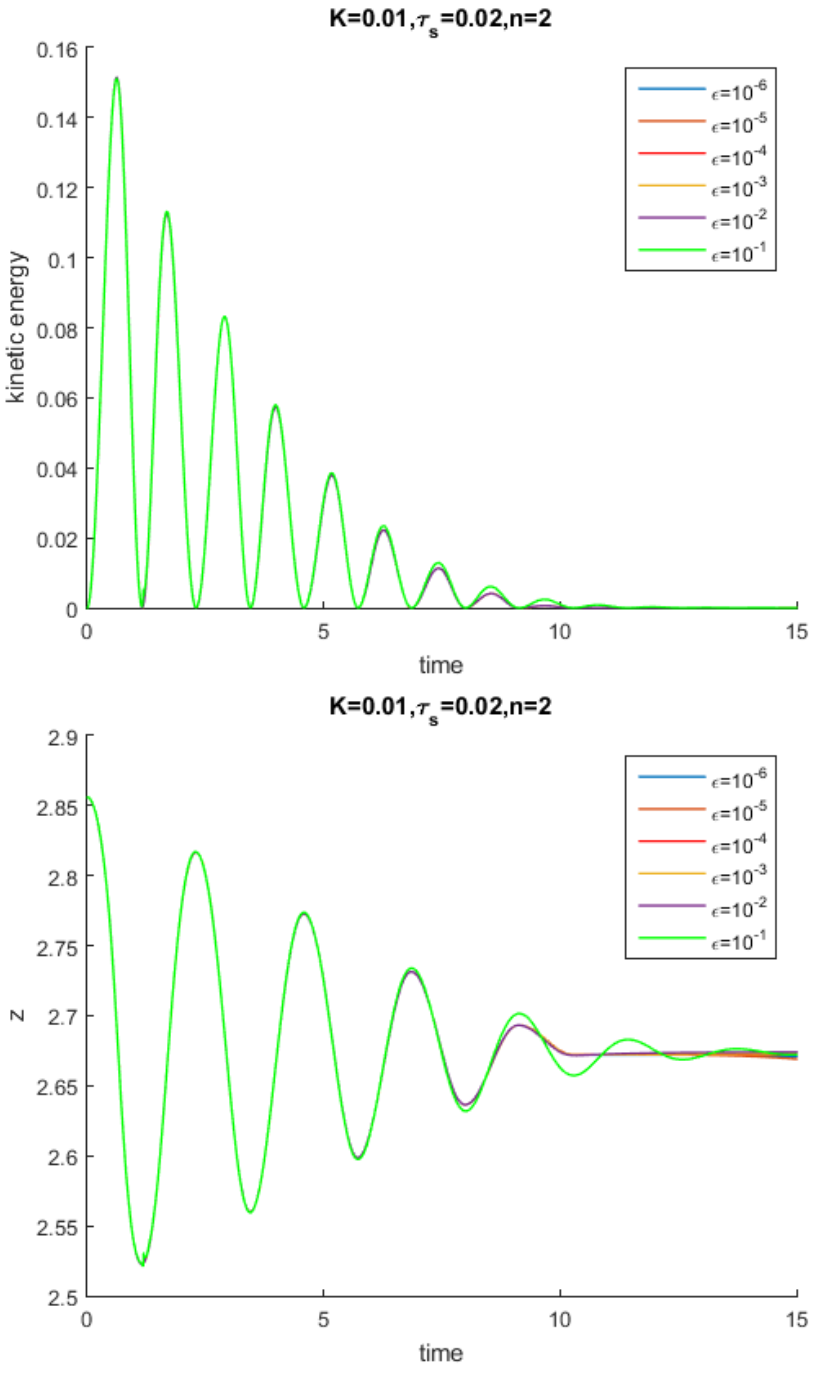

Figure 4.2: The evolution of the kinetic energy (upper plots) and the trajectory of the north tip (bottom plots) computed for $K = 0.01, \tau_s = 0.02$, different regularization parameter ε and the second spherical harmonic ($n = 2$) to define initial perturbation.

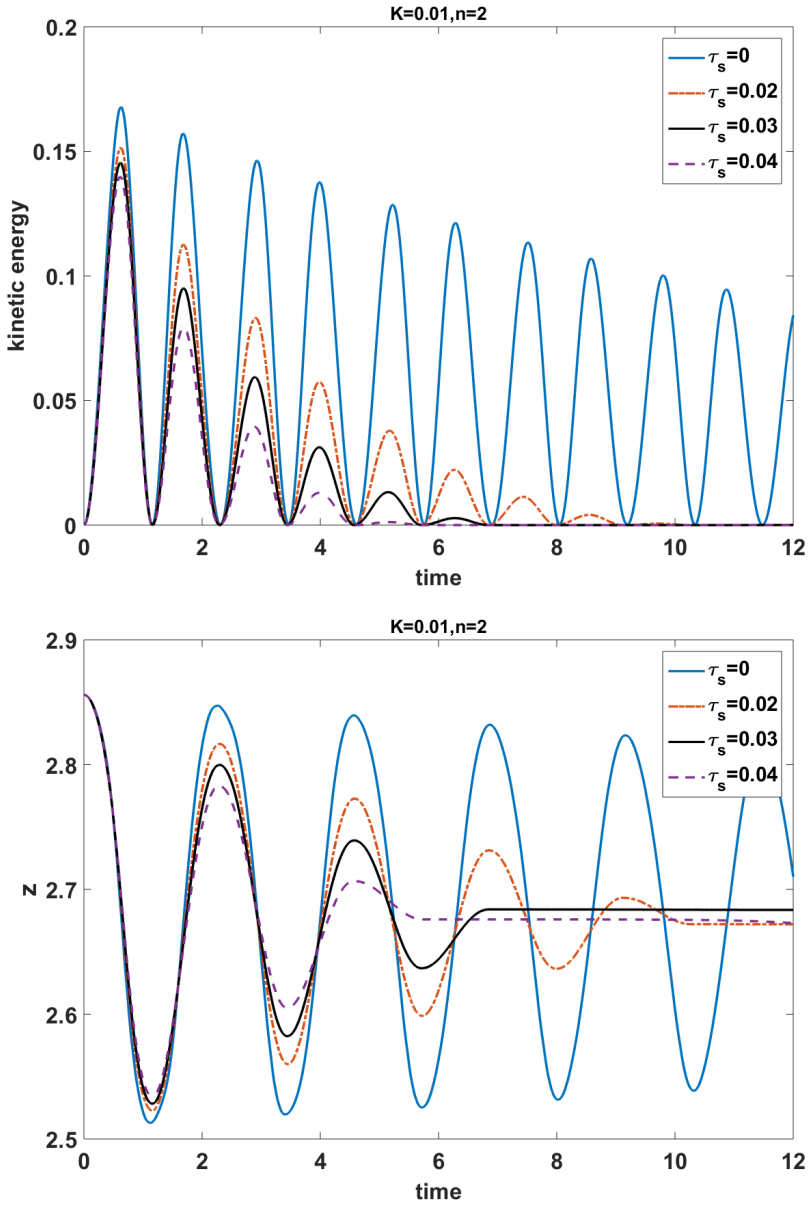

Figure 4.3: The evolution of the kinetic energy (upper plots) and the trajectory of the north tip (bottom plots) computed for $K = 0.01$, different τ_s and the second spherical harmonic ($n = 2$) to define initial perturbation.

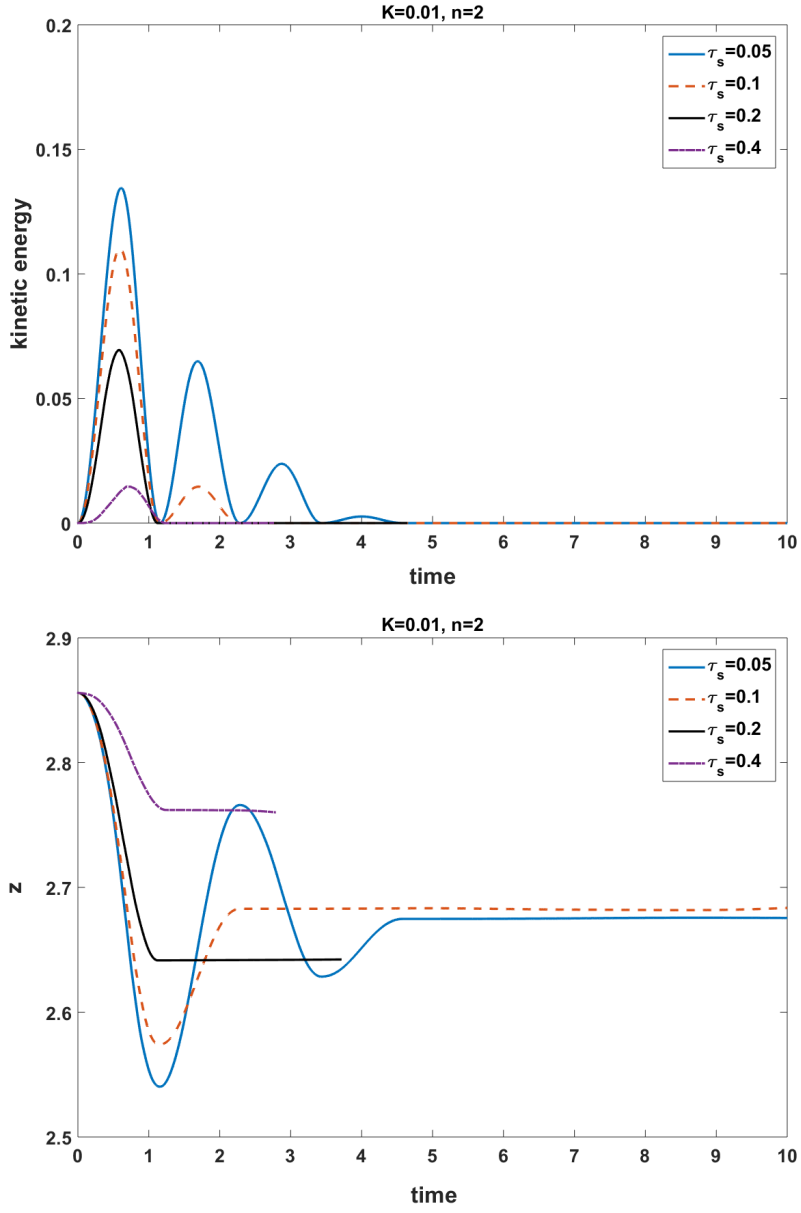

Figure 4.4: The evolution of the kinetic energy (upper plots) and the trajectory of the north tip (bottom plots) computed for $K = 0.01$, different τ_s and the second spherical harmonic ($n = 2$) to define initial perturbation.

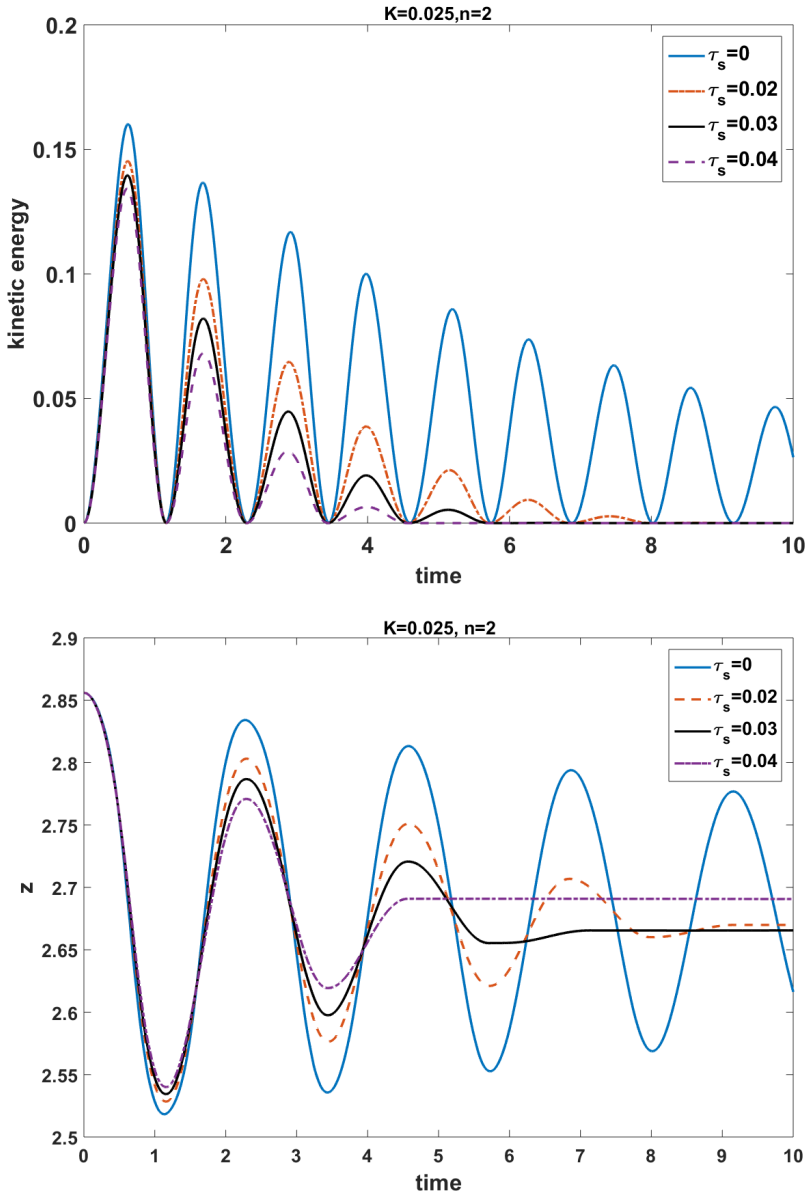

Figure 4.5: The evolution of the kinetic energy (upper plots) and the trajectory of the north tip (bottom plots) computed for $K = 0.025$, different τ_s and the second spherical harmonic ($n = 2$) to define initial perturbation.

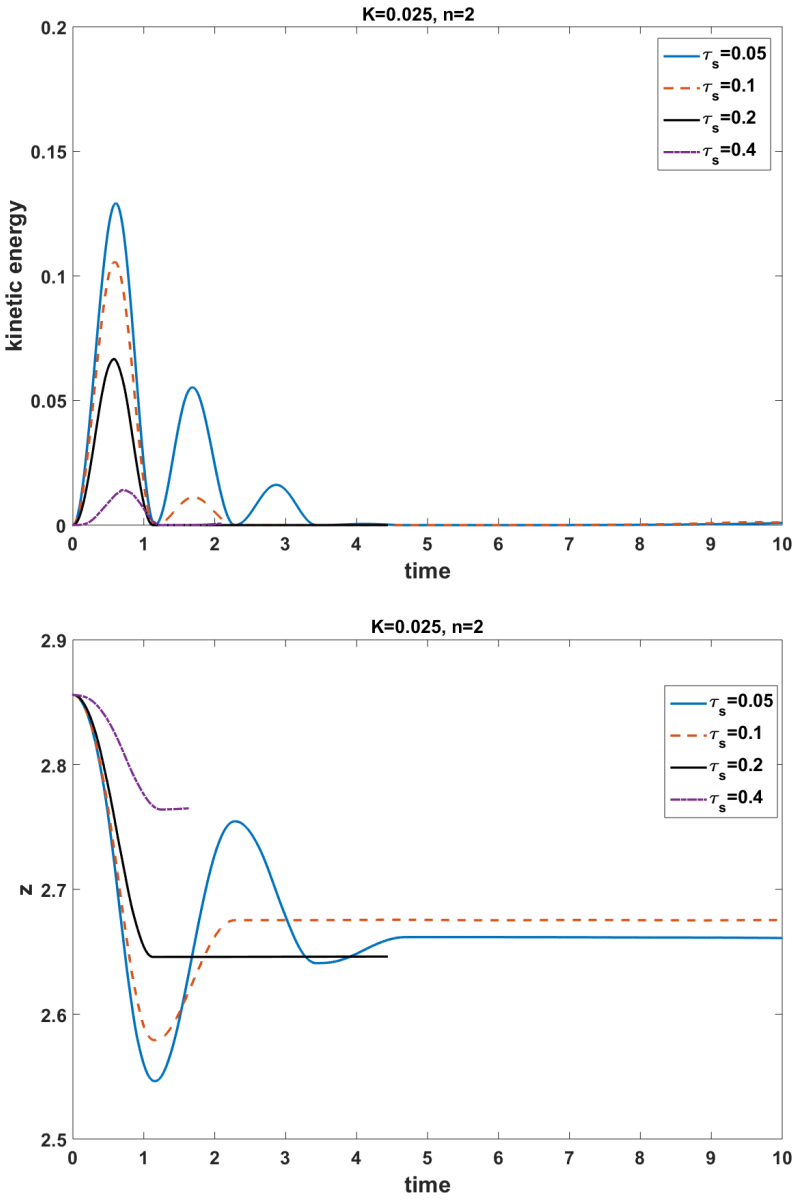

Figure 4.6: The evolution of the kinetic energy (upper plots) and the trajectory of the north tip (bottom plots) computed for $K = 0.025$, different τ_s and the second spherical harmonic ($n = 2$) to define initial perturbation.

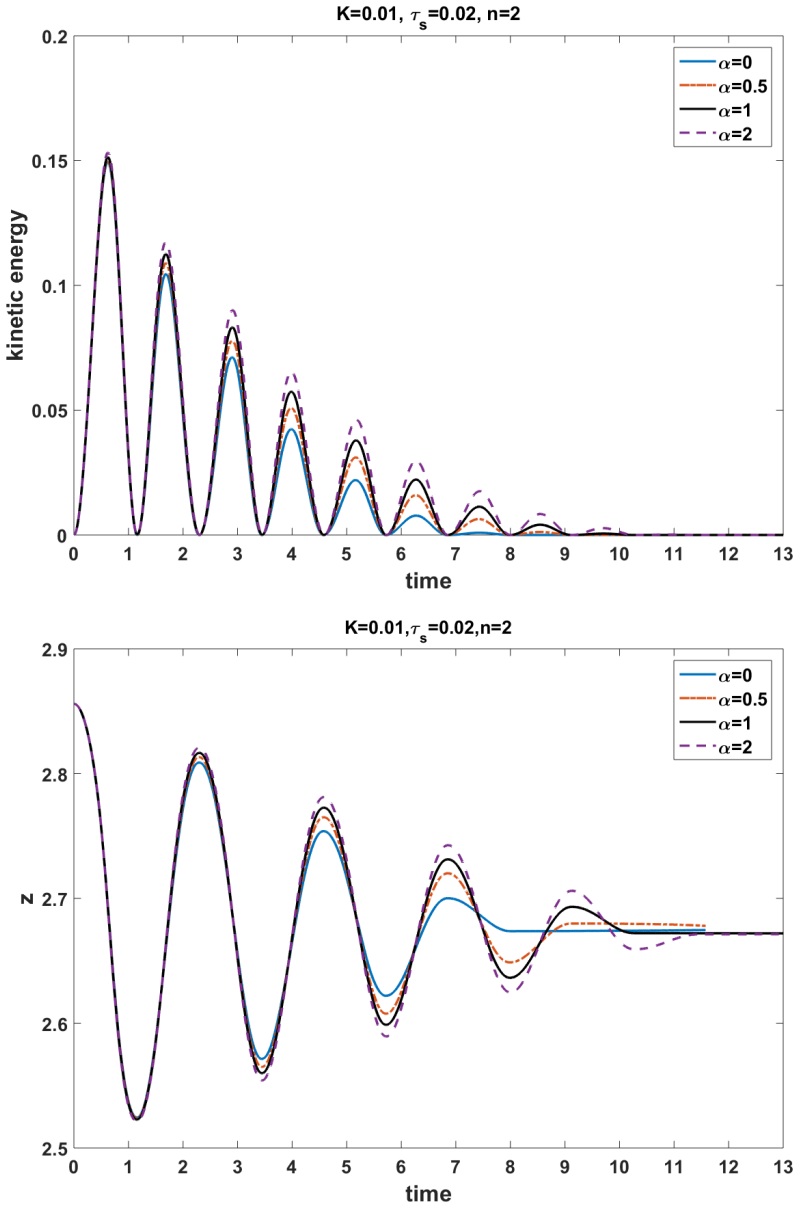

Figure 4.7: The evolution of the kinetic energy and the trajectory of the north tip computed for $K = 0.01$, $\tau_s = 0.02$, and different flow indexes α.

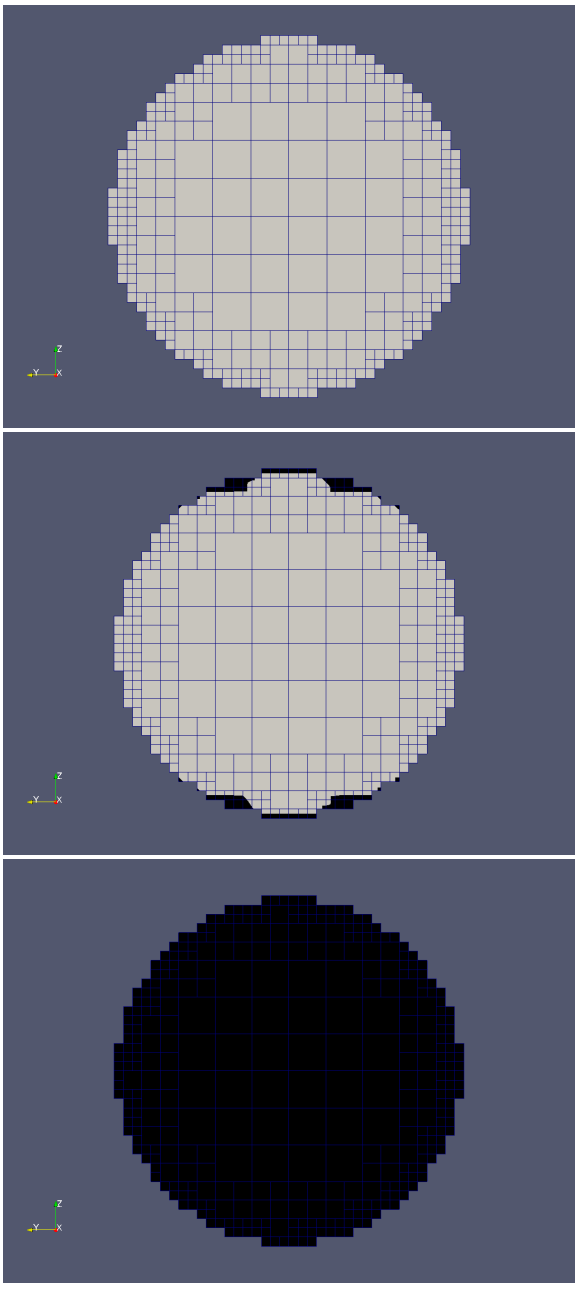

Figure 4.8: The visualization of the rigid zones near the final stopping time for $\tau_s = 0.04$, with other parameters $K = 0.01$, $\alpha = 1$, $n = 2$. The cutaway by the xz-midplane is shown. The unyielded regions by von Mises criterion are colored black. Full cells are shown, but cut cells ensuring $O(h^2)$ boundary approximation are used in computations.

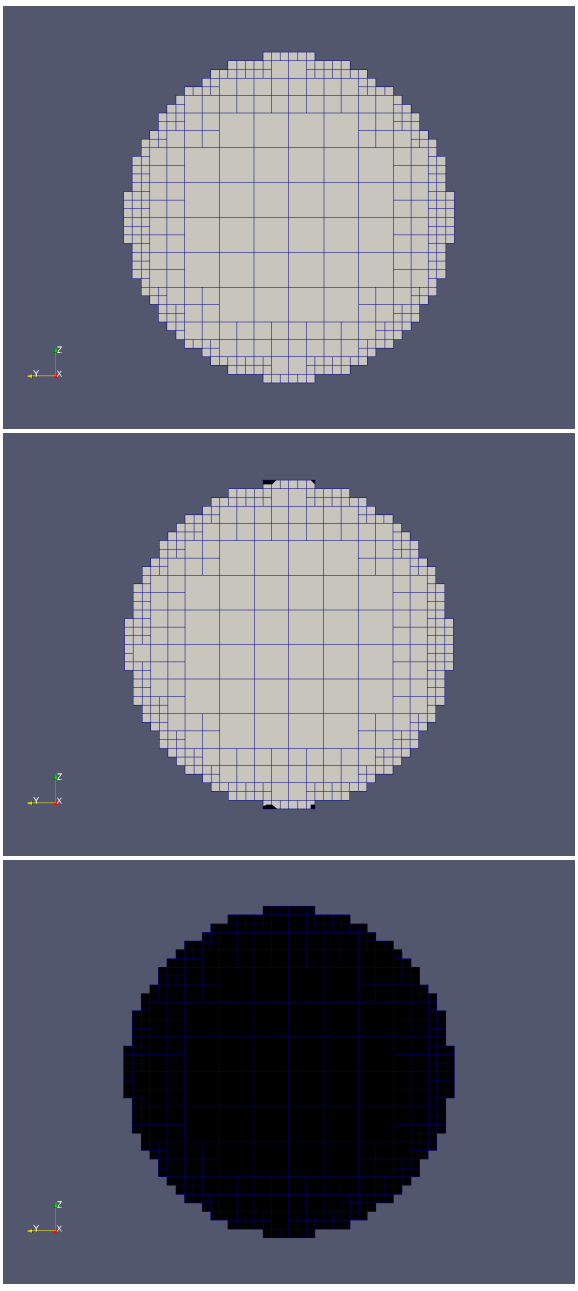

Figure 4.9: The visualization of the rigid zones near the final stopping time for $\tau_s = 0.05$, with other parameters $K = 0.01$, $\alpha = 1$, $n = 2$. The cutaway by the xz-midplane is shown. The unyielded regions by von Mises criterion are colored black. Full cells are shown, but cut cells ensuring $O(h^2)$ boundary approximation are used in computations.

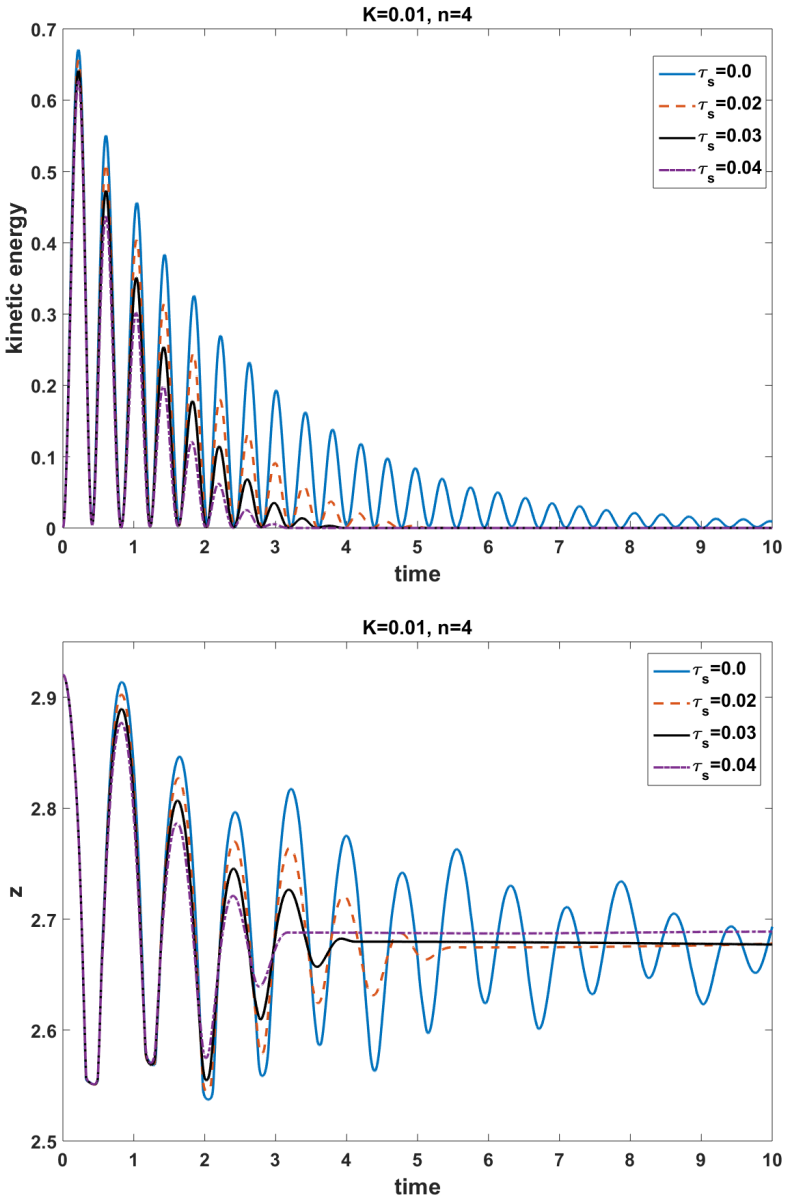

Figure 4.10: The evolution of the kinetic energy and the trajectory of the north tip computed for $K = 0.01$ and various τ_s, with $n = 4$ (for initial perturbation).

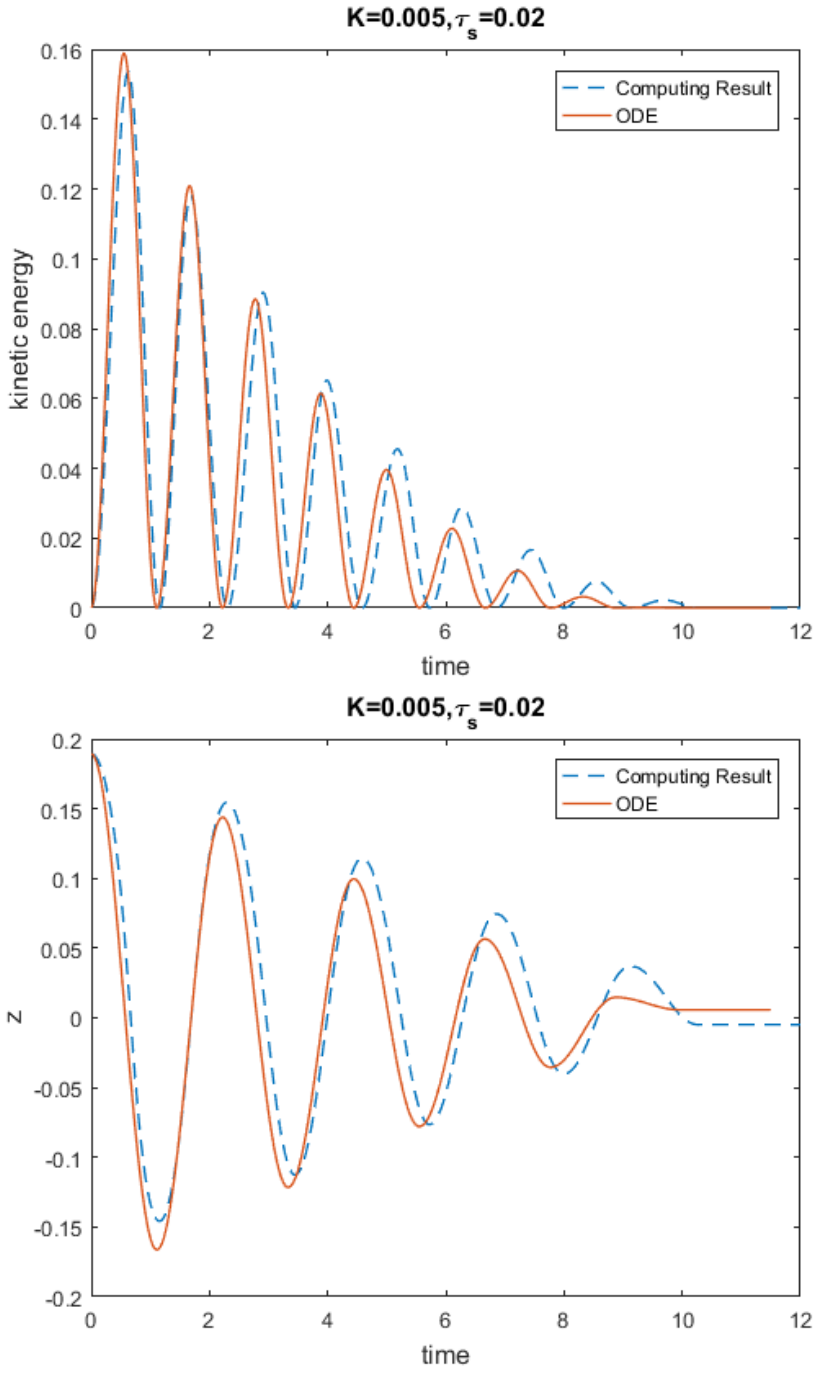

Figure 4.11: The evolution of the kinetic energy (upper plots) and the trajectory of the north tip (bottom plots) computed for equation 4.26(ODE) and octree-CFD code(computing results).

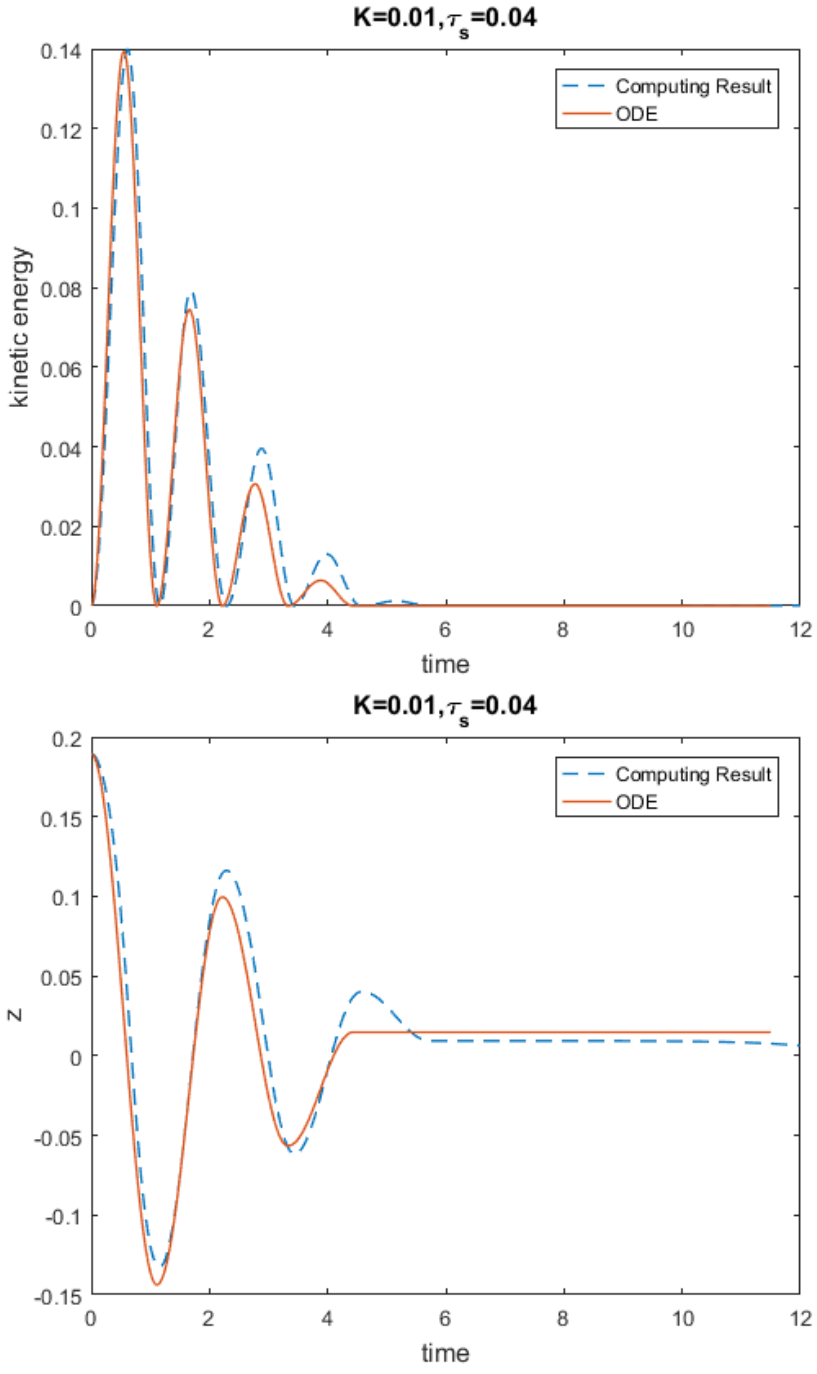

Figure 4.12: The evolution of the kinetic energy (upper plots) and the trajectory of the north tip (bottom plots) computed for equation 4.26(ODE) and octree-CFD code(computing results).

CHAPTER 5

Conclusion and Outlook

We deduced a variational inequality for free surface fluid flow. By using the dissipation method, we proved there is a finite stopping time for shear-thicking and Bingham oscillating droplet. The analysis for shear-thining case is lacking at present. Within a currently available framework of variational inequalities and energy type estimates, we don't see how one could treat a more general problem. The fundamental difficulty arises within the existing framework regardless of the form of exterior forces and also for the fixed (time-independent) domain. This type of a lower bound for the plastic dissipation term is crucial in the analysis of the finite stopping times of any yield stress fluid. Theoretical upper bounds for the finite stopping times of several

simple one-dimensional flows can be found in [31, 29, 41]. In the presence of a free surface, one may distinguish between the existence of a finite cessation time and the existence of a final arrested state (the latter can be attained in a finite or infinite time). Although the non-Newtonian fluid community (arguably) believes that the existence of finite stopping time is an intrinsic property of a yield stress fluid, there are only very few cases where proofs are known (i.e., those mentioned above). We consider the problem of small oscillations of the visco-plastic spheroid as another rare example. Besides being another example, the problem allows one to have an insight into the interplay between kinetic energy, free energy and dissipation for a yield stress fluid. We believe that the example studied in the thesis is relevant for a better understanding of physically- realiseable viscoplastic flows for the following reasons: (i) There is a number of applications where droplet flows of viscoplastic fluids arise; (ii) The crucial assumption about the irrotation velocity field is plausible in our setup.

Bibliography

[1] C. Acary-Robert, E. D. Fernández-Nieto, G. Narbona-Reina, and P. Vigneaux. A well-balanced finite volume-augmented Lagrangian method for an integrated Herschel–Bulkley model. *Journal of Scientific Computing*, 53(3):608–641, 2012.

[2] A. N. Alexandrou, G. C. Florides, and G. C. Georgiou. Squeeze flow of semi-solid slurries. *Journal of Non-Newtonian Fluid Mechanics*, 193:103–115, 2013.

[3] C. Ancey. Plasticity and geophysical flows: a review. *Journal of Non-Newtonian Fluid Mechanics*, 142(1):4–35, 2007.

[4] C. Ancey and S. Cochard. The dam-break problem for Herschel–Bulkley viscoplastic fluids down steep flumes. *Journal of Non-Newtonian Fluid Mechanics*, 158(1):18–35, 2009.

[5] S. D. Aziz and S. Chandra. Impact, recoil and splashing of molten metal droplets. *International journal of heat and mass transfer*, 43(16):2841–2857, 2000.

[6] N. J. Balmforth, R. V. Craster, A. C. Rust, and R. Sassi. Viscoplastic flow over an inclined surface. *Journal of non-newtonian fluid mechanics*, 139(1):103–127, 2006.

[7] N. J. Balmforth, I. A. Frigaard, and G. Ovarlez. Yielding to stress: recent developments in viscoplastic fluid mechanics. *Annual Review of Fluid Mechanics*, 46:121–146, 2014.

[8] M. Bercovier and M. Engelman. A finite-element method for incompressible non-Newtonian flows. *Journal of Computational Physics*, 36(3):313–326, 1980.

[9] N. Bernabeu, P. Saramito, and C. Smutek. Numerical modeling of non-Newtonian viscoplastic flows: Part II. Viscoplastic fluids and general tridimensional topographies. *International Journal of Numerical Analysis and Modeling*, 11(1):213–228, 2014.

[10] D. Bonn and M. M. Denn. Yield stress fluids slowly yield to analysis. *Science*, 324(5933):1401–1402, 2009.

[11] M. Bulicek, P. Gwiazda, J. Malek, and A. Swierczewska-Gwiazda. On unsteady flows of implicitly constituted incompressible fluids. *SIAM Journal on Mathematical Analysis*, 44(4):2756–2801, 2012.

[12] M. Chatzimina, G. C. Georgiou, I. Argyropaidas, E. Mitsoulis, and R. Huilgol. Cessation of couette and poiseuille flows of a Bingham plastic and finite stopping times. *Journal of non-newtonian fluid mechanics*, 129(3):117–127, 2005.

[13] M. Chatzimina, C. Xenophontos, G. C. Georgiou, I. Argyropaidas, and E. Mitsoulis. Cessation of annular Poiseuille flows of Bingham plastics. *Journal of non-newtonian fluid mechanics*, 142(1):135–142, 2007.

[14] A. J. Chorin. Numerical solution of the navier-stokes equations. *Mathematics of computation*, 22(104):745–762, 1968.

[15] A. Cianchi. A sharp trace inequality for functions of bounded variation in the ball. *Proceedings of the Royal Society of Edinburgh: Section A Mathematics*, 142(06):1179–1191, 2012.

[16] P. Coussot. Yield stress fluid flows: A review of experimental data. *Journal of Non-Newtonian Fluid Mechanics*, 211:31–49, 2014.

[17] D. Coutand and S. Shkoller. Unique solvability of the free-boundary Navier–Stokes equations with surface tension. *arXiv preprint math/0212116*, 2002.

[18] H. Eberlein and Michael. Existence of weak solutions for unsteady motions of Herschel–Bulkley fluids. *Journal of Mathematical Fluid Mechanics*, 14(3):485–500, 2012.

[19] E. D. Fern ndez Nieto, J. M. Gallardo, and P. Vigneaux. Efficient numerical schemes for viscoplastic avalanches. Part 1: the 1D case. *Journal of Computational Physics*, 264:55–90, 2014.

[20] I. Frigaard and C. Nouar. On the usage of viscosity regularisation methods for visco-plastic fluid flow computation. *Journal of non-newtonian fluid mechanics*, 127(1):1–26, 2005.

[21] I. Ginzburg. A free-surface lattice Boltzmann method for modelling the filling of expanding cavities by Bingham fluids. *Philosophical Transactions of the Royal Society of London A: Mathematical, Physical and Engineering Sciences*, 360(1792):453–466, 2002.

[22] R. Glowinski. *Lectures on numerical methods for non-linear variational problems*. Springer Science & Business Media, 2008.

[23] R. W. Griffiths. The dynamics of lava flows. *Annual Review of Fluid Mechanics*, 32(1):477–518, 2000.

[24] W. Gropp, D. Kaushik, M. Knepley, L. C. McInnes, K. Rupp, and B. Smith. of the 2004 acm/ieee conference on supercomputing,(sc04), ieee computer society, 2004, 34: 1–15, 2004.(cited on pp. 207, 213)[3] h. alcin, b. koobus, o. allain, and a. dervieux. efficiency and scalability of a two-level schwarz algorithm for incompressible and compressible flows. internat. j. numer. methods fluids, 72 (1): 69–89, 2013. issn: 0271-2091. doi: 10.1002/fld. 3733. url: http.

[25] J. Guermond, P. Minev, and J. Shen. An overview of projection methods for incompressible flows. *Computer methods in applied mechanics and engineering*, 195(44):6011–6045, 2006.

[26] M. E. Gurtin. *An introduction to continuum mechanics*, volume 158. Academic press, 1982.

[27] J. Haidar and J. Lowke. Predictions of metal droplet formation in arc welding. *Journal of Physics D: Applied Physics*, 29(12):2951, 1996.

[28] A. J. Hogg and G. P. Matson. Slumps of viscoplastic fluids on slopes. *Journal of Non-Newtonian Fluid Mechanics*, 158(1):101–112, 2009.

[29] R. Huilgol, B. Mena, and J. Piau. Finite stopping time problems and rheometry of Bingham fluids. *Journal of non-newtonian fluid mechanics*, 102(1):97–107, 2002.

[30] R. R. Huilgol. Variational inequalities in the flows of yield stress fluids including inertia: theory and applications. *Physics of Fluids (1994-present)*, 14(3):1269–1283, 2002.

[31] R. R. Huilgol. *Fluid mechanics of viscoplasticity*. Springer, 2015.

[32] I. R. Ionescu. Viscoplastic shallow flow equations with topography. *Journal of Non-Newtonian Fluid Mechanics*, 193:116–128, 2013.

[33] D. D. Joseph. Potential flow of viscous fluids: Historical notes. *International Journal of Multiphase Flow*, 32(3):285–310, 2006.

[34] G. Karapetsas and J. Tsamopoulos. Transient squeeze flow of viscoplastic materials. *Journal of non-newtonian fluid mechanics*, 133(1):35–56, 2006.

[35] H. Lamb. *Hydrodynamics*. Cambridge university press, 1932.

[36] F. Losasso, F. Gibou, and R. Fedkiw. Simulating water and smoke with an octree data structure. In *ACM Transactions on Graphics (TOG)*, volume 23, pages 457–462. ACM, 2004.

[37] G. P. Matson and A. J. Hogg. Two-dimensional dam break flows of Herschel–Bulkley fluids: the approach to the arrested state. *Journal of non-newtonian fluid mechanics*, 142(1):79–94, 2007.

[38] C. Miller and L. Scriven. The oscillations of a fluid droplet immersed in another fluid. *Journal of Fluid Mechanics*, 32(03):417–435, 1968.

[39] C. Min and F. Gibou. A second order accurate level set method on non-graded adaptive cartesian grids. *Journal of Computational Physics*, 225(1):300–321, 2007.

[40] B. R. Munson, D. F. Young, and T. H. Okiishi. Fundamentals of fluid mechanics. *New York*, 3(4), 1990.

[41] L. Muravleva, E. Muravleva, G. C. Georgiou, and E. Mitsoulis. Unsteady circular couette flow of a bingham plastic with the augmented lagrangian method. *Rheologica acta*, 49(11-12):1197–1206, 2010.

[42] K. Nikitin and Y. Vassilevski. Free surface flow modelling on dynamically refined hexahedral meshes. *Russian Journal of Numerical Analysis and Mathematical Modelling*, 23(5):469–485, 2008.

[43] K. D. Nikitin, M. A. Olshanskii, K. M. Terekhov, and Y. V. Vassilevski. A numerical method for the simulation of free surface flows of viscoplastic fluid in 3D. *J. Comp. Math*, 29:605–622, 2011.

[44] K. D. Nikitin, M. A. Olshanskii, K. M. Terekhov, and Y. V. Vassilevski. A splitting method for numerical simulation of free surface flows of incompressible fluids with surface tension. *Computational Methods in Applied Mathematics*, 15(1):59–77, 2015.

[45] M. A. Olshanskii, K. M. Terekhov, and Y. V. Vassilevski. An octree-based solver for the incompressible navier–stokes equations with enhanced stability and low dissipation. *Computers & Fluids*, 84:231–246, 2013.

[46] S. Osher and R. Fedkiw. *Level set methods and dynamic implicit surfaces*, volume 153. Springer Science & Business Media, 2006.

[47] J. Padrino, T. Funada, and D. Joseph. Purely irrotational theories for the viscous effects on the oscillations of drops and bubbles. *International Journal of Multiphase Flow*, 34(1):61–75, 2008.

[48] O. Pironneau. On the transport-diffusion algorithm and its applications to the navier-stokes equations. *Numerische Mathematik*, 38(3):309–332, 1982.

[49] S. Popinet. An accurate adaptive solver for surface-tension-driven interfacial flows. *Journal of Computational Physics*, 228(16):5838–5866, 2009.

[50] A. Prohl. *Projection and quasi-compressibility methods for solving the incompressible Navier-Stokes equations*. Springer, 1997.

[51] A. Prosperetti. Free oscillations of drops and bubbles: the initial-value problem. *Journal of Fluid Mechanics*, 100(02):333–347, 1980.

[52] W. H. Reid. The oscillations of a viscous liquid drop. *Quarterly of Applied Mathematics*, 18(1):86–89, 1960.

[53] A. Saïdi, C. Martin, and A. Magnin. Influence of yield stress on the fluid droplet impact control. *Journal of Non-Newtonian Fluid Mechanics*, 165(11):596–606, 2010.

[54] H. Samet. Applications of spatial data structures: Comuter graphics, image processing and gis. *Addison-Wesley, R eading, MA*, 1:99.

[55] B. Schweizer. Free boundary fluid systems in a semigroup approach and oscillatory behavior. *SIAM Journal on Mathematical Analysis*, 28(5):1135–1157, 1997.

[56] V. A. Solonnikov. Solvability of a problem on the evolution of a viscous incompressible fluid, bounded by a free surface, on a finite time interval. *Algebra i Analiz*, 3(1):222–257, 1991.

[57] J. Strain. Tree methods for moving interfaces. *Journal of Computational Physics*, 151(2):616–648, 1999.

[58] A. Syrakos, G. C. Georgiou, and A. N. Alexandrou. Cessation of the lid-driven cavity flow of Newtonian and Bingham fluids. *Rheologica Acta*, 55(1):51–66, 2016.

[59] K. M. Terekhov, K. D. Nikitin, M. A. Olshanskii, and Y. V. Vassilevski. A semi-lagrangian method on dynamically adapted octree meshes. *Russian Journal of Numerical Analysis and Mathematical Modelling*, 30(6):363–380, 2015.

[60] P. A. Thompson, W. Brinckerhoff, and M. O. Robbins. Microscopic studies of static and dynamic contact angles. *Journal of Adhesion Science and Technology*, 7(6):535–554, 1993.

[61] P. A. Thompson and S. M. Troian. A general boundary condition for liquid flow at solid surfaces. *Nature*, 389(6649):360–362, 1997.

[62] J. Töger, M. Carlsson, G. Söderlind, H. Arheden, and E. Heiberg. Volume tracking: A new method for quantitative assessment and visualization of intracardiac blood flow from three-dimensional, time-resolved, three-component magnetic resonance velocity mapping. *BMC medical imaging*, 11(1):1, 2011.

[63] J. Tsamopoulos, Y. Dimakopoulos, N. Chatzidai, G. Karapetsas, and M. Pavlidis. Steady bubble rise and deformation in Newtonian and viscoplastic fluids and conditions for bubble entrapment. *Journal of Fluid Mechanics*, 601:123–164, 2008.